

**Computational Modelling of Membrane Viscosity  
for Immersed Boundary Simulations of Red Blood Cell Dynamics**

by

Ping Li

A thesis submitted in partial fulfilment  
of the requirements for the degree of  
Doctor of Philosophy (PhD) in Engineering Science

The Faculty of Graduate Studies  
Laurentian University  
Sudbury, Ontario, Canada

©Ping Li, 2021

**THESIS DEFENCE COMMITTEE/COMITÉ DE SOUTENANCE DE THÈSE**  
**Laurentian University/Université Laurentienne**  
Faculty of Graduate Studies/Faculté des études supérieures

Title of Thesis Titre de la thèse	Computational Modelling of Membrane Viscosity for Immersed Boundary Simulations of Red Blood Cell Dynamics	
Name of Candidate Nom du candidat	Li, Ping	
Degree Diplôme	Doctor of Philosophy	
Department/Program Département/Programme	Engineering Science	Date of Defence Date de la soutenance January 29, 2021

**APPROVED/APPROUVÉ**

Thesis Examiners/Examineurs de thèse:

Dr. Junfeng Zhang  
(Supervisor/Directeur de thèse)

Dr. Brahim Chebbi  
(Committee member/Membre du comité)

Dr. Krishna Challagulla  
(Committee member/Membre du comité)

Dr. Brent Lievers  
(Committee member/Membre du comité)

Dr. Marianne Fenech  
(External Examiner/Examineur externe)

Dr. Kalpdrum Passi  
(Internal Examiner/Examineur interne)

Approved for the Faculty of Graduate Studies  
Approuvé pour la Faculté des études supérieures  
Dr. Lace Marie Brogden  
Madame Lace Marie Brogden  
Acting Dean, Faculty of Graduate Studies  
Doyenne intérimaire, Faculté des études supérieures

**ACCESSIBILITY CLAUSE AND PERMISSION TO USE**

I, **Ping Li**, hereby grant to Laurentian University and/or its agents the non-exclusive license to archive and make accessible my thesis, dissertation, or project report in whole or in part in all forms of media, now or for the duration of my copyright ownership. I retain all other ownership rights to the copyright of the thesis, dissertation or project report. I also reserve the right to use in future works (such as articles or books) all or part of this thesis, dissertation, or project report. I further agree that permission for copying of this thesis in any manner, in whole or in part, for scholarly purposes may be granted by the professor or professors who supervised my thesis work or, in their absence, by the Head of the Department in which my thesis work was done. It is understood that any copying or publication or use of this thesis or parts thereof for financial gain shall not be allowed without my written permission. It is also understood that this copy is being made available in this form by the authority of the copyright owner solely for the purpose of private study and research and may not be copied or reproduced except as permitted by the copyright laws without written authority from the copyright owner.

## Abstract

Although tremendous efforts have been devoted to modelling various membrane properties, few studies considered the membrane viscous effects. Meanwhile, immersed boundary method (IBM) has been a popular choice for simulating the motion of deformable cells in flow for the convenience of incorporating the flow-membrane interaction. Unfortunately, the direct implementation of membrane viscosity in IBM suffers severe numerical instability. In this thesis, three numerical schemes for implementing membrane viscosity in IBM are developed. Furthermore, the effects of membrane viscosity on the capsule dynamics in shear flow have been examined in detail.

In Chapter 1, the biomechanical properties of red blood cells (RBCs) are introduced followed with a literature review. Also, the motivations and objectives, the structure of this thesis, and the contributions of the candidate are described.

In Chapter 2, a finite-difference approach is proposed for implementing membrane viscosity in IBM. To improve the simulation stability, an artificial elastic element is added in series to the viscous component in the membrane mechanics. The detailed mathematical description and key steps for its implementation in immersed boundary programs are provided. Validation tests show a good agreement with analytical solutions and previous calculations. The accuracy dependence on membrane mesh resolution and simulation time step is also examined.

In Chapter 3, two other schemes are proposed based on the convolution integral expression of the Maxwell viscoelastic element. Several carefully designed tests are conducted and the results show that the three schemes have nearly identical performances in accuracy,

stability, and computational efficiency. In addition, suggestions have been provided for selecting appropriate relaxation time and artificial spring stiffness in IBM simulations using these methods.

In Chapter 4, the capsule dynamics in shear flows are simulated using the finite-difference method developed in Chapter 2. The similar but different effects from the membrane and interior viscosities are observed in the capsule deformation, inclination, and rotation frequency. Also, the analysis shows that the energy dissipation ratio cannot be treated as a constant to represent the membrane viscosity effect by increasing the interior viscosity. It is suggested that the membrane viscosity needs to be considered explicitly for accurate and reliable results.

This research developed three algorithms for membrane viscosity simulations with good accuracy, stability, and computational efficiency. The simulations of capsule dynamics in shear flow suggest that the membrane viscosity needs to be considered carefully for accurate and reliable results. The membrane viscous schemes could be valuable for future simulations of red blood cells and other biological capsules and vesicles.

## **Keywords**

Red blood cell, Capsule, Membrane viscoelasticity, Lattice Boltzmann method, Immersed boundary method, Finite-difference method, Integral scheme

## Co-Authorship Statement

I declare that this thesis includes materials that are the results of joint research collaborations. The following individuals have contributed to the publishable chapters of this thesis.

CHAPTER 2: Ping Li, Junfeng Zhang. A Finite-Difference Method with Subsampling for Immersed Boundary Simulations of the Capsule Dynamics with Viscoelastic Membranes.

CHAPTER 3: Ping Li, Junfeng Zhang. Finite-difference and Integral Schemes for Maxwell Viscous Stress Calculation in Immersed Boundary Simulations of Viscoelastic Membranes.

CHAPTER 4: Ping Li, Junfeng Zhang. Similar but Different Effects of Membrane and Interior Fluid Viscosities on Capsule Dynamics in Shear Flows.

P.L. is responsible for the initiation of this thesis. She developed the simulation model, collected the data, conducted the analysis, and wrote the chapters. J.Z. was the doctoral supervisor and provided feedback and revisions on drafts of each chapter. He also determined the thesis topic, methodology, and confirmed the conclusions.

I am aware of Laurentian University's Policy on Authorship and I certify that I have properly acknowledged the contribution of other researchers to my thesis. I certify that this thesis, and the research to which it refers, is the product of my own work.

## Acknowledgements

I would like to express my sincere gratitude to my supervisor Dr. Junfeng Zhang for the continuous support of my Ph.D. study and related research with his patience, encouragement, and immense knowledge. I appreciate that Dr. Zhang provided the opportunity to start my Ph.D. study and his support through the program. It was a pleasure for me to work and study under his supervision.

I thank my thesis committee, Dr. Krishna Challagulla, Dr. Brent Lievers, Dr. Brahim Chebbi, for their valuable time in helping me with my Ph.D. work and giving me insightful comments to improve my thesis. I am also grateful to Dr. Marianne Fenech (Mechanical Engineering, University of Ottawa) and Dr. Kalpdrum Passi (Mathematics and Computer Science) for reviewing my thesis, participating my defense, and providing hopeful comments on my research.

The financial support from the Ontario Trillium Scholarship at Laurentian University and the Natural Sciences and Engineering Research Council of Canada (NSERC) is gratefully acknowledged. I appreciate the computing resources provided by WestGrid ([westgrid.ca](http://westgrid.ca)), SHARCNet ([sharcnet.ca](http://sharcnet.ca)), and Compute/Calcul Canada ([compute canada.org](http://compute canada.org)), on which most of my calculations are accomplished.

Last, but not least, I would like to thank my son, Zilin Li, and my friends for supporting me spiritually throughout my Ph.D. study and my life in general. They offer me invaluable support, company, and encouragement, and we shared a lot of happiness, sorrow, stress, and all other sensitive feelings in life.

# Table of Contents

Abstract . . . . .	iii
Co-Authorship Statement . . . . .	v
Acknowledgements . . . . .	vi
Table of Contents . . . . .	x
List of Tables . . . . .	xii
List of Figures . . . . .	xxii
List of Appendices . . . . .	xxiii
<b>1 Introduction</b>	<b>1</b>
1.1 Biomechanical Properties of Red Blood Cells . . . . .	1
1.2 Background Literature . . . . .	7
1.2.1 Experimental and Numerical Studies of RBC Behaviors . . . . .	8
1.2.2 Typical Numerical Methods of RBC Dynamics . . . . .	10
1.2.3 Numerical Modelling for RBCs Membrane Viscosity . . . . .	12
1.3 Motivations and Objectives . . . . .	14
1.4 Structure of Thesis . . . . .	15
1.5 Statement of Original Contributions . . . . .	17
<b>2 A Finite-Difference Method with Subsampling for Immersed Boundary Simulations of the Capsule Dynamics with Viscoelastic Membrane</b>	<b>19</b>

Abstract . . . . .	20
2.1 Introduction . . . . .	22
2.2 Model Development and Algorithm Implementation . . . . .	28
2.2.1 The IBM . . . . .	28
2.2.2 Membrane Viscoelasticity . . . . .	29
2.2.3 The Finite-Difference Algorithm for the Maxwell Model . . . . .	32
2.2.4 The Integrated Algorithm for Membrane Viscosity in IBM . . . . .	36
2.3 Results and Discussion . . . . .	39
2.3.1 Nondimensional Analysis and Numerical Tests for the 1D Maxwell Model . . . . .	39
2.3.2 Droplet Deformation in Shear Flow . . . . .	46
2.3.3 Spherical Capsule Deformation in Shear Flow . . . . .	51
2.4 Summary and Concluding Remarks . . . . .	58
Appendices . . . . .	61
<b>3 Finite-Difference and Integral Schemes for Maxwell Viscous Stress Calcula- tion in Immersed Boundary Simulations of Viscoelastic Membranes</b>	<b>69</b>
Abstract . . . . .	70
3.1 Introduction . . . . .	72
3.2 Immersed Boundary Method and Membrane Mechanics . . . . .	74
3.2.1 The Immersed Boundary Method . . . . .	74
3.2.2 Membrane Viscoelasticity . . . . .	75
3.3 Numerical Schemes for Membrane Viscosity in IBM . . . . .	78
3.3.1 The Maxwell Viscoelastic Model for Stability Improvement . . . . .	78

3.3.2	Scheme FD: The Finite-Difference Method for Maxwell Viscous Stress . . . . .	81
3.3.3	Scheme Int1: The First Integral Scheme for the Maxwell Viscous Stress . . . . .	82
3.3.4	Scheme Int2: The Second Integral Scheme for the Maxwell Viscous Stress . . . . .	84
3.4	Results and Discussion . . . . .	85
3.4.1	1D Maxwell Element Test . . . . .	86
3.4.2	Twisting Spherical Shell Test . . . . .	91
3.4.3	Capsule Deformation in Shear Flow . . . . .	97
3.5	Summary . . . . .	104

**4 Similar but Distinct Roles of Membrane and Interior Fluid Viscosities in Capsule Dynamics in Shear Flows 107**

	Abstract . . . . .	108
4.1	Introduction . . . . .	110
4.2	Model and Methods . . . . .	113
4.2.1	Membrane viscoelasticity . . . . .	113
4.2.2	Immersed Boundary Method (IBM) . . . . .	116
4.2.3	Finite-Difference Method for Membrane Viscosity in IBM Simulations . . . . .	117
4.3	Results and Discussion . . . . .	120
4.3.1	Simulation Setup and Parameters . . . . .	120
4.3.2	Individual Effects of $\lambda$ and $Bq_s$ on Capsule Deformation . . . . .	122

4.3.3	Capsule Dynamics with Various $\lambda - Bq_s$ Combinations . . . . .	128
4.3.4	On the Energy Dissipation Ratio $d$ . . . . .	134
4.3.5	Effect of Dilatational Membrane Viscosity . . . . .	139
4.4	Conclusion . . . . .	142
<b>5</b>	<b>Concluding Statements</b>	<b>145</b>
5.1	Summary of Thesis . . . . .	145
5.2	Future Work . . . . .	149

# List of Tables

2.1	Simulated droplet deformation $D$ and inclination $\theta$ using various finite difference time interval $\Delta t$ and relaxation time $\tau$ . The results from Refs. [1, 2] are also provided for comparison. . . . .	48
2.2	Effects of different membrane mesh resolutions, simulation time steps, and finite-difference schemes on the result accuracy for capsule simulations. . . . .	57
3.1	Parameter substitution for applying the numerical schemes in this work to IBM simulations of viscoelastic membranes. . . . .	81
3.2	The coefficients in the general expression Eq. (3.30) for viscous stress $\sigma_M$ for different numerical schemes and the key assumptions involved in the derivations of these schemes. . . . .	85
3.3	Numerical errors for the calculated strain rates ( $L_{\dot{\varepsilon}}$ ) and viscous stresses ( $L_{\sigma}$ ) from different numerical schemes. Only the digit terms are listed and the common exponential term $10^{-4}$ has been omitted for clarity. . . . .	97
3.4	The one-CPU computation time (in seconds) for $10^5$ executions of individual computational components in our capsule IBM simulation. . . . .	103

4.1 Simulation parameters used in this work. All values are non-dimensional based on LBM simulation units: length in the lattice grid  $\delta x$ , time in the simulation time step  $\Delta t$ , and mass in the reference mass  $\delta m$ . The physical values of these simulation units can only be determined when a specific system is given. . . . . 120

# List of Figures

1.1	(a) A scanning electron micrograph shows the characteristic disk-like bi-concave shape of RBCs. (b) A picture of the microvascular networks in human mesenteric tissues. The vessels are labeled with letters as A for arterioles, V for venules and c for capillaries [3]. . . . .	2
1.2	Schematic representations for (a) the structure of a phospholipid with a polar head and two non-polar tails [4], (b) a vesicle formed by closed bilayers, and the bilayers formed by the phospholipids [4], and (c) The cytoskeleton architecture of the RBC membrane. The filamentous mesh-work of proteins forms a membrane skeleton along the entire cytoplasmic surface of the membrane [5]. . . . .	4
1.3	Rotation and deformation of a single RBC in shear flows from two-dimensional (2D) simulations with different viscosity contrast ratios Three consecutive RBC shapes, as indicated by numbers (1 to 3) and colors (black, blue, and red), are displayed for a period of the cell tank-treading (a), tumbling (b), or swinging (c) motions. The small circles represent a membrane marker initially at the cell rim [6]. . . . .	5
1.4	(a) A video micrograph of vessel in a 38 $\mu\text{m}$ venule with dextran-treated, aggregating blood flowing through it [7]. (b) A micrograph of RBCs flowing through microvascular networks in the rat mesentery [8]. . . . .	7

2.1	Schematic drawings showing (a) the Kelvin–Voigt model for viscoelastic membrane mechanics (spring $k$ for membrane elasticity and dashpot $\mu$ for membrane viscosity) and (b) the standard linear solid (SLS) model with an artificial spring $k'$ added to improve the numerical stability in IBM simulations. In (b) the dashpot $\mu$ and the spring $k'$ together form a Maxwell viscoelastic model. . . . .	33
2.2	The dependence of the artificial error $L$ on the spring constant $k'$ under different situations: (a) a constant strain period $T_0 = 100$ and different dashpot viscosity $\mu = 0.1, 0.2, 0.5, 1, 2, 5,$ and $10$ (from bottom to top); and (b) a constant dashpot viscosity $\mu = 1$ and different strain period $T_0 = 10, 20, 50, 100, 200, 500,$ and $1000$ (from top to bottom). . . . .	42
2.3	The dependence of the artificial error $L$ on the nondimensional relaxation time $\tau/T_0$ . This graph covers all data points in Fig. 2.2 with blue circles for data points from Figure 2.2(a) and red crosses for those from Figure 2.2(b). They all fall on a single curve on this graph, indicating the relative error $L$ only depends on the nondimensional relaxation $\tau/T_0$ . . . . .	43

2.4	Validation of our finite-difference algorithm with the 1D Maxwell model. The imposed strain $\epsilon_M(t)$ is shown in (a), and the effect of the finite difference time interval $\Delta t$ is examined in (b). The errors between the numerical results from our finite-difference method using different $\Delta t$ ( $\sigma_{M,n}$ ) and the theoretical values from Eq. (2.29) ( $\sigma_{M,t}$ ) are displayed in (c). The performance of our algorithm with different spring constant $k'$ is also displayed in (d). In (b) and (d), the thick lines are the analytical solutions from Eq. (2.30) for the limit of $k' \rightarrow \infty$ ; the thin lines are obtained from Eq. (2.29); and the symbols are calculated using our method Eq. (2.18). The arrows in (d) indicate the direction of $k'$ increasing from 0.1, 0.2, 0.5, 1, 2, 5, to 10. .	45
2.5	Simulated droplet deformation $D$ (a) and inclination $\theta$ (b) in shear flow for $Ca = 0.33$ , $\lambda = 1$ , $Bq_s = 5$ , and $Bq_d = 0$ . The inset in (a) shows the definitions of the deformation index $D$ and inclination angle $\theta$ . . . . .	46
2.6	Simulated droplet deformation $D$ (a, c) and inclination angle $\theta$ (b, d) in shear flow for systems with different Boussinesq numbers $Bq_s$ and $Bq_d$ . Results from previous studies [1, 2] are also displayed for comparison. .	49
2.7	Simulated capsule deformation $D$ (a) and inclination angle $\theta$ (b) in shear flow with different shear Boussinesq numbers $Bq_s$ . The symbols indicate the states at which the snapshots in Figure 2.8 are taken. . . . .	51

2.8	The initial (a) and deformed (b-l) capsule shapes selected from simulations in Figure 2.7. The Boussinesq number $Bq_s$ and the snapshot time for each shape are indicated in the labels. The deformed shapes are taken at the steady states (b-d, circles in Figure 2.7) or at the states with the first maximum or minimum deformations (e-f and i-j, diamonds in Figure 2.7) or inclination angles (g-h and k-l, triangles in Figure 2.7). The arrows in (b) indicate the shear flow direction. . . . .	52
2.9	Comparisons of the simulated capsule deformation $D$ (a) and inclination angle $\theta$ (b) using different membrane meshes. . . . .	54
2.10	Comparisons of the simulated capsule deformation $D$ (a) and inclination angle $\theta$ (b) using Meshes #3 and #4 of under dynamic shear with $Bq_s = 0$ . . . . .	56
2.11	(a) The flow streamlines from the stream function Eq. (2.38), (b) the velocities $u$ and $v$ along the $\psi = 0.2$ streamline (blue in a), and (c) the difference between the IBM interpolated velocity and the theoretical velocity from Eq. (2.38). The circles along the $\psi = 0.2$ streamline in (a) show the positions of a particle along this streamline at different time instances: the first circle at $t = 0$ and the last at $t = 500\delta t$ with an interval of $50\delta t$ between. The time step is $\delta t = 0.0015$ . . . . .	63

2.12 (a, a')	The strain rates along the streamline $\psi = 0.2$ from theory (solid lines) and calculated with different finite intervals (dashed lines and symbols), and (b, b') the differences of the calculated strain rates from the theory (dashed lines and symbols). The left panels show the entire time period $0 \leq t \leq 500\delta t$ , and the right panels enlarge the period $200\delta t \leq t \leq 320\delta t$ for a better view of details. The black straight lines in (b) and (b') are plotted to indicate the zero-difference state. . . . .	65
3.1	Schematic drawings showing (a) the Kelvin–Voigt model for viscoelastic membrane mechanics (spring $k$ for membrane elasticity and dashpot $\mu$ for membrane viscosity) and (b) the standard linear solid (SLS) model with an artificial spring $k'$ added to improve the numerical stability in IBM simulations. In (b) the dashpot $\mu$ and the spring $k'$ together form a Maxwell viscoelastic model. . . . .	79
3.2	Numerical accuracy for the 1D Maxwell element using different artificial spring constant $k'$ : (a) Error $L_0$ for the stress discrepancy in the Maxwell element from the original dashpot element; (b) Error $L_1$ for the stress inaccuracy caused by the numerical schemes FD, Int1, and Int2 for the Maxwell element; and (c) Error $L_2$ for the overall difference between the numerical calculated Maxwell stress and the original dashpot stress. In (b) and (c), two viscous stress calculation intervals $\Delta t = 1$ (solid lines) and $\Delta t = 6$ (dashed lines) are used for each numerical scheme. Also the $L_0$ line in (a) has been re-presented in (c) as the thick dashed line for a direct comparison of $L_0$ and $L_2$ . . . . .	89

3.3	(a) The spherical coordinate system adopted in the twisting sphere test and (b) a schematic visualization of the surface deformation under Eq. (3.35): The original $\phi=\text{constant}$ arc (solid line) deforms into the dashed curve, and the position of a surface point originally at $P$ moves to the new position $P'$ .	92
3.4	Comparisons of the calculated strain rates (left panels) and viscous stresses (right panels) using Scheme FD (symbols) with theoretical solutions (solid lines) in the spherical shell under the twisting deformation defined in Eq. (3.35). The numerical results from the other two schemes Int1 and Int2 are not displayed since they would be indistinguishable from those from Scheme FD shown here. . . . .	95
3.5	Profiles of deformation index $D$ of a spherical capsule in shear flows: (a) Comparisons of the deformation index $D$ from different numerical schemes for $Bq_s = 10$ (with $N = 25$ and $\kappa = 100$ ) and $Bq_s = 40$ (with $N = 50$ and $\kappa = 10$ ); (b) The $\kappa$ effect on the simulated capsule deformation for $Bq_s =$ 10 with $N = 25$ ; and (c) The $N$ effect on the simulated capsule deformation for $Bq_s = 40$ with $\kappa = 70$ . The inset figures enlarge the $D$ profiles at the profile peaks for a close view of the influences of $N$ and $\kappa$ values and the numerical schemes on simulation results. . . . .	99
3.6	Phase diagrams for the simulation stability (crosses: unstable; boxes: sta- ble) and accuracy (the filling color of each box represents the calculated $D_1$ value according to the color bar on the right) of capsule deformation in shear flow with (a) $Bq_s = 10$ and (b) $Bq_s = 40$ . The dashed lines separate the stable and unstable regions approximately. . . . .	102

3.7	Dependence of the peak deformation $D_1$ on the non-dimensional stiffness $\kappa$ for all stable simulations in Figure 3.6. The dashed curves are obtained by fitting the $D_1 \sim \kappa$ data points with the power function Eq. (3.42). . . .	103
4.1	Schematic drawings showing (a) the Kelvin–Voigt model for viscoelastic membrane mechanics (spring $k$ for membrane elasticity and dashpot $\mu$ for membrane viscosity) and (b) the standard linear solid (SLS) model with an artificial spring $k'$ added to improve the numerical stability in IBM simulations. In (b) the dashpot $\mu$ and the spring $k'$ together form a Maxwell viscoelastic model. . . . .	118
4.2	Variations of the capsule deformation $D$ (a and c) and inclination angle $\theta$ (b and d) with time in shear flows in responding to increases in interior fluid viscosity (a and b, $Bq_s = 0$ ) and membrane viscosity (c and d, $\lambda = 1$ ), respectively. . . . .	123
4.3	Comparison of the capsule deformation $D$ (a) and inclination angle $\theta$ (b) obtained in this work and those from Ref. [9] for $Ca = 0.3$ and $\lambda = 1$ . . .	125

4.4	Three representative cases (labeled on top) for the individual effects of $\lambda$ and $Bq_s$ on capsule deformation dynamics: the deformed shapes at $\dot{\gamma}t = 40$ (top row), the $x$ and $z$ positions of a membrane marker in the shear plane (second row); the marker velocity (third row), and the membrane circumference in the shear plane (bottom row). Also displayed in the top row panels are the black particles for a membrane node, the dashed circles for the original undeformed capsule shape, and the dashed straight lines for the inclination angle. In the third and bottom rows, the mean values calculated at the late stage of the simulations ( $\dot{\gamma}t = 30 \sim 50$ ) are displayed and indicated by dashed segments on the right. . . . .	126
4.5	Simulated deformation $D$ (top panels) and inclination angle $\theta$ (bottom panels) with various $\lambda$ and $Bq_s$ combinations. Error bars are utilized to show the property variations at $\dot{\gamma}t \sim 40$ , and the horizontal positions for data points with error bars at $Bq_s = 20, 30$ , and $40$ have been slightly shifted to avoid the overlapping of error bars. . . . .	128
4.6	Simulated capsule circumference $C^*$ (a1 and a2), membrane velocity $V_m^*$ (b1 and b2) and rotation frequency $\nu^*$ (c1 and c2) changing with membrane viscosity coefficient $Bq_s$ (left) and fluid viscosity ratio $\lambda$ (right). . . . .	130
4.7	Schematic illustrations for the effects on capsule deformation and inclination on membrane velocity in shear flow. Compared to the reference configuration in (a), Capsule (b) has the same inclination angle but a smaller deformation, and Capsule (c) has the same deformation but a larger inclination angle. . . . .	131

- 4.8 A reproduction of Figure 13b in Ref. [9] for the energy dissipation rates  $\Phi_{mem}$  due to membrane viscosity  $\mu_s$ ,  $\Phi_{int}$  due to interior fluid viscosity  $\mu_c$ , and the sum of them  $\Phi_{tot} = \Phi_{mem} + \Phi_{int}$  at different membrane viscosity  $Bq_s$ . The energy dissipation ratio  $d$  calculated from these dissipation rates via  $d = \Phi_{mem}/\Phi_{int}$  is plotted in (b), showing a strong non-linear relationship between  $d$  and  $Bq_s$ . . . . . 134
- 4.9 Simulated capsule deformation  $D$  and inclination angle  $\theta$  for all cases considered in this study with various  $(\lambda, Bq_s)$  combinations. Four different symbols are adopted to indicate the  $\lambda$  and  $Bq_s$  ranges: red circles for  $\lambda$  in  $0.2 \sim 3$  versus blue squares for  $\lambda$  in  $5 \sim 10$ , and filled symbols for  $Bq_s$  in  $0 \sim 10$  versus open symbols for  $Bq_s$  in  $20 \sim 40$ . Three specific series of such  $(\lambda, Bq_s)$  data points are connected by lines: Curve I for  $\lambda = 0.2 \sim 10$  and  $Bq_s = 0$ , Curve II for  $\lambda = 1$  and  $Bq_s = 0 \sim 40$ , and Curve III for  $\lambda = 5$  and  $Bq_s = 0 \sim 40$ . These curves and data points are re-presented in (b) for clarity and convenience of our discussions in the text. The respective  $\lambda$  and  $Bq_s$  values for each data point in (b) are also provided in parenthesis in the format of  $(\lambda, Bq_s)$ . . . . . 136
- 4.10 Variations of the capsule deformation  $D$  (a and c) and inclination angle  $\theta$  (b and d) with time in shear flows in responding to increases in dilatational viscosity  $Bq_d$  alone (a and b,  $Bq_s = 0$ ) and in combination with the shear viscosity (c and d,  $Bq_s = Bq_d$ ), respectively. . . . . 139

4.11 Capsule shapes during the deformation process of  $Bq_s = Bq_d = 40$  in shear flows. The dashed blue circles denote the original undeformed capsule shape for comparison, and the black dots represent the positions of one membrane node to show the membrane rotation. The dashed straight lines are plotted based on the calculated inclination angle  $\theta$  values, which are also shown with the deformation  $D$  in each subplot. . . . . 140

# List of Appendices

A	Demonstration and Analysis of the Numerical Noise in Calculated Strain Rate from the IBM Interpolated Velocity . . . . .	61
B	The Lattice Boltzmann Method for Flow Field and Simulation Setup . . .	66

# Chapter 1

## Introduction

### 1.1 Biomechanical Properties of Red Blood Cells

Blood is essential to various biological functions and processes in human and animal bodies. It circulates through a vast network of arteries, capillaries, and veins within the body, delivering necessary substances (such as oxygen and nutrients) and taking metabolic waste products (such as carbon dioxide, ammonia, and uric acid) away. Erythrocytes, usually called red blood cells (RBCs), typically take 40% to 45% of the blood volume in the adult human body. As the oxygen carriers, RBCs play a crucial role in blood flow behaviors and functions in the circulatory system. The shape of a healthy human RBC is biconcave (Figure 1.1(a)), with the surface area and volume as  $\sim 140 \mu\text{m}^2$  and  $\sim 90 \mu\text{m}^3$ , respectively [10]. The diameter of human RBCs is  $\sim 8 \mu\text{m}$ , by contrast, the diameter of the smallest vessels, such as capillaries connecting arterioles and venules, can be as small as  $2\sim 4 \mu\text{m}$  (Figure 1.1(b)). Therefore, the ability of RBCs to travel through the microcirculation systems is decisive for a healthy metabolism. To pass through the capillaries, RBCs have to deform significantly from its original biconcave shape. To achieve high deformability,

RBCs possess several unique features, such as the disk-like biconcave shape, the absence of a nucleus, and the extremely low elastic modulus of their membrane.

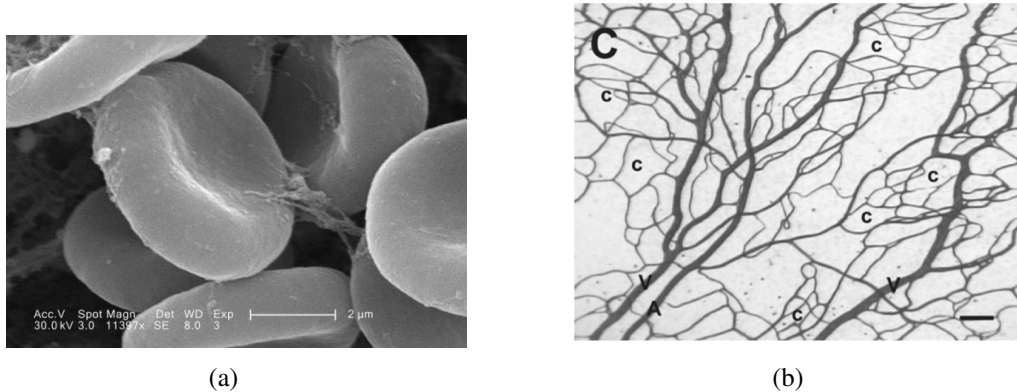


Figure 1.1: (a) A scanning electron micrograph shows the characteristic disk-like biconcave shape of RBCs. (b) A picture of the microvascular networks in human mesenteric tissues. The vessels are labeled with letters as A for arterioles, V for venules and c for capillaries [3].

Due to the fact that RBCs lack a cell nucleus and most organelles, their mechanical characteristics are mainly determined by the membrane, and the interior cytoplasm fluid, which is a high-concentration hemoglobin solution. Meanwhile, the suspending liquid for RBCs in the blood is called plasma, which is a dilute aqueous solution of proteins, glucose, electrolytes, etc. The RBC membrane separates the interior cytoplasm and exterior plasma. When taking a close look at it, this thin membrane is composed of three layers: the glycocalyx on the exterior, the lipid bilayer which contains many transmembrane proteins, and the membrane cytoskeleton, a structural network of proteins located on the inner surface of the lipid bilayer. The properties of the latter two components significantly affect the RBCs' deformability. A lipid is an amphiphilic phospholipid molecule, which has one hydrophilic (water-loving) polar head and two strong hydrophobic (water-hating) non-polar tails (Figure 1.2(a)). Two of these lipid monolayers fold in opposite directions and form a bilayer (Figure 1.2(b)). The hydrophilic heads of these molecules are in contact with the

aqueous fluids both inside and outside of the RBCs. In contrast, the hydrophobic tails will not interact with water. The strong hydrophobic tails of these molecules make these closed structures energetically favorable, and thus ensure the structural stability under mechanical stress. The membrane also exhibits viscous and bending resistance due to the lipid bilayer [11]. The cytoskeleton is formed by a network of the spectrin proteins linked by short filaments of actin (Figure 1.2(c)). The membrane elasticity is mainly attributed by the spectrin network. The typical thickness of a membrane lipid bilayer is  $\sim 4$  nm [4], in contrast to the diameter of a RBC  $\sim 8$   $\mu$ m as mentioned above. Because of this orders difference, the membrane is typically considered as a two-dimensional (2D) incompressible sheet with negligible thickness [12].

Experiments have shown that RBCs exhibit reduced deformability in many pathological situations, such as heart disease, hypertension, diabetes, malaria, and sickle cell anemia [13]. For example, sickle cell anemia (SCA) is a genetic disease that leads to mis-shaped RBCs. These sickle-shaped RBCs are less deformable and more viscoelastic and can cause blood vessel blockage, pain, strokes, and other tissue damage. In principle, the elevated cell rigidity can be caused by increasing the membrane viscoelastic modulus, bending resistance, and/or the cytoplasm viscosity.

RBCs are vital in maintaining normal metabolism. Consequently, tremendous efforts have been devoted to study the dynamics of an individual RBC in the flow field and the suspension flow behaviors of multiple RBCs in the past decades. Several phenomena have been noticed. Human RBCs suspended at low concentrations in steady shear flow have been observed to exhibit three types of motion (Figure 1.3). With sufficiently high shear rates and low internal-to-external fluid viscosity ratio, the cell membrane rotates around

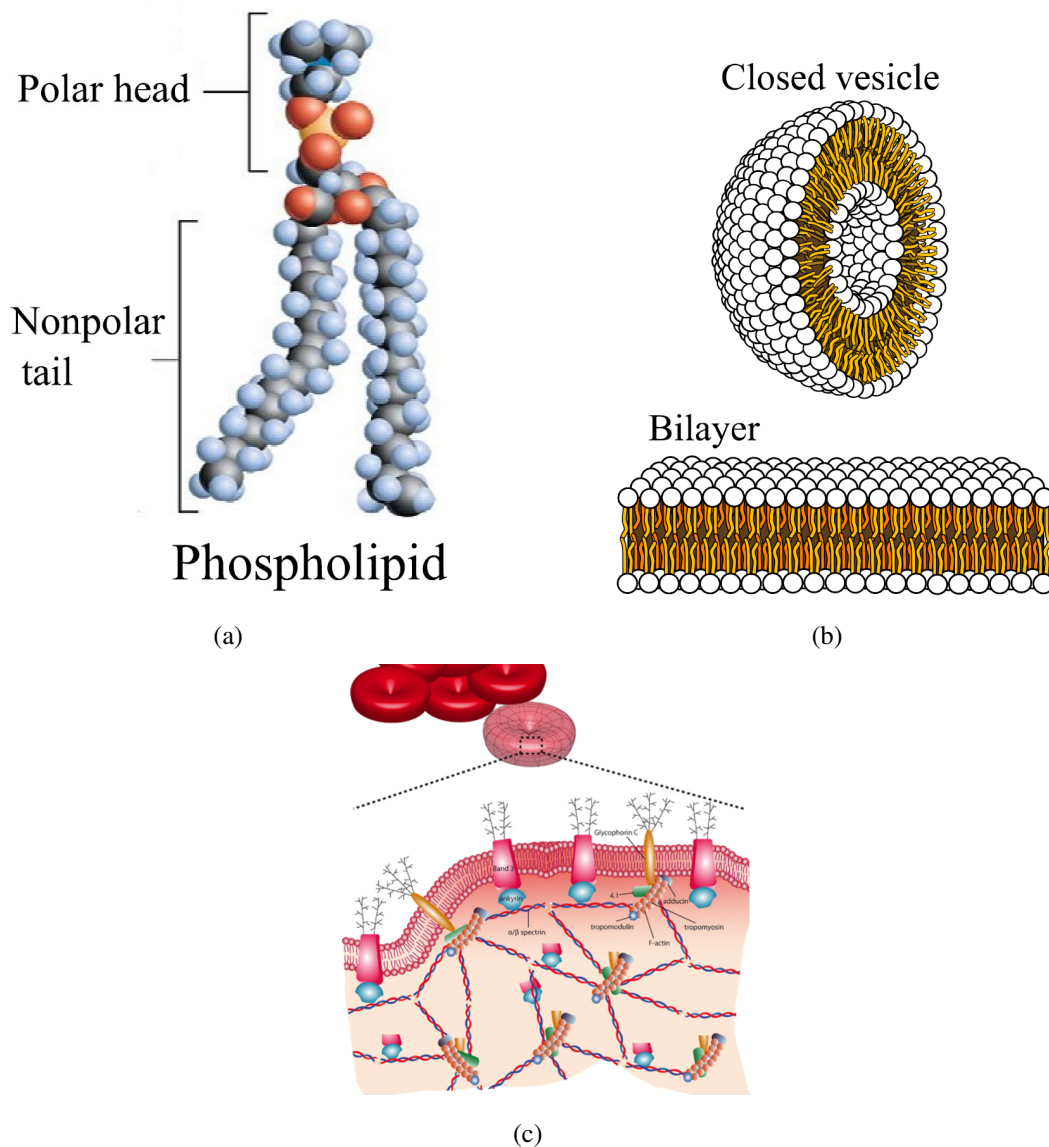


Figure 1.2: Schematic representations for (a) the structure of a phospholipid with a polar head and two non-polar tails [4], (b) a vesicle formed by closed bilayers, and the bilayers formed by the phospholipids [4], and (c) The cytoskeleton architecture of the RBC membrane. The filamentous meshwork of proteins forms a membrane skeleton along the entire cytoplasmic surface of the membrane [5].

the elongated cell in an approximately stable shape and the interior cytoplasm performs an eddy-like circulation flow [14, 15]. Fischer et al. [14] used the term tank-treading (TT) to describe this motion of RBCs (Figure 1.3(c)). Tumbling motion (Figure 1.3(a)) is observed for low shear rates of large viscosity contrast ratios. Another motion mode between these two regimes, the swinging motion (Figure 1.3(b)), was examined by Abkarian et al. [16].

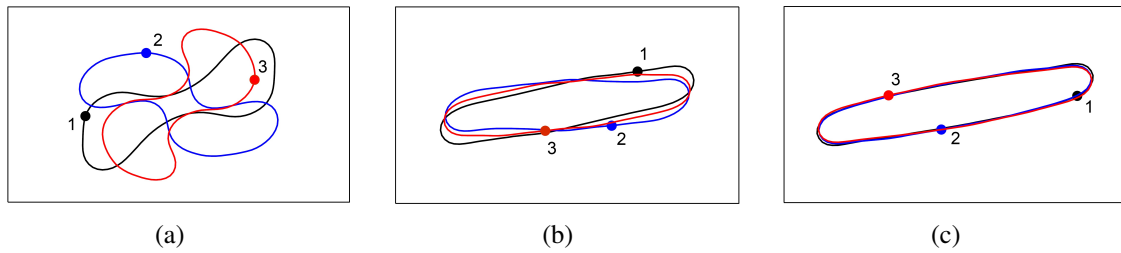


Figure 1.3: Rotation and deformation of a single RBC in shear flows from two-dimensional (2D) simulations with different viscosity contrast ratios. Three consecutive RBC shapes, as indicated by numbers (1 to 3) and colors (black, blue, and red), are displayed for a period of the cell tank-treading (a), tumbling (b), or swinging (c) motions. The small circles represent a membrane marker initially at the cell rim [6].

It happens under small shear flow and close to the tumbling tank-treading transition. In the swinging motion, a cell undergoes periodic shape deformation and inclination oscillation while its membrane is rotating around the liquid inside.

Other than the behaviors of an individual RBC, the dynamics of multiple RBCs in suspension flow are more complicated. RBCs can aggregate and form one-dimensional stacks-of-coins-like rouleaux or three-dimensional (3D) aggregates [13]. This phenomenon is particularly important in the microcirculation since such rouleaux or aggregates can affect in vivo hemodynamic behaviors, especially in low shear flow regions in the venules [17]. Increased aggregation is often observed in several clinical states, such as diabetes, heart diseases, inflammation, acute myocardial infarction, and bacterial sepsis [18]. Currently, there exist two theoretical descriptions of the aggregation: the bridging model and the depletion model [13]. The former assumes that macromolecules in the blood plasma, such as fibrinogen, can adhere to the adjacent RBC surfaces and bridge them together [19]. On the other hand, the depletion model attributes the RBC aggregation to a polymer depletion layer between RBC surfaces, which is accompanied by a decrease in the osmotic pressure [20]. In general, it can be assumed that the attractive interaction between RBC

surfaces will occur when the surfaces are close. On the contrary, a repulsive interaction would occur when the separation distance is sufficiently small.

When flowing in vessels, one notable phenomenon is that the blood flow features change greatly with the vessel diameter. For example, when blood flows in tubes with a diameter in the range of  $10 \sim 300 \mu\text{m}$ , the apparent viscosity decreases with diameter, and this phenomenon is called the Fahraeus-Lindqvist effect [21]. This observation is attributed to a cross-stream migration of RBCs leading to the formation of two phases [22]: a core with a high RBC concentration, and a cell-free layer (CFL), also called a cell-depleted layer, next to the tube wall devoid or depleted of cells (Figure 1.4). The CFL has a lower viscosity in comparison with the RBC core and serves as a lubrication layer, reducing the effective blood viscosity [13, 22]. The cross-stream migration of RBCs in tube flow is governed by two counter interactions: one is cell-wall hydrodynamic interactions, which drive the cells away from the wall; and the other is due to cell-cell hydrodynamic interactions, which tend to disperse RBCs [23]. The CFL is formed by cell migration, which depends on several factors, including the tube diameter, the hematocrit (volume fractions occupied by RBCs in the blood), the flow rate, and the RBC properties.

Besides the RBC motion in shear flow and multiple RBCs in a vessel, another interesting phenomenon is the hematocrit phase separation, which represents the divergence when blood flow across the bifurcation of a microvessel. The microvascular network is composed of many levels of vessel branches (Figure 1.1(b)). When blood flows toward a diverging bifurcation of a microvessel, RBCs preferentially enter the higher flow rate branch, leading to unequal discharge hematocrits in the downstream branches [24]. The unequal of the phase separation is mainly due to the non-uniform RBC distribution in the mother vessel



(a)



(b)

Figure 1.4: (a) A video micrograph of vessel in a  $38 \mu\text{m}$  venule with dextran-treated, aggregating blood flowing through it [7]. (b) A micrograph of RBCs flowing through microvascular networks in the rat mesentery [8].

[25]. This phenomenon is important for blood flow properties and oxygen delivery in microcirculation.

## 1.2 Background Literature

In Section 1.1, I discussed the complex structure of human RBCs on the molecular level, and their mechanical effects and flow behaviors in the microcirculation system are introduced. In this section, the relevant literature in RBC flows by experimental, theoretical, and computational methods are reviewed. In addition, I will describe several commonly used numerical techniques for RBC simulations. In these studies, RBCs are usually considered from a view of fluid mechanics, and their detailed molecular structures are neglected. They are treated as liquid capsules with a highly deformable membrane enclosing a Newtonian

fluid, the cytoplasm. Appropriate constitutive relationships have also been developed to describe the stress-strain relation for the RBC membrane.

### **1.2.1 Experimental and Numerical Studies of RBC Behaviors**

Researchers have utilized various techniques to examine RBC deformation. One classical method is micropipette aspiration. In this technique, a known suction pressure is applied within a small diameter glass pipet causing an aspiration of the contacted cell into the pipette, and the mechanical properties of the cell can be measured from the cell deformation. [26]. Optical tweezers have also been utilized to analyze RBC deformation. This instrument uses highly focused laser beams to manipulate microscopic and sub-microscopic objects like cells, nanoparticles and droplets [27]. Another useful technique for probing cell micromechanics is the magnetic twisting cytometry. This technique applies on twisting forces on ligand-coated magnetic microbeads bound to membrane receptors and measures the resulting bead rotation with a magnetometer. As the bead rotates, mechanical stresses opposing to the rotation are developed within the cell to which the bead is attached. As such, mechanical properties of the cell can be derived from measurements of the applied rotatory torque and the resulting bead rotation recorded from an in-line magnetometer [28]. However, these methods have their own disadvantages. One particular criticism is that the deformation generated by these methods is different from what the RBCs experience in the microcirculation situation, and the RBC properties obtained from these methods might be doubtful for modelling and simulating blood flow behaviors [29]. Another alternative approach for RBC mechanics studying is a rheoscope. Rheoscopic technology utilizes a transparent cone-plate chamber, where RBCs are suspended at low hematocrits in a high-

viscosity solution [30]. The RBC elongation and rotation frequency can be measured when the suspension is subjected to a simple shear flow. Nonetheless, such experimental studies also suffer several inevitable technical difficulties, including measurement inaccuracy and intraindividual distributions of cell parameters in the sample.

In addition to experiments, theoretical and numerical analysis are helpful to reveal underlying mechanisms, examine the various effects involved, provide design guidelines for practical applications, and even to interpret experimentally observed phenomena. Since theoretical analysis is limited to very simple situations, numerical simulations are often employed to obtain detailed, in-depth information, especially for that not directly available from experimental measurements.

Considering the tiny thickness of biological capsules (e.g.,  $\sim 10$  nm for RBCs) compared to the capsule size (e.g.,  $\sim 8$   $\mu\text{m}$  in diameter for RBCs), the capsule membrane can be treated as a two-dimensional sheet with no mass and thickness. The elastic stress induced by the membrane in-plane deformation usually is expressed in terms of the strain energy function, such as the Skalak function for RBCs [12]. Three-dimensional simulations of RBC deformation using the strain energy function for the membrane mechanics can be traced back to 1998 when Eggleton and Popel [31] examined the motion of a single RBC in simple shear flow. In this work, they assumed the internal and external fluid possessed the same viscosity and ignored the viscoelastic properties of the RBC membrane. The membrane was represented by the neo-Hookean elastic constitutive relationship. Similar numerical analysis have been conducted by Abkarian et al. [16], Sui et al. [32] and Skotheim and Secomb [33] for a single RBC or multiple RBCs. Their results showed that the motion of RBC was related to interior and suspending viscosities, membrane elasticity,

geometry, and shear rate. In other words, the RBC can exhibit either tumbling, tank-treading, or swinging alternately with different combinations of these above parameters.

### **1.2.2 Typical Numerical Methods of RBC Dynamics**

One characteristic for the blood flow in microcirculation is the low Reynolds number, and thus the flow is generally considered as Stokesian. Although Stokes flows can be described with relatively simple linear governing equations, the direct numerical simulation of the cellular flow system is still a challenging one. This is because the cell geometry is continuously changing with its deformation, and the simultaneous interaction among the cells and between cells and the vessel wall makes the modelling and calculations even more complicated. For classical simulation methods, boundary-fitted meshes need to be updated dynamically with the cell motion and deformation, and this is complicated and time-consuming in simulations. Fortunately, there are several numerical techniques that can effectively avoid these difficulties in RBC simulations

We start with the dissipative particle dynamics (DPD) [34], which is a mesh-free method for fluids and other soft matters. In DPD, the fluid is represented by a set of particles that move according to the Newton's second law. Such particles are interacting with each other via conservative, dissipative, and random forces. DPD has been employed in simulations of several RBC phenomena, such as RBC rotation in the shear flow [35, 36], rouleau formation and its disaggregation [37, 38], CFL in microvessel [39], and RBC separation at microvascular bifurcations [40]. In spite of these applications, the computational

efficiency could be a concern considering a large number of DPD particles and the complex calculation for interaction forces and particle trajectories. Moreover, the algorithm involves a group of parameters and their quantities are not directly related to macroscopic parameters [34].

The second approach is the boundary integral method (BIM), which utilizes the linearity of Stokes flows to express the flow solutions as surface integrals over interfaces and boundaries [41]. In BIM, only the cell and vessel-wall surfaces are required to be discretized, and the difficulties in the volumetric meshing of the complex-shaped flow domain are avoided. BIM has been employed for simulations of RBC motions, including tank-treading, swinging and tumbling [42, 43], large RBC deformations [44] and multiple cell interactions [45]. However, two major limitations exist. BIM requires the simulation in a periodic domain, however, it is difficult to model a system with complicated vessel boundaries. In addition, BIM is established based on the Stokes equation and therefore it is not applicable for flows with finite or moderate Reynolds numbers.

Besides the DPD and BIM, the immersed boundary method (IBM) has been extensively applied to simulate deformable objects in flow fields in recent years. IBM was developed to simulate the blood flow in the heart by Peskins in the 1970s [46]. One unique feature of IBM is that it combines the Lagrangian description for the moving/deforming objects and the Eulerian description for the surrounding flow in a novel approach. It thus avoids the complicated and time-consuming mesh regeneration. Also, the general IBM algorithm for incorporating the dynamic flow-structure interaction can be conveniently implemented in various numerical methods for fluid dynamics, such as the lattice Boltzmann method, finite element method and finite volume method. Because of these advantages, IBM has

become a popular choice for simulating the motion and deformation of cells, capsules and vesicles in flow fields recently [9, 41, 47]. For example, Eggleton and Popel [31] combined IBM with a finite element treatment of the RBC membrane to simulate large 3D RBC deformation in a shear flow. Bagchi [48] simulated a suspension containing multiple cells in a vessel. Zhang et al. [15, 47] developed an integrated immersed boundary-lattice Boltzmann method (IB-LBM) to study RBC behavior in both shear and channel flow. A more detailed description of IBM will be presented in section 2.2.1.

### **1.2.3 Numerical Modelling for RBCs Membrane Viscosity**

The RBC membrane shows complex constitutive relations between the membrane deformation and the induced internal stress. These properties can significantly affect the dynamics of individual RBC in flow field and the suspension flow behaviours of multiple cells. For example, studies show that the RBC membrane is highly deformable and flexible with very small elastic and bending moduli [49]. In contrast, it has a strong resistance to surface area change as indicated by a large area dilation modulus [50]. Besides, the membrane also exhibits viscous response in experimental studies, meaning a stress will be generated in response to the temporal change in membrane strain [51, 52]. This viscous behaviour is characterized by the membrane viscosity, which is the proportional coefficient relating the induced viscous stress to the strain rate in the membrane. Typically, the 2D membrane strain and stress tensors are decomposed into the shear and dilatational parts, and therefore two independent membrane viscosities exist, namely the shear and dilatational viscosities

[2, 9, 50].

In spite of the endeavours mentioned above in modelling other aspects of the complex membrane mechanics, the membrane viscosity has not been well addressed in RBC modelling and simulations. In the literature, only few RBC simulations considered the membrane viscosity. Noguchi and Gompper [53, 54] modeled the capsule membrane as a triangular network with tethers connecting membrane nodes. To represent the fluidity of the membrane, they flipped the tethers between two possible diagonals of two adjacent triangles based on a Monte Carlo method, and a probability parameter was adjusted to produce desirable membrane viscosity. Although their technique may appear simple and convenient for the node-link network representation of membrane, it is not applicable to the finite element representation typically employed in IBM simulations [2, 9]. The other trial based on the node-link network representation was proposed by Fedosove et al. [55, 56]. They introduced a dissipative force between two connecting nodes to mimic the viscous effect in membrane. Yet, their model is not suitable for capsules undergoing significant deformation [9, 57]. Besides, it cannot be used for general membranes with independent shear and dilatational viscosities separately.

The practical challenge for implementing membrane viscosity in IBM simulations is the numerical noise in the membrane viscous stress calculation. To circumvent this difficulty, Gounley and Peng [58] suggested to spread the membrane viscosity coefficient to fluid grid nodes in the layer along the membrane. Their strategy is contradictory to the classical definition of membrane viscosity. Moreover, it is physically not true when the membrane undergoes no change in deformation. Yazdani and Bagchi [9] proposed to replace the linear viscous component with a Maxwell viscoelastic element by adding an artificial spring

in series to the viscous element in order to improve the numerical stability. Although this is a more thoughtful numerical scheme, several concerns are noticed, including the unphysical decomposition of the shear and dilatation membrane stresses and the incorrect adoption of the Prony series for a nonlinear spring. Gounley and Peng [58] introduced a similar method based on the integral formulation from Christensen [59]; however, this method is limited to linear elastic membranes and it is not useful for general membrane strain energy functions such as the Skalak function for the RBC membrane [12]. Other than these concerns, the algorithms in Refs. [9, 58] involve extensive matrix calculations and this could affect the computation efficiency.

### **1.3 Motivations and Objectives**

The motivation of my research is to develop algorithms that overcome these concerns for implementing membrane viscosity in IBM simulations, and then to utilize the developed models to analyze the effects of membrane viscous stress on capsule dynamics in shear flows. The following specific objectives will be pursued:

1. To develop accurate and stable numerical schemes for simulating biological capsules of viscoelastic membranes with IBM;
2. To examine the numerical performances of the developed viscous methods in IBM simulations, including the accuracy, stability and efficiency;
3. To study the membrane viscosity effects on capsule dynamics in shear flows.

## 1.4 Structure of Thesis

This thesis comprises an introductory chapter (Chapter 1), three journal manuscripts (Chapters 2 - 4), and a concluding chapter (Chapter 5). Some information is repeated in Chapters 2 - 4 since they are intended for publication as individual stand-alone manuscripts.

In Chapter 1, after introducing some background information and presenting the up-to-date literature review, I present the research motivation and problems to be addressed in this thesis. The basic structure of this thesis and the scientific contributions are also outlined in this chapter.

Chapter 2, entitled “A finite-difference method with subsampling for immersed boundary simulations of the capsule dynamics with viscoelastic membranes”, proposes a finite-difference approach for implementing membrane viscosity in IBM. An artificial spring element is added in series to the viscous elements to improve the numerical stability. Detailed mathematical description of the method and key steps for its implementation in immersed boundary programs are provided. Validation calculations confirm the good agreement with analytical solutions and previous publications. The membrane mesh resolution independent and simulation time step tests are provided. It is concluded that this method would be a better choice for future IBM simulations of capsule dynamics with viscoelastic membranes.

Chapter 3, entitled “Finite-difference and integral schemes for Maxwell viscous stress calculation in immersed boundary simulations of viscoelastic membranes”, introduces two new schemes for the membrane viscous stress calculation based on the convolution inte-

gral expression of the Maxwell viscoelastic element. A set of comprehensive comparisons among the three algorithms developed in Chapter 2 and Chapter 3 are conducted from the aspects of accuracy, stability and efficiency. Firstly, a various of tests for accuracy are performed using a one-dimensional Maxwell element and a twisting sphere under a pro-defined sinusoidal deformation. After that, extensive simulations are conducted for the dynamic deformation of a spherical capsule in shear flow. These tests involve three viscous stress calculation schemes, different artificial spring constants and membrane viscous stress calculation frequencies. No observable differences are noticed among the three schemes in terms of numerical accuracy, stability and computational efficiency. The results are valuable for selecting appropriate simulation parameters in future IBM simulations of viscoelastic membranes.

Chapter 4, entitled “Similar but different effects of membrane and interior fluid viscosities on capsule dynamics in shear flows”, presents comprehensive numerical simulations to distinguish the dynamic effects from membrane and interior fluid viscosities on capsule dynamics in shear flows. The finite-difference scheme developed in Chapter 2 is used for the membranes viscous stress calculation in IBM. The results show that the membrane and interior viscosities have similar however different effects. The variations of various dynamic parameters, including the circumference, average membrane velocity, and rotation frequency, are also analyzed. In addition, an intuitive mechanism is proposed to relate the membrane velocity and rotation frequency to the capsule deformation and inclination angle. The observed spoon-like variation patterns for membrane velocity and rotation frequency are explained. Furthermore, the validation of the energy dissipation ratio approach based on the mathematical functional dependence is examined. This research is valuable

for a better understanding of the complex capsule dynamics in flows and also suggests that the membrane viscosity needs to be considered explicitly for accurate and reliable results in future studies.

Chapter 5 presents the overall conclusions of the thesis and proposes future research based on this thesis. The dissertation developed three numerical schemes for implementing membrane viscosity in IBM with comprehensive validation tests and analyses for the effects of membrane viscosity on the capsule dynamics in shear flow. For the future work, several topics can be explored, such as the effects of membrane viscosity on single RBC dynamics in shear flow, one or multiple RBCs in tube flow and bifurcation system.

## **1.5 Statement of Original Contributions**

This research has developed three algorithms to implement the viscoelastic membranes in IBM by using the finite-difference and integral schemes. Unlike previous attempts, these models are consistent with the classical membrane viscosity definition, and the algorithms have been carefully validated. The major contributions of this thesis are listed below.

1. The extensive verifications have been conducted for the algorithms from the aspects of accuracy, stability and computational efficiency. It is demonstrated that the errors from the viscous stress calculation can be neglected comparing to the other components in the IBM simulations. Furthermore, these methods avoid the complicated matrix calculations and only little extra computation time is required.
2. General suggestions for selecting the simulation parameters are provided. A nondi-

mensional parameter, the ratio of the relaxation time for the Maxwell element to the characteristic time for the element deformation, is defined for selecting an appropriate spring stiffness. Also, the membrane viscous stress calculation frequency is analyzed and we recommend to do the calculation at each simulation time step for better numerical stability.

3. In previous studies, the energy dissipation ratio has been used to represent the membrane viscosity effect by increasing the interior viscosity; however, the applicability and accuracy of this treatment have not been evaluated carefully. In this study, tests with various combinations of membrane and interior fluid viscosities are conducted to analyze the deformation dynamics of a single capsule in shear flow. The results show that the membrane and interior fluid viscosity have similar however different effects on the capsule deformation dynamics. The dissipation ratio is a system-process-dependent variable and it cannot be treated as a constant even for the same capsule. This suggests that the membrane viscosity needs to be considered explicitly for accurate and reliable results in future studies.

## **Chapter 2**

# **A Finite-Difference Method with Subsampling for Immersed Boundary Simulations of the Capsule Dynamics with Viscoelastic Membrane \***

Ping Li and Junfeng Zhang

Bharti School of Engineering, Laurentian University

935 Ramsey Lake Road, Sudbury, ON P3E 2C6, Canada

---

\*This Chapter has been published in the International journal for numerical methods in biomedical engineering, 35(6): e3200, 2019

## Abstract

The membrane or interfacial viscosity is an important property in many multiphase and biofluidic situations, such as red blood cell dynamics and emulsion stability. The immersed boundary method (IBM), which incorporates the dynamic flow-membrane interaction via force distribution and velocity interpolation, has been extensively employed in simulations of such systems. Unfortunately, direct implementation of membrane viscosity in IBM suffers severe numerical instability, which causes an IBM calculation to break down before generating any useful results. Few attempts have been recently reported; however, several concerns exist in these attempts, such as the inconsistency to the classical definition of membrane viscosity, the inability to model the shear and dilatational viscosities separately, the unjustified mathematical formulations, and the complicated algorithms and computation. To overcome these concerns, in this paper we propose a finite-difference approach for implementing membrane viscosity in immersed boundary simulations. The viscous stress is obtained via finite-difference approximations to the differential strain-stress relationship, with the help of a sub-sampling scheme to reduce the numerical noise in the calculated strain rates. This simple method has also avoided the complicated matrix calculations in previous attempts, and hence a better computational efficiency is expected. Detailed mathematical description of the method and key steps for its implementation in immersed boundary programs are provided. Validation and illustration calculations are performed, and our results are compared to analytical solutions and previous publications with satisfactory agreement. The influences of membrane mesh resolution and simulation time step are also examined, and the results show no indication that our finite-difference method has downgraded the general IBM accuracy. Based on these simulations and anal-

ysis, we believe that our method would be a better choice for future IBM simulations of capsule dynamics with viscoelastic membranes.

## **Keywords**

Capsule dynamics, Droplet/Bubble dynamics, Finite-difference method, Front-tracking method, Immersed boundary method, Interfacial viscosity, Membrane viscosity, Multiphase flow

## 2.1 Introduction

Since it was first proposed in the 1970s by Peskin [46] to simulate the blood flow in the heart, the immersed boundary method (IBM) has been utilized extensively for various flow systems, including fluid-structure interactions, particulate flows, multiphase flows, flows through heart valves, swimming and flight, settling processes of flexible objects in fluid, and filament flapping dynamics [60–64]. One attractive feature of IBM is that it combines the Lagrangian description for the moving/deforming objects and the Eulerian description for the surrounding flow in a novel approach and thus avoids the complicated and time-consuming mesh regeneration. In addition, IBM provides a general algorithm for incorporating the dynamic flow-structure interaction that can be conveniently implemented in any numerical flow solvers. For this reason, in recent years IBM has become a popular choice for simulating the motion and deformation of cells, capsules and vesicles in flow fields [9, 41, 47, 65–69].

To simulate the dynamics of individual capsules in flow field and even the suspension flow behaviors of multiple capsules, in addition to IBM for the flow-membrane interaction, several other challenges exist and tremendous efforts have been devoted in past years. The membranes of these biological cells and vesicles and synthetic capsules usually show complex constitutive relations between the membrane deformation and the induced internal stress. For example, studies show that the red blood cell membrane is highly deformable and flexible with very small elastic and bending moduli; however, it has a strong resistance to surface area change as indicated by a large area dilation modulus [50]. In addition, experimental investigations via various techniques [57, 70, 71] have shown that these capsule

membranes also exhibit viscous characteristics as 2D liquids, meaning that stress will be induced in response to the strain rate in the membrane. Koleva and Rehage [72, 73] also studied the membrane properties and capsule dynamics of polysiloxane microcapsules, and the membrane viscous effect has been observed. Similar viscous behaviors have also been observed in fluid-fluid interfaces when surfactants or other contaminants are present [1, 2, 74]. This viscous behavior is characterized by the membrane viscosity, which is the proportional coefficient relating the induced viscous stress to the strain rate in membrane. Typically, the 2D membrane strain and stress tensors are decomposed into the shear and dilatational parts, and therefore two independent membrane viscosities exist, namely the shear and dilatational viscosities [2, 9, 50, 75]. Experiments have shown that the interfacial viscosity is an important factor for the dynamic behaviour of foams and emulsions [75, 76]; in particular, the dilatational viscosity is more relevant for short-term foam/emulsion stability [77, 78]. Furthermore, for membranes, studies have shown that the dilatational viscosity is essential to the coexisting phase domains in Langmuir monolayers [79] and the relaxation and poration of giant vesicles in electric fields [80].

In spite of the endeavours in modelling other aspects of the complex membrane mechanics, the membrane viscosity has not been well addressed in IBM capsule simulations. Typically the finite element representation is adopted to discretize the membrane into triangular elements for three-dimensional (3D) systems or spring elements for two-dimensional (2D) systems [47, 66]. Several attempts at including the membrane viscosity in simulations have been reported in the literature. Noguchi and Gompper [53, 54] modeled the capsule membrane as a triangular network with tethers connecting membrane nodes. To represent the fluidity of the membrane, they flipped the tethers between two possible diagonals of

two adjacent triangles based on a Monte Carlo method, and a probability parameter was adjusted to produce different membrane viscous effects. This technique may appear simple and convenient for the node-link network representation of membrane; however it is not applicable to the finite element representation typically employed in IBM simulations [2, 9, 66, 81], since flipping a link direction between two adjacent triangular elements causes changes in the reference configurations as well as the shape functions for the two elements. The single probability parameter is not adequate either to consider independent shear and dilatational membrane viscosity values. Also based on the node-link network representation, Fedosove et al. [55, 56] introduced a dissipative force between two connecting nodes to mimic the viscous effect in membrane. An expression was derived to relate the apparent membrane viscosity to the dissipative force parameters. The derivation was performed by assuming a hexagonal network configuration around a node, and this will not be true for capsules undergoing significant deformation as shown in previous simulations and experiments [9, 57, 81]. Again only one membrane viscosity was established there and therefore it is not suitable to model general membranes with independent shear and dilatational viscosities. Moreover, the derived apparent membrane viscosity has a different dimension (unit Pa·s in Refs. [55, 56]) than that from the classical membrane viscosity definition (unit N·s/m) [1, 2, 9, 50, 57]; and this makes it difficult for direct utilization of measured membrane viscosity in simulations. As for the finite element representation where the membrane is discretized into 2D triangular elements, Pozrikidis [82] and Gounley et al. [2] studied the droplet dynamics in shear flow with interfacial viscosity consistent with its classical definition. However, these studies were performed with the

boundary integral method.

The practical challenge for implementing membrane viscosity in IBM simulations is the numerical noise in membrane velocity, which is amplified in the strain rate calculation and eventually causes the simulations to break down. Please see Appendix A for more details. To circumvent this difficulty, Gounley and Peng [58] suggested spreading the membrane viscosity coefficient to fluid grid nodes in the layer along the membrane via the delta function, similar to the classical force distributing treatment in IBM. No rigorous justification was presented there, and this method cannot distinguish the shear and dilatational membrane viscosities either. Moreover, the extra fluid viscosity at fluid nodes near the membrane will affect the flow field and flow-membrane interaction even when the membrane undergoes no change in deformation (i.e., zero strain rate), and this is contradictory to the classical description of membrane viscosity. For a simple example, considering a membrane placed in a simple shear flow in parallel to the flow and moving with the fluid. The entire membrane simply moves at a constant velocity and there will be no strain rate in the membrane. Therefore there is no viscous stress and the membrane viscosity is not playing a role in this system. However, the extra fluid viscosity near the membrane, coming from the membrane viscosity according to Ref. [58], will cause changes in the velocity profile as well as the shear stress on the membrane. This is physically not true. For a more realistic example, we can look at the membrane of a steady, tank-treading capsule or red blood cell in shear flow. By definition, membrane viscous stress only exists in the area where the membrane undergoes a local configuration change, and the viscous stress status depends on the in-plane strain rate. On the opposite, the method in Ref. [58] adds artificial viscous effect all along the membrane uniformly, regardless of the membrane strain state.

The extra viscous stress from this approach is related to the local velocity gradient, and again this is not consistent to the rheological and biomechanical description of interfacial and membrane viscosity [50, 75].

A more thoughtful numerical scheme to model membrane viscosity for IBM simulations was proposed by Yazdani and Bagchi [9]. Here the classical definition and formulation of membrane viscosity were followed (i.e., the viscous stress was calculated from the simultaneous strain rate in the membrane). To improve the numerical stability, the linear viscous component was replaced with a Maxwell viscoelastic element by adding an artificial spring in series to the viscous element. The spring stiffness needs to be large enough so its effect on the membrane dynamics can be neglected. A dimensional analysis shows that this requirement can be expressed by a nondimensional parameter, the ratio of the relaxation time of the Maxwell element to the characteristic time of the element deformation, and the membrane elasticity should not be involved (see Sect. 2.3.1 for more details). Instead, Yazdani and Bagchi [9] used the ratio of the artificial spring stiffness to the membrane elastic module as a major control parameter when studying the system performance. In addition, the algorithm was established on the Prony series expression of the time-dependent modulus; in the meantime, it had assumed that the artificial spring element in the Maxwell component follows the same stress-strain constitutive relationship as the membrane elasticity. It should be noted that the exponential terms in the Prony series are obtained from the condition that the spring elements in the Maxwell components respond *linearly* to their individual strain rates [83]. Therefore the two aspects in Ref.[9] (the Prony series expression of the dynamic modulus and the neo-Hookean stress-strain relationship for the artificial spring component) are contradictory. Moreover, the viscous stress calculation requires a

decomposition of the elastic stress tensor into the shear and dilatational parts; and the decomposition method in Refs. [9, 84] leads to *non-zero* shear and dilatational stresses even for a membrane at its *undeformed, stress-free* state. Gounley and Peng [58] has introduced a similar method based on the integral formulation from Christensen [59]; however, it is difficult to implement the general membrane strain energy functions such as the Skalak function for red blood cell membrane [12]. Also, this method did not separate the shear and dilatational components in stress and strain tensors, and therefore is not suitable for simulating membranes or interfaces with independent shear and dilatational viscosities. In addition to these fundamental concerns, the algorithms in Refs. [9, 58] involve extensive matrix calculations; and the algorithms have not been validated, for example, with comparisons to published results, probably due to the lack of such results for capsules in the literature.

Our aim in this study is to develop a numerical scheme for IBM simulations of flexible capsules with membrane viscosity consistent with the classical definition. Following Yazdani and Bagchi [9] we also use an artificial spring element to improve the numerical stability; however, the strain rate is obtained directly from the membrane dynamic deformation via the finite element method, and the induced viscous stress is calculated efficiently via a finite-difference approach. The method can incorporate the shear and dilatational membrane viscosities independently, and various membrane constitutive relationships or even the surface tension effect for fluid droplets can be considered. Rigorous analysis for the effect from the artificial spring element is performed, and this provides a guidance for choosing an appropriate value for the artificial spring constant. The finite-difference algorithm for calculating the viscous stress is first tested for the one-dimensional (1D) Maxwell vis-

coelastic element, for which analytical solutions are available for comparison. The method is then applied to simulate the deformation of droplets and capsules in shear flows with various system parameters, and the calculated droplet deformation is compared to available published results from Refs. [1, 2]. Effects of membrane mesh resolution and simulation time step are also evaluated, and direct comparisons show that our finite-difference method has introduced no negative impact on the IBM simulation accuracy.

## 2.2 Model Development and Algorithm Implementation

### 2.2.1 The IBM

Here we present IBM from a practical prospect, while more mathematical descriptions and analyses can be found in the literature [46, 60, 64]. To solve the flow field (both inside and outside of the capsule) an appropriate numerical method can be adopted and here we assume the solution is performed over a uniform Eulerian grid. IBM incorporates the dynamic interaction between the Eulerian flow field and the Lagrangian capsule membrane via two steps: the force distribution and the velocity interpolation. When a membrane is deformed, the membrane force will be developed according to the material constitutive relationship, as to be discussed in Sect. 2.2.2. The membrane force  $\mathbf{F}_m$  calculated at a membrane node  $\mathbf{x}_m$  is then transferred to local fluid nodes  $\mathbf{x}_f$  as body forces  $\mathbf{F}_f$ :

$$\mathbf{F}_f(\mathbf{x}_f) = \sum_{\mathbf{x}_m} D(\mathbf{x}_f - \mathbf{x}_m) \mathbf{F}_m(\mathbf{x}_m) \quad (2.1)$$

using a discrete delta function  $D(\mathbf{x})$ , which is chosen to approximate the properties of the Dirac delta function [46]:

$$D(\mathbf{x}) = \frac{1}{(4\delta x)^3} \left(1 + \cos \frac{\pi x}{2\delta x}\right) \left(1 + \cos \frac{\pi y}{2\delta x}\right) \left(1 + \cos \frac{\pi z}{2\delta x}\right), \quad (2.2)$$

$$|x| \leq 2\delta x, |y| \leq 2\delta x, \text{ and } |z| \leq 2\delta x$$

$$D(\mathbf{x}) = 0, \text{ otherwise.}$$

Here  $x, y, z$  are the three elements of location vector  $\mathbf{x}$ , and  $\delta x$  is the Euler grid resolution. Other forms for the kernel function  $D(\mathbf{x})$  have also been proposed in the literature [64, 66].

On the other hand, as the fluid flows, the membrane moves with the ambient flow and deforms accordingly. To enforce the no-slip requirement between the flow and the membrane surface, the membrane velocity  $\mathbf{u}_m(\mathbf{x}_m)$  is obtained from the local flow field  $\mathbf{u}$  via interpolation, which also uses the kernel function  $D$ :

$$\mathbf{u}_m(\mathbf{x}_m) = (\Delta x)^3 \sum_{\mathbf{x}_f} D(\mathbf{x}_f - \mathbf{x}_m) \mathbf{u}(\mathbf{x}_f) . \quad (2.3)$$

Here the summation runs over all fluid nodes with  $D > 0$ . The membrane location and configuration can then be updated, for example, using the Euler approximation according to the membrane velocity  $\mathbf{u}_m$ .

### 2.2.2 Membrane Viscoelasticity

Considering the tiny thickness of biological capsules (e.g.,  $\sim 10$  nm for red blood cells) compared to the capsule size (e.g.,  $\sim 8$   $\mu\text{m}$  in diameter for red blood cells), the capsule

membrane can be treated as a 2D sheet with no mass and thickness. The elastic stress induced by the membrane in-plane deformation usually is expressed in terms of the strain energy function, such as the Skalak function for red blood cells [12]:

$$W_s = \frac{E_s}{8}(I_1^2 + 2I_1 - 2I_2) + \frac{E_a}{8}I_2^2 \quad , \quad (2.4)$$

where  $W_s$  is the strain energy per membrane area, and  $E_s$  and  $E_a$  are, respectively, the shear and dilation moduli. The strain invariants  $I_1$  and  $I_2$  are related to the two principle stretch ratios  $\varepsilon_1$  and  $\varepsilon_2$  for a 2D membrane by

$$I_1 = \varepsilon_1^2 + \varepsilon_2^2 - 2 \quad ; \quad I_2 = \varepsilon_1^2 \varepsilon_2^2 - 1 \quad . \quad (2.5)$$

The elastic stress tensor  $\tau^e$  can then be obtained from this energy function as [12, 85]

$$\tau^e = \tau_1^e \mathbf{e}_1 \otimes \mathbf{e}_1 + \tau_2^e \mathbf{e}_2 \otimes \mathbf{e}_2 \quad , \quad (2.6)$$

where

$$\tau_1^e = \frac{1}{\varepsilon_2} \frac{\partial W_s}{\partial \varepsilon_1} \quad ; \quad \tau_2^e = \frac{1}{\varepsilon_1} \frac{\partial W_s}{\partial \varepsilon_2} \quad ; \quad (2.7)$$

are the two principal stresses; and  $\mathbf{e}_1$  and  $\mathbf{e}_2$  are their corresponding directions. The principle directions  $\mathbf{e}_1$  and  $\mathbf{e}_2$  can be obtained as the unit eigenvectors of the left Cauchy-Green deformation tensor  $\mathbf{G} = \mathbf{F}\mathbf{F}^T$  with  $\mathbf{F}$  as the deformation gradient matrix [9, 66]. With the membrane being discretized into triangular elements, the matrix  $\mathbf{F}$  can be readily calculated by comparing the deformed and original configurations of each element [86]. The

strain tensor  $\mathbf{E}$  is related to matrices  $\mathbf{G}$  or  $\mathbf{F}$  as:

$$\mathbf{E} = \frac{1}{2}(\mathbf{G}^T - \mathbf{1}) = \frac{1}{2}(\mathbf{F}^T \mathbf{F} - \mathbf{1}) \quad . \quad (2.8)$$

The viscous stress  $\tau^v$  in membranes or fluid interfaces is typically split into two parts: the shear viscous stress  $\tau_s^v$  induced by the shear (deviatoric) part of the strain rate tensor  $\mathbf{D}$ , and the dilatational viscous stress  $\tau_d^v$  from the dilatational (hydrostatic) part of  $\mathbf{D}$  [2, 9, 82, 87, 88]:

$$\tau^v = \tau_s^v + \tau_d^v = \mu_s [2\mathbf{D} - \text{tr}(\mathbf{D})\mathbf{I}] + \mu_d \text{tr}(\mathbf{D})\mathbf{I} \quad , \quad (2.9)$$

where  $\mu_s$  and  $\mu_d$  are the shear and dilatational membrane viscosities, respectively. The matrix  $\mathbf{D}$  is the strain rate tensor of the membrane and  $\mathbf{I}$  is the  $2 \times 2$  unit matrix. A convenient way to numerically obtain the strain rate tensor  $\mathbf{D}$  is to apply a backward finite-difference approximation to the strain tensor  $\mathbf{E}$ ; whereas another approach is via the membrane velocity gradient [2, 82, 88]

$$\mathbf{D} = \frac{1}{2} [\nabla_m \mathbf{u}_m + (\nabla_m \mathbf{u}_m)^T] \quad , \quad (2.10)$$

where  $\nabla_m$  is the gradient operator and  $\mathbf{u}_m$  is the membrane velocity, both in the local membrane plane.

As discussed above, IBM requires the nodal force at each Lagrangian membrane node. This can be accomplished with the help of the shape functions of the triangular elements according to the finite element theory [9]. The elastic part of the nodal force can also be calculated directly from the energy function according to the virtual work principle

[66, 81]. Other aspects of membrane mechanics, including the bending modulus, area conservation and intercellular aggregation, can be considered as well [9, 66, 81].

### 2.2.3 The Finite-Difference Algorithm for the Maxwell Model

The velocity interpolation in Eq. (2.3) inevitably introduces numerical errors in the calculated membrane velocity. The inaccuracy may appear less significant or even negligible in the node velocity and position. However, when finite-difference calculations are performed to approximate the temporal rate or spatial gradient of such variables, significant noises are observed in the calculated strain rate, even when the flow field itself varies very gently in space and time (see Appendix A). To model the membrane viscosity directly according to the mathematical formulation in Sect. 2.2.2, such finite-difference calculations are necessary. The noises in the calculated strain rate or velocity gradient affect the numerical stability greatly and the simulations cannot proceed. This has been mentioned by Yazdani and Bagchi [9] using the finite volume method as the flow solver, and it has also been noticed in our previous unsuccessful attempts using the lattice Boltzmann method to solve the flow field.

For simplicity and clarity, we employ the Kelvin-Voigt model (Figure 2.1(a)) as an idealization of the membrane viscoelastic behavior described in Sect. 2.2.2. The elastic part of the membrane mechanics is represented by the spring element  $k$  and the viscous part is displayed as the dashpot element  $\mu$ . These two elements are connected in parallel and thus they share the same membrane deformation and strain. Please note that this is just an illustration schematic and the dashpot  $\mu$  can be considered as the shear or dilatational

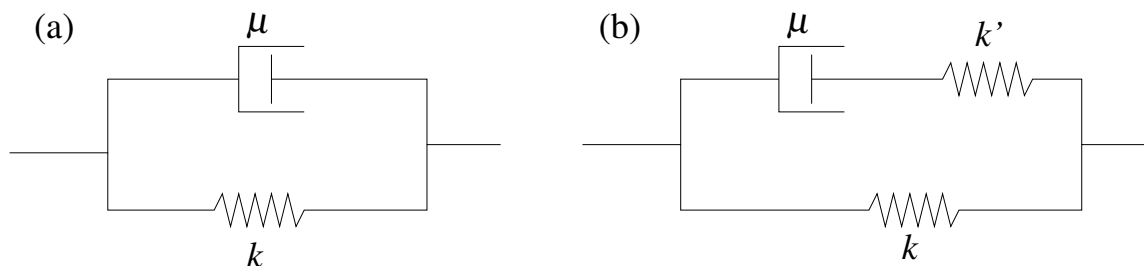


Figure 2.1: Schematic drawings showing (a) the Kelvin–Voigt model for viscoelastic membrane mechanics (spring  $k$  for membrane elasticity and dashpot  $\mu$  for membrane viscosity) and (b) the standard linear solid (SLS) model with an artificial spring  $k'$  added to improve the numerical stability in IBM simulations. In (b) the dashpot  $\mu$  and the spring  $k'$  together form a Maxwell viscoelastic model.

viscous contribution to the membrane stress. In this section, we do not distinguish them for the algorithm description. Since in IBM the flow-membrane coupling process is a strain-imposed problem (i.e., we are calculating the membrane stress from the membrane deformation), the significant errors in strain rate discussed above produce abrupt variations in the viscous stress from the dashpot. To overcome this difficulty in numerical stability, we follow previous practices [9, 58] and add an artificial spring element  $k'$  in series to the dashpot  $\mu$  (Figure 2.1(b)). Now the dashpot  $\mu$  and the new spring  $k'$  form a Maxwell viscoelastic element; and the original Kelvin–Voigt model is transferred into the so-called standard-linear-solid (SLS) model in the viscoelasticity theory [83]. As to be shown in Sect. 2.3.1, when the stiffness of  $k'$  is sufficiently large, its effect on the system performance becomes negligible. However, with the addition of this spring  $k'$ , the stress induced in the Maxwell element under a given strain  $\varepsilon(t)$  cannot be expressed explicitly. Previous attempts used the integral approach [9, 58]; however, several physical and mathematical concerns exist in these implementations, such as the inability to model neo-Hookean membranes for Ref. [58] and the inconsistency between the linear elasticity assumption for the Prony series expression and the neo-Hookean Skalak energy function in Ref. [9]. Here we propose a finite-difference alternative to calculate the stress in the Maxwell element.

We consider the simple 1D situation as shown in Figure 2.1(b), and the algorithm can be extended to a 2D sheet with different shear and dilatational viscosities easily as given in the next section.

Since the dashpot  $\mu$  and the spring  $k'$  are connected in series, the internal stress in these two components is the same as that in the overall Maxwell element

$$\sigma_M = \sigma_\mu = \sigma_{k'} \quad ; \quad (2.11)$$

and the strain of the Maxwell element is the sum of those for the dashpot  $\mu$  and artificial spring  $k'$

$$\varepsilon_M = \varepsilon_\mu + \varepsilon_{k'} \quad ; \quad (2.12)$$

where all these strain terms are defined according to the same undeformed length of the Maxwell element. Here we use  $\sigma$  for the stresses and  $\varepsilon$  for the strains, and subscripts are used to indicate the corresponding components for these properties:  $M$  for the Maxwell element,  $\mu$  for the dashpot  $\mu$ , and  $k'$  for the spring  $k'$ . The stresses and strains in the dashpot  $\mu$  and spring  $k'$  are related via the coefficients for the viscous dashpot and the linear spring as

$$\sigma_\mu = \mu \dot{\varepsilon}_\mu \quad ; \quad \sigma_{k'} = k' \varepsilon_{k'} \quad . \quad (2.13)$$

In this equation,  $\mu$  and  $k'$  have also been used to denote, respectively, the viscosity of the dashpot  $\mu$  and the Hookean coefficient of the spring  $k'$ . Applying the time rate to Eq. (2.12) and utilizing relations in Eqs. (2.11) and (2.13) yield

$$\dot{\varepsilon}_M = \frac{\sigma_M}{\mu} + \frac{\dot{\sigma}_M}{k'} \quad . \quad (2.14)$$

This can be considered as the dynamic constitutive relation for the Maxwell element. For a time interval from  $t - \Delta t$  to  $t$ , we can apply the central finite-difference approximation for the time rate terms

$$\dot{\varepsilon}_M(t - \Delta t/2) \approx \frac{\varepsilon_M(t) - \varepsilon_M(t - \Delta t)}{\Delta t} ; \quad \dot{\sigma}_M(t - \Delta t/2) \approx \frac{\sigma_M(t) - \sigma_M(t - \Delta t)}{\Delta t} . \quad (2.15)$$

In the meantime we write the stress at  $t - \Delta t/2$  as the average of those at  $t - \Delta t$  and  $t$ :

$$\sigma_M(t - \Delta t/2) \approx \frac{\sigma_M(t - \Delta t) + \sigma_M(t)}{2} . \quad (2.16)$$

Using these approximations, Eq. (2.14) now is written as

$$\frac{\varepsilon_M(t) - \varepsilon_M(t - \Delta t)}{\Delta t} \approx \frac{\sigma_M(t - \Delta t) + \sigma_M(t)}{2\mu} + \frac{\sigma_M(t) - \sigma_M(t - \Delta t)}{k'\Delta t} , \quad (2.17)$$

from which the stress term  $\sigma_M(t)$  can then be solved as

$$\sigma_M(t) \approx \frac{(2\mu - k'\Delta t)\sigma_M(t - \Delta t) + 2\mu k'[\varepsilon_M(t) - \varepsilon_M(t - \Delta t)]}{2\mu + k'\Delta t} . \quad (2.18)$$

With the initial condition specified [typically the system dynamics starts from a stress-free state  $\varepsilon_M(0) = 0$  and  $\tau_M(0) = 0$ ], and a time interval  $\Delta t$  being selected properly, the above equation can be employed to calculate the stress in the Maxwell element  $\sigma_M(t)$  from the imposed strain function  $\varepsilon_M(t)$ .

### 2.2.4 The Integrated Algorithm for Membrane Viscosity in IBM

The above description is given for the simple 1D situation as shown in Figure 2.1 for clarity, and the IBM calculation is not involved. Here we describe the detailed algorithm and steps for applying our finite-difference method to IBM simulations with membrane viscosity.

As demonstrated in Appendix A, the finite-difference time interval  $\Delta t$  should be large enough compared to the simulation time step  $\delta t$  to smear the numerical noise from IBM velocity interpolation. On the other hand, a too-large  $\Delta t$  may reduce the finite-difference accuracy in describing the dynamic membrane deformation. In practice, a frequency number  $N$  can be introduced as  $\Delta t = N\delta t$ . This means that we only need to do the viscous stress calculation every  $N$  time steps of simulation and the calculated viscous stress will be used in the next  $N$  steps, until the new viscous stress is calculated. We would call this method the finite-difference method with sub-sampling, since the finite difference estimates are performed by sub-sampling the membrane deformation (although available at every time step) at every  $N$  time steps. We are aware that this practice may induce numerical errors: the viscous stress used in the current time step has been calculated some time before. This could be improved by calculating the viscous stress at each time step  $n\delta t$  ( $n > N$ ) from previously stored stress and strain values at  $(n - N)\delta t$ , however, at a cost of extra memory demand considering the relatively large value of  $N$  (50~200) in the following simulations. Some analysis and tests on the selection of the sub-sampling frequency  $N$  will be presented in Sect. 2.3.2.

Generally, in flow simulations, some initialization work is necessary to start the calculation, and the simulation time is set as  $t = 0$ . After that, the computer program repeats a series of

calculations for one time step  $\delta t$ , and the simulation time proceeds from  $t_i$  to  $t_{i+1} = t_i + \delta t$ . Such calculation cycles are repeated till satisfactory results have been obtained: for example, the results have converged to a certain accuracy for steady simulations or the process of interest has been covered by the simulation for unsteady systems. Below we outline the key steps in one calculation cycle with corresponding equations. Our description focuses on our method for the membrane viscosity, and details on other components such as the computational fluid dynamics methods for flow and the finite element methods for membrane can be found in the literature. At the beginning of the  $i$ -th cycle we have all property values at  $t_{i-1}$  available, from the initialization or the previous calculation cycle.

1. Calculate the membrane node velocity  $\mathbf{u}_m(t_{i-1})$  using Eq. (2.3).
2. Calculate the new membrane node position  $\mathbf{x}_m(t_i)$  via the Euler scheme:

$$\mathbf{x}_m(t_i) = \mathbf{x}_m(t_{i-1}) + \mathbf{u}_m(t_{i-1})\delta t . \quad (2.19)$$

3. Calculate the local membrane strain tensor  $\mathbf{E}(t_i) = \begin{bmatrix} E_{11} & E_{12} \\ E_{21} & E_{22} \end{bmatrix}$  by Eq. (2.8) for each membrane element. Note that the strain tensor  $\mathbf{E}$  is symmetric and  $E_{12} = E_{21}$ .
4. Calculate the elastic membrane stress  $\boldsymbol{\tau}^e(t_i) = \begin{bmatrix} \tau_{11}^e & \tau_{12}^e \\ \tau_{21}^e & \tau_{22}^e \end{bmatrix}$  from the constitutive relationship of the membrane material (such as Eq. 2.4) via Eqs. (2.5-2.7). Details of the implementation of these equations can be found in Refs. [86, 89].
5. Check if the viscous membrane stress needs to be calculated at this time step: If not ( $i \bmod N > 0$ ), skip the calculations in this step, and move to Step 6 to complete the

rest calculations in the cycle; If yes ( $i \bmod N=0$ ), perform the following calculations:

- (a) Calculate the shear ( $E_{11}^s$  and  $E_{12}^s$ ) and dilatational ( $E_{11}^d$ ) strain tensor elements:

$$E_{11}^s = \frac{E_{11} - E_{22}}{2}, \quad E_{12}^s = E_{12}, \quad \text{and} \quad E_{11}^d = \frac{E_{11} + E_{22}}{2}. \quad (2.20)$$

All other elements are directly related to these three ( $E_{21}^s = E_{12}^s$ ,  $E_{22}^s = -E_{11}^s$ , and  $E_{22}^d = E_{11}^d$ ) or simply zeros ( $E_{12}^d = E_{21}^d = 0$ ). The three independent strain elements,  $E_{11}^s$ ,  $E_{12}^s$  and  $E_{11}^d$ , should be stored for next viscous stress calculation after  $N$  time steps.

- (b) Calculate the three independent viscous stress elements from the corresponding strain elements above using the following equations, which are direct modifications of Eq. (2.18):

$$\tau_{11}^{v,s}(t_i) \approx \frac{(4\mu_s - k'_s \Delta t) \tau_{11}^{v,s}(t_{i-N}) + 4\mu_s k'_s [E_{11}^s(t_i) - E_{11}^s(t_{i-N})]}{4\mu_s + k'_s \Delta t}, \quad (2.21)$$

$$\tau_{12}^{v,s}(t_i) \approx \frac{(4\mu_s - k'_s \Delta t) \tau_{12}^{v,s}(t_{i-N}) + 4\mu_s k'_s [E_{12}^s(t_i) - E_{12}^s(t_{i-N})]}{4\mu_s + k'_s \Delta t}, \quad (2.22)$$

$$\tau_{11}^{v,d}(t_i) \approx \frac{(4\mu_d - k'_d \Delta t) \tau_{11}^{v,d}(t_{i-N}) + 4\mu_d k'_d [E_{11}^d(t_i) - E_{11}^d(t_{i-N})]}{4\mu_d + k'_d \Delta t}; \quad (2.23)$$

and other viscous stress elements are

$$\tau_{21}^{v,s} = \tau_{12}^{v,s}, \quad \tau_{22}^{v,s} = -\tau_{11}^{v,s}, \quad \tau_{22}^{v,d} = \tau_{11}^{v,d}, \quad \text{and} \quad \tau_{12}^{v,d} = \tau_{21}^{v,d} = 0. \quad (2.24)$$

The three independent viscous stress elements,  $\tau_{11}^{v,s}$ ,  $\tau_{12}^{v,s}$  and  $\tau_{11}^{v,d}$ , will be used in Step 6 for the next  $N$  time steps.

6. Add the elastic and viscous stresses together for each membrane element:

$$\boldsymbol{\tau} = \boldsymbol{\tau}^e + \boldsymbol{\tau}^{v,s} + \boldsymbol{\tau}^{v,d} = \begin{bmatrix} \tau_{11}^e + \tau_{11}^{v,s} + \tau_{11}^{v,d} , & \tau_{12}^e + \tau_{12}^{v,s} \\ \tau_{12}^e + \tau_{12}^{v,s} , & \tau_{22}^e - \tau_{11}^{v,s} + \tau_{11}^{v,d} \end{bmatrix} . \quad (2.25)$$

7. Convert the total local membrane stress  $\boldsymbol{\tau}$  to nodal forces on the three vertices of each element. See details in Refs. [9, 86].

8. Distribute the nodal forces to neighboring fluid nodes according to Eq. (2.1).

9. Calculate the flow field  $\mathbf{u}(t_i)$  using an appropriate numerical method, with the membrane nodal forces included. Details for this step depend on the particular numerical method employed.

10. Return to Step 1 for the next cycle.

It can be seen from the above algorithm outline that our method has a simple algorithm and introduces very limited extra demand for computation and memory in Step 5.

## 2.3 Results and Discussion

### 2.3.1 Nondimensional Analysis and Numerical Tests for the 1D Maxwell Model

We first conduct nondimensional analysis on the governing equation Eq. (2.14) for the Maxwell element. Introducing the characteristic stress  $\sigma_0$ , strain  $\varepsilon_0$ , and time  $T_0$  for the Maxwell viscoelastic element, the following nondimensional variables can be defined:

$$\sigma_M^* = \frac{\sigma_M}{\sigma_0} ; \quad \varepsilon_M^* = \frac{\varepsilon_M}{\varepsilon_0} ; \quad \dot{\sigma}_M^* = \frac{\dot{\sigma}_M}{\sigma_0/T_0} ; \quad \text{and} \quad \dot{\varepsilon}_M^* = \frac{\dot{\varepsilon}_M}{\varepsilon_0/T_0} . \quad (2.26)$$

Eq. (2.14) is then rewritten to the following nondimensional form:

$$\frac{\tau}{T_0} \dot{\sigma}_M^* + \sigma_M^* = \frac{\mu \varepsilon_0}{T_0 \sigma_0} \dot{\varepsilon}_M^* \quad , \quad (2.27)$$

where  $\tau = \mu/k'$  is the relaxation time of the Maxwell element [83]. The first term on the left hand side of this equation represents the effect from the artificial spring  $k'$ , and the second term represents the effect of the original dashpot  $\mu$ . The coefficient  $\tau/T_0$ , the nondimensional relaxation time, can be considered as the relative weight of  $k'$ -effect compared to that from the dashpot  $\mu$ . The smaller  $\tau/T_0$ , the less significant the role of the artificial spring  $k'$  in determining the overall strain-stress dynamics of the Maxwell element. When using IBM simulating membrane dynamics, the imposed strain is calculated from the membrane deformation. The  $k'$  value should be selected according to the membrane viscosity and the strain variation; the membrane elasticity should not be involved. Yazdani and Bagchi [9] and Gounley and Peng [58] used the ratio of the shear elastic modulus  $k$  to the artificial spring constant  $k'$  as a primary control parameter to justify their selections of the artificial spring constant value. This practice is incorrect according to our nondimensional analysis above as well as our test calculations below in this section.

We next conduct some numerical tests for the 1D Maxwell element in Figure 2.1(b). The membrane elastic part is not involved so it is not considered here. To obtain an analytical solution of the stress, we impose a model deformation

$$\varepsilon_M(t) = \varepsilon_0 [1 - \cos(2\pi t/T_0)] \quad . \quad (2.28)$$

Here  $\varepsilon_0$  serves as the variation amplitude and  $T_0$  as the variation period. Assuming the

system starts from the stress-free state with  $\sigma_M(0) = 0$ , the viscous stress can be solved analytically with the following solution:

$$\sigma_M(t) = \mu \omega \varepsilon_0 \left[ \frac{\sin(\omega t) - \omega \tau \cos(\omega t) + \omega \tau \exp(-t/\tau)}{\omega^2 \tau^2 + 1} \right] , \quad (2.29)$$

where  $\omega = 2\pi/T_0$  is the variation frequency. For a large artificial spring constant  $k'$ , the relaxation time  $\tau = \mu/k'$  approaches 0 and we therefore have  $\omega \tau = 2\pi\tau/T_0 \rightarrow 0$ . Under this situation, the last two terms in the numerator and the  $\omega^2 \tau^2$  term in the denominator in the above equation are negligible, and the solution is simplified to

$$\sigma_\mu(t) = \lim_{k' \rightarrow \infty} \sigma_M(t) = \mu \omega \varepsilon_0 \sin(\omega t) = \mu \dot{\varepsilon}_M(t) , \quad (2.30)$$

meaning the Maxwell element reverses back to the original dashpot  $\mu$  and the effect of the artificial spring  $k'$  disappears. This is consistent with our nondimensional analysis above and will be confirmed next in our test calculations. To quantify the artificial inaccuracy induced by adding the artificial spring  $k'$  to the dashpot  $\mu$ , we define the following discrepancy parameter

$$L = \int_0^{T_0} \frac{[\sigma_M(t) - \sigma_\mu(t)]^2}{[\sigma_\mu(t)]^2} dt , \quad (2.31)$$

where  $\sigma_M(t)$  and  $\sigma_\mu(t)$  are calculated from Eqs. (2.29) and (2.30), respectively.

We calculate this error parameter for systems with various dashpot viscosity  $\mu$ , strain period  $T_0$ , and the spring constant  $k'$  values. The calculated discrepancy  $L$  are plotted in Figure 2.2. The discrepancy  $L$  appears decreasing with  $k'$  linearly in the log-log plot. To achieve a certain accuracy, a larger  $k'$  is required for a larger dashpot viscosity  $\mu$  (Figure

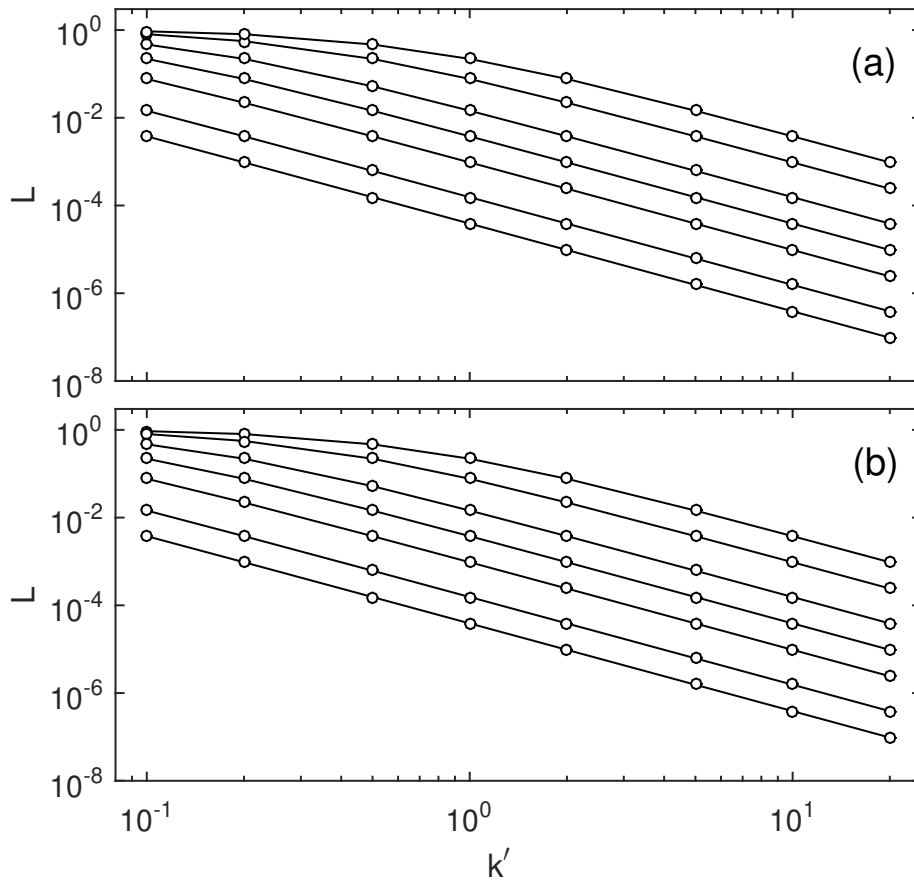


Figure 2.2: The dependence of the artificial error  $L$  on the spring constant  $k'$  under different situations: (a) a constant strain period  $T_0 = 100$  and different dashpot viscosity  $\mu = 0.1, 0.2, 0.5, 1, 2, 5,$  and  $10$  (from bottom to top); and (b) a constant dashpot viscosity  $\mu = 1$  and different strain period  $T_0 = 10, 20, 50, 100, 200, 500,$  and  $1000$  (from top to bottom).

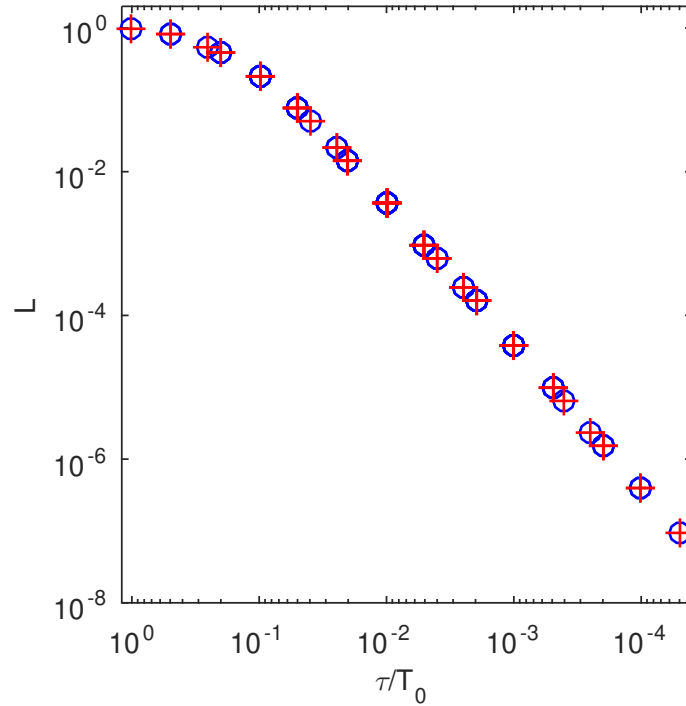


Figure 2.3: The dependence of the artificial error  $L$  on the nondimensional relaxation time  $\tau/T_0$ . This graph covers all data points in Fig. 2.2 with blue circles for data points from Figure 2.2(a) and red crosses for those from Figure 2.2(b). They all fall on a single curve on this graph, indicating the relative error  $L$  only depends on the nondimensional relaxation  $\tau/T_0$ .

2.2(a)) or a smaller variation period  $T_0$  (Figure 2.2(b)). The data points in these two graphs appear identical, even though they were obtained with different system parameters (see details in the caption text of Figure 2.2). Actually, when plotting these  $L$  values versus the nondimensional relaxation time  $\tau/T_0 = \mu/k'T_0$  in Figure 2.3, the 112 data points with various combinations of  $\mu$ ,  $k'$  and  $T_0$  values in Figure 2.2 condense to 21 points and they fall onto a single curve, indicating that there exists a one-to-one relationship between  $L$  and  $\tau/T_0$ . To choose an appropriate value for  $k'$  in IBM simulations, one should compare the relaxation time  $\tau$  to the characteristic time of the membrane variation (such as the rotation period for a capsule in shear flows). The membrane elastic modulus  $k$  is not involved.

We now perform some simple calculations for the 1D Maxwell element under the imposed

strain Eq. (2.28) to validate our finite-difference approach for the viscoelastic stress. We first look at the influence of the finite difference time interval  $\Delta t$  on the calculation accuracy. We take  $\mu = 1$  for the dashpot,  $k' = 0.5$  for the spring, and  $\varepsilon_0 = 1$  and  $T_0 = 20$  for the imposed strain (Figure 2.4(a)), all non-dimensional. Figure 2.4(b) displays the calculated stresses with different  $\Delta t = T_0/5, T_0/10,$  and  $T_0/20$ , and the difference between the calculated and theoretical values are shown in Figure 2.4(c). Fairly good results are observed there even for a coarse finite-difference approximation with  $\Delta t = T_0/5$ , and excellent agreement between the calculated and analytical stresses is achieved when finer resolutions  $\Delta t = T_0/10$  and  $T_0/20$  are adopted. Obviously, the accuracy improves as  $\Delta t$  decreases. We also calculate the relative errors between the calculated and analytical stresses by

$$L_2 = \left[ \frac{\sum (\sigma_{M,n} - \sigma_{M,t})^2}{\sum \sigma_{M,t}^2} \right]^{\frac{1}{2}}, \quad (2.32)$$

where both summations include all available data points in Figures 2.4 (b, c). The calculated  $L_2$  values are: 0.126 for  $\Delta t = T_0/5$ ,  $2.80 \times 10^{-2}$  for  $\Delta t = T_0/10$ , and  $6.70 \times 10^{-3}$  for  $\Delta t = T_0/20$ . Plotting these  $L_2$  errors vs. the finite difference time interval  $\Delta t$  on a log-log graph exhibits a straight line of slope 2.11, suggesting a second order convergence of our method with  $\Delta t$ . However, in actual IBM simulations, the membrane strain calculated from the capsule deformation contains significant noise, and a too small  $\Delta t$  will cause severe numerical instability. The calculations here suggest that our algorithm can provide a reasonably good accuracy with a relatively large interval  $\Delta t$ ; and this aspect is important for IBM simulations. We test  $\Delta t = (50 \sim 200)\delta t$  in our next droplet and capsule simulations and find the difference among them is negligible.

We also conduct calculations with different  $k'$  values to illustrate how our numerical so-

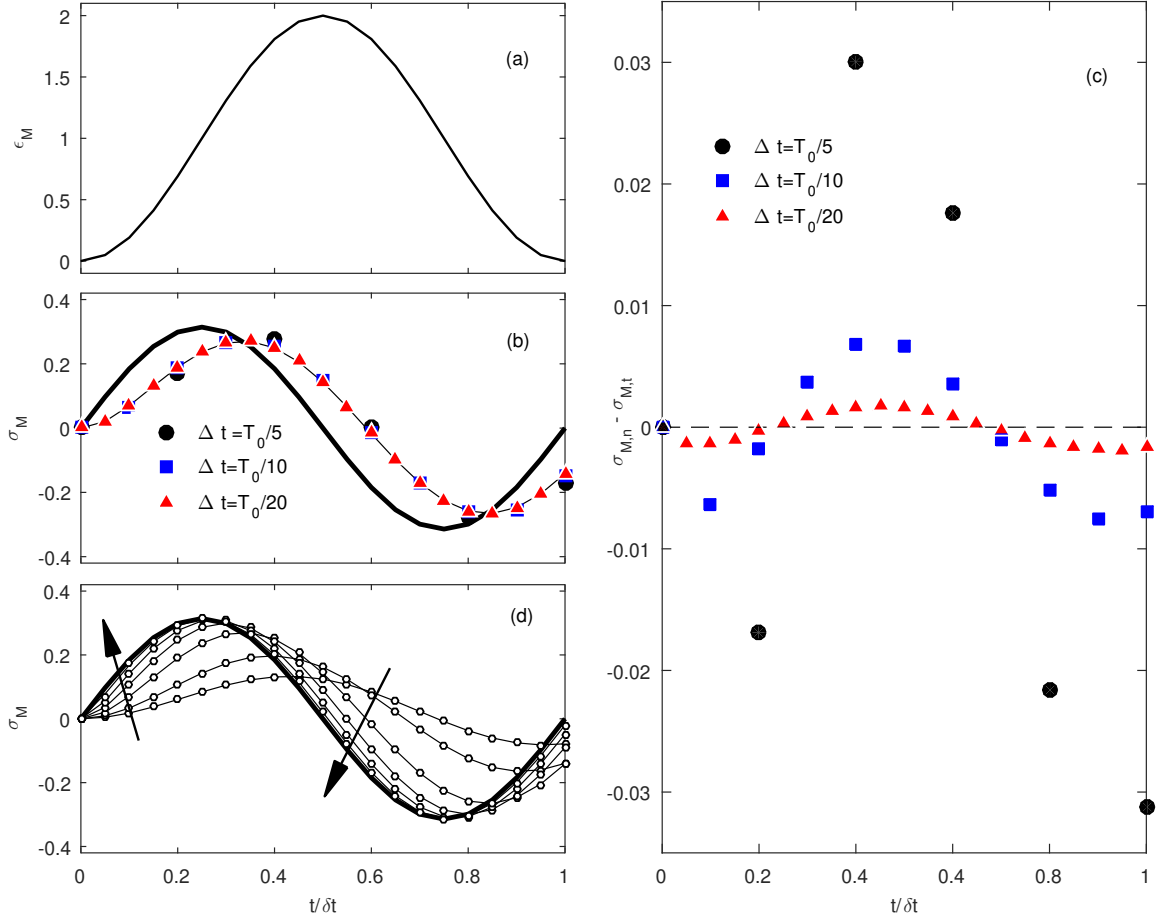


Figure 2.4: Validation of our finite-difference algorithm with the 1D Maxwell model. The imposed strain  $\epsilon_M(t)$  is shown in (a), and the effect of the finite difference time interval  $\Delta t$  is examined in (b). The errors between the numerical results from our finite-difference method using different  $\Delta t$  ( $\sigma_{M,n}$ ) and the theoretical values from Eq. (2.29) ( $\sigma_{M,t}$ ) are displayed in (c). The performance of our algorithm with different spring constant  $k'$  is also displayed in (d). In (b) and (d), the thick lines are the analytical solutions from Eq. (2.30) for the limit of  $k' \rightarrow \infty$ ; the thin lines are obtained from Eq. (2.29); and the symbols are calculated using our method Eq. (2.18). The arrows in (d) indicate the direction of  $k'$  increasing from 0.1, 0.2, 0.5, 1, 2, 5, to 10.

lution agrees to the analytical expression Eq. (2.29) and how it approaches the dashpot solution Eq. (2.30) as  $k'$  increases (Figure 2.4(c)). The time interval  $\Delta t$  is set at  $T_0/20$ . It clearly shows that our numerical solutions match the corresponding analytical solutions very well for all  $k'$  values tested here. As the  $k'$  increases (i.e., the ratio  $\tau/T_0$  decreases), the  $k'$  effect gradually disappears and the Maxwell element reduces back to the simple dashpot

$\mu$ . For  $k' > 2$ , the difference becomes almost indistinguishable in Figure 2.4(d).

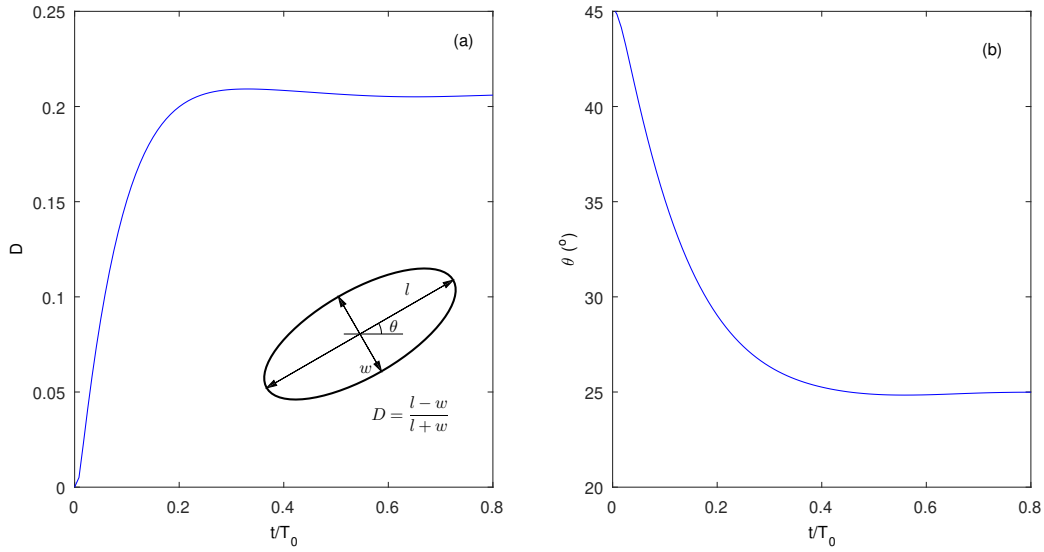


Figure 2.5: Simulated droplet deformation  $D$  (a) and inclination  $\theta$  (b) in shear flow for  $Ca = 0.33$ ,  $\lambda = 1$ ,  $Bq_s = 5$ , and  $Bq_d = 0$ . The inset in (a) shows the definitions of the deformation index  $D$  and inclination angle  $\theta$ .

### 2.3.2 Droplet Deformation in Shear Flow

Although our purpose of this work is for capsule simulations, it can be utilized for droplet dynamics simulations as well, simply by replacing the elastic stress tensor  $\tau^e$  in Eq. (2.6) with  $\gamma\mathbf{I}$ , where  $\gamma$  is the surface tension. The calculation for the viscous stress is the same for membranes and fluid interfaces. The reason for simulating droplet deformation here is to further validate our method by comparing our results to those published in a few previous studies on interfacial viscosity effects [1, 2, 82]. We use the lattice Boltzmann method to solve the flow in a cubic domain with a droplet of radius  $a$  placed at the center. The side length of the cubic computational domain is set as  $2\pi a$  [9]. The ambient fluid viscosity is  $\mu_o$  and the droplet viscosity is  $\mu_i$ . The external shear flow of a shear rate  $\dot{\gamma}$  is generated by applying opposite velocities on the top and bottom domain boundaries.

The characteristic time for this system is chosen as  $T_0 = 1/\dot{\gamma}$ . The initial spherical droplet interface is discretized into 5120 triangular elements. More details on the simulation setup and numerical techniques can be found in Appendix B and Ref. [81]. As in previous studies [1, 2, 82], the following nondimensional numbers are taken as controlling parameters for the system performance:

$$\text{viscosity contrast: } \lambda = \frac{\mu_i}{\mu_o} ; \quad (2.33)$$

$$\text{Capillary number: } Ca = \frac{\mu_o \dot{\gamma} a}{\gamma} ; \quad (2.34)$$

$$\text{Boussinesq numbers: } Bq_s = \frac{\mu_s}{\mu_o a} , \text{ and } Bq_d = \frac{\mu_d}{\mu_o a} . \quad (2.35)$$

To describe the droplet deformation, two parameters are typically utilized: the Taylor deformation index  $D = (l - w)/(l + w)$  ( $l$  and  $w$  represent, respectively, the major and minor axes of the deformed ellipsoidal droplet in the shear plane); and the inclination angle  $\theta$  (the angle between the flow direction and the major axis in the shear plane). See the inset of Figure 2.5(a) for an illustration of the definitions of  $D$  and  $\theta$ . Figure 2.5 shows the droplet deformation processes for a system with  $Ca = 0.33$ ,  $\lambda = 1$ ,  $Bq_s = 5$ , and  $Bq_d = 0$  with  $\Delta t = 100\delta t$  and  $\tau/T_0 = 1/20$ . It can be seen there, as observed in previous studies for droplets and capsules [2, 9, 58, 81], the droplet gradually deforms into a stable ellipsoidal shape with a constant inclination angle in the shear plane. Once the stable state established, the droplet performs the so-called tank-treading rotation with no further apparent change in shape and orientation.

Different finite difference time interval  $\Delta t$  and relaxation time  $\tau$  have been tested for this same system, and the calculated stable deformation and orientation values are compared to

Table 2.1: Simulated droplet deformation  $D$  and inclination  $\theta$  using various finite difference time interval  $\Delta t$  and relaxation time  $\tau$ . The results from Refs. [1, 2] are also provided for comparison.

$N = \Delta t / \delta t$	$\tau / T_0$	Deformation $D$	Inclination Angle $\theta$ ( $^\circ$ )
50	1/20	0.206	25.0
100	1/20	0.206	25.0
200	1/20	0.206	25.0
100	1/10	0.205	25.4
100	1/40	0.207	24.7
Gounley et al. 2016 [2]		0.213	25.4
Flumerfelt 1980 [1]		0.231	31.9

those from the theoretical analysis by Flumerfelt [1] and the boundary integral simulation by Gounley et al. [2] in Table 2.1. It can be seen that the effects of these tested  $\Delta t$  and  $\tau$  values are relatively minor and they yield very close results in both droplet deformation and orientation. It suggests that our method can work well with relatively wide ranges of these parameters; such insensitivity is favorable since it makes the selection of these parameters easier for future applications of this method. Both our results and those by Gounley et al. [2] deviate from the theoretical predictions by Flumerfelt [1] quite noticeably. This should not be surprising since the analysis in Ref. [1] had assumed small droplet deformation. The droplet deformation from our calculations is smaller and the inclination angles are similar when compared to the numerical results in Ref. [2]. Since there are no other results available in the literature, it is inappropriate at present to make further comments on the accuracy of our and Gounley et al.'s methods.

More simulations are performed for droplets in shear flows with different interfacial viscosities and capillary numbers, and the results are plotted in Figure 2.6 as filled symbols. Also shown there are the results from previous studies by Flumerfelt [30] (lines) and Gounley et al. [2] (open symbols). For the droplet deformation, our calculations reveal similar trends for the interfacial viscosity effect as previous studies: The shear viscosity  $Bq_s$  re-

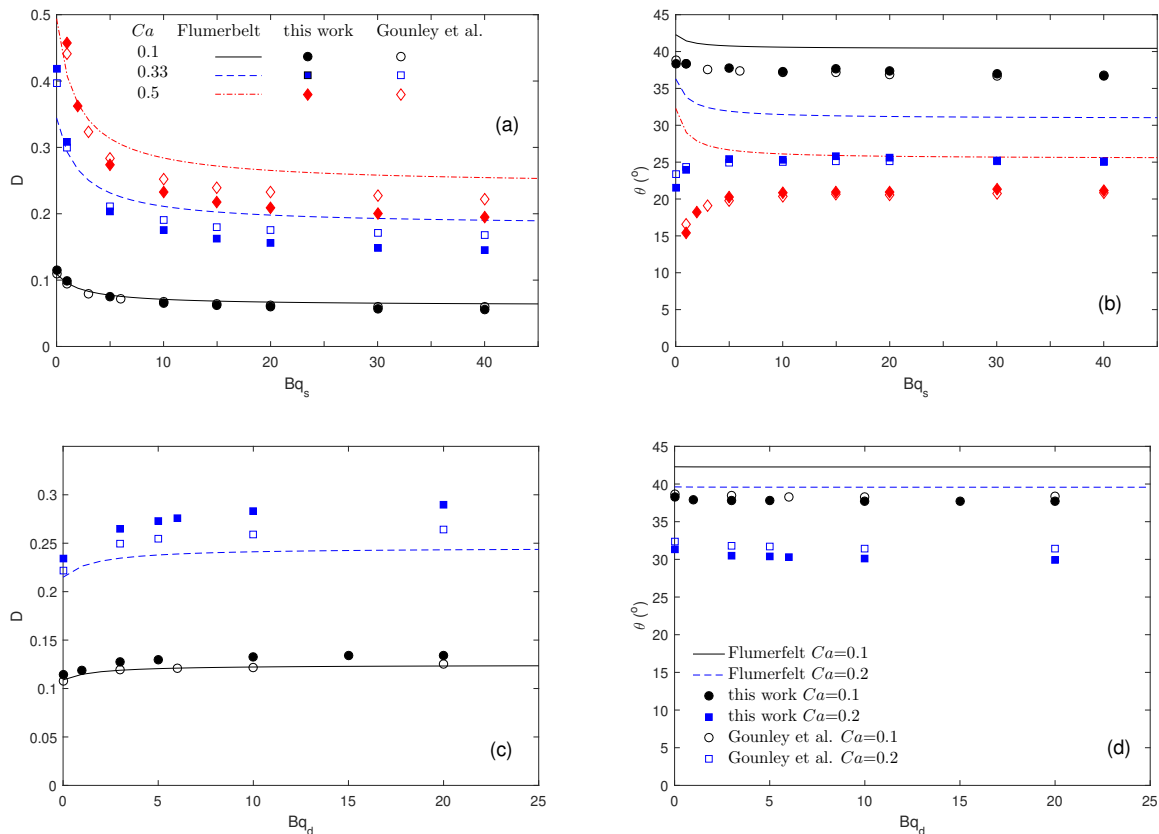


Figure 2.6: Simulated droplet deformation  $D$  (a, c) and inclination angle  $\theta$  (b, d) in shear flow for systems with different Boussinesq numbers  $Bq_s$  and  $Bq_d$ . Results from previous studies [1, 2] are also displayed for comparison.

duces the droplet deformation index  $D$  (Figure 2.6(a)); however, the dilatational viscosity  $Bq_d$  enhances the droplet deformation (Figure 2.6(c)). While the depressing effect of  $Bq_s$  on  $D$  might be anticipated, the enhancing effect of  $Bq_d$  on  $D$  is interesting and somehow counterintuitive. Considering the system complexity here, it is difficult to provide qualitative explanation and analysis for this observation. The increase in droplet deformation  $D$  with the capillary number  $Ca$  is obvious due to the smaller interfacial tension  $\gamma$  associated with a larger  $Ca$ . On the other hand, the dependences of the inclination angle  $\theta$  on interfacial viscosities  $Bq_s$  and  $Bq_d$  are much complicated. In Figure 2.6(b), the Flumerfelt analysis [1] predicts that the inclination angle would always decrease with the shear interfacial viscosity  $Bq_s$ . However, according to numerical results from both the boundary

integral method [2] and the immersed boundary method (our present study), this trend is only true for small deformation  $D$ , and an opposite dependence relationship is observed for larger deformation. Even for the  $Ca = 0.1$  systems with  $D \sim 0.1$ , the agreement between numerical studies and the Flumerfelt theory for  $\theta$  is worse than that for deformation index  $D$ . In Figure 2.6(d), the effect of  $Bq_d$  on  $\theta$  appears much less evident, and the Flumerfelt theory seems over-predict the inclination angle compared to the numerical results from Gounley et al. [2] and this current study. Overall, the effects of  $Bq_s$  and  $Bq_d$  on both  $D$  and  $\theta$  are more dramatic in the low viscosity range. For the systems considered here, the droplet deformation and inclination become approximately constant for  $Bq_s > 20$  and  $Bq_d > 10$ .

When comparing the numerical results from Gounley et al. [2] by the boundary integral method and ours by the immersed boundary method, we find they agree well in the inclination angle  $\theta$  for both the  $Bq_s$  and  $Bq_d$  cases (Figure 2.6(b, d)). The deformation  $D$  from these two studies exhibit very similar variation behaviors with  $Bq_s$  and  $Bq_d$ ; however, obvious differences in magnitude can be seen in Figure 2.6(a, c). Since these are the only two numerical studies available for such systems with interfacial viscosities considered, we are not able to comment on the accuracy. For the few clean droplet situations ( $Bq_s = Bq_d = 0$ ), the results from our calculations and those in Ref. [2], in spite of the differences, are both in the acceptable range from the literature. For example, Ref. [90] collects droplet deformation results in shear flows from various numerical and experimental studies, and it shows a range of  $D = 0.222 \sim 0.250$  for  $Ca = 0.2$ . At this capillary number,  $D = 0.234$  from our calculation falls in the middle and  $D = 0.221$  from Gounley et al. [2] locates at the low end of the reported range.

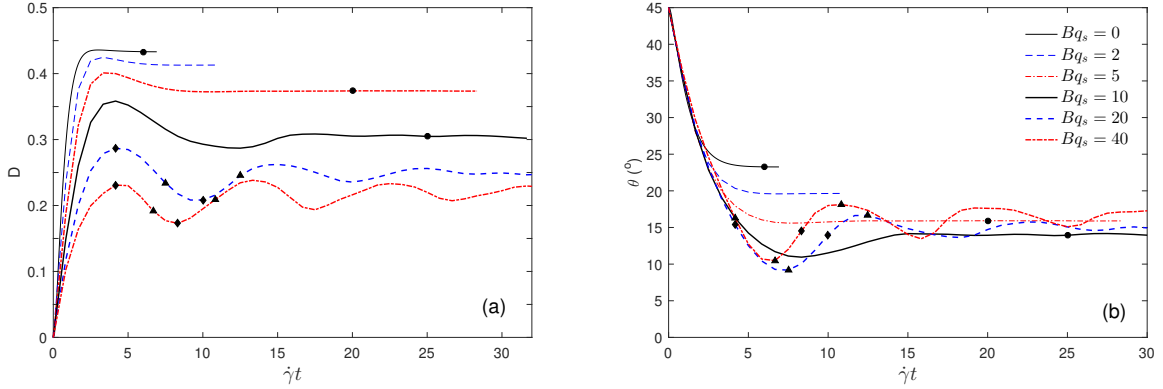


Figure 2.7: Simulated capsule deformation  $D$  (a) and inclination angle  $\theta$  (b) in shear flow with different shear Boussinesq numbers  $Bq_s$ . The symbols indicate the states at which the snapshots in Figure 2.8 are taken.

### 2.3.3 Spherical Capsule Deformation in Shear Flow

As the motivation of this research is to develop a numerical scheme for membrane viscosity, here we apply our method to simulate the deformation processes of spherical capsules in shear flows. The Skalak constitutive relation Eq. (2.4) is adopted for the membrane elasticity and only the shear membrane viscosity is considered (i.e.,  $Bq_d = 0$ ) for the area conservation in typical biological capsules. For the demonstration purpose here, we set  $C = 1$ ,  $\lambda = 1$ , and the capillary number  $Ca = \mu_0 \dot{\gamma} a / E_s = 0.3$ . The only varying parameter in the following simulations is the nondimensional shear viscosity  $Bq_s$ , unless otherwise specified. The simulated capsule deformation  $D$  and inclination angle  $\theta$  are plotted in Figure 2.7. In addition, the initial spherical capsule and several representative deformed shapes are displayed in Figure 2.8. With the absence of membrane viscosity ( $Bq_s = 0$ ), the capsule quickly deforms into a stable ellipsoidal shape with  $D = 0.433$  and  $\theta = 23.3^\circ$  (Figure 2.8(b)). When the shear membrane viscosity increases gradually ( $Bq_s = 2, 5$  and  $10$ ), the developing processes are prolonged and oscillations are noticed in both  $D$  and  $\theta$ . The oscillations eventually die out and a stable droplet shape and inclination are established.

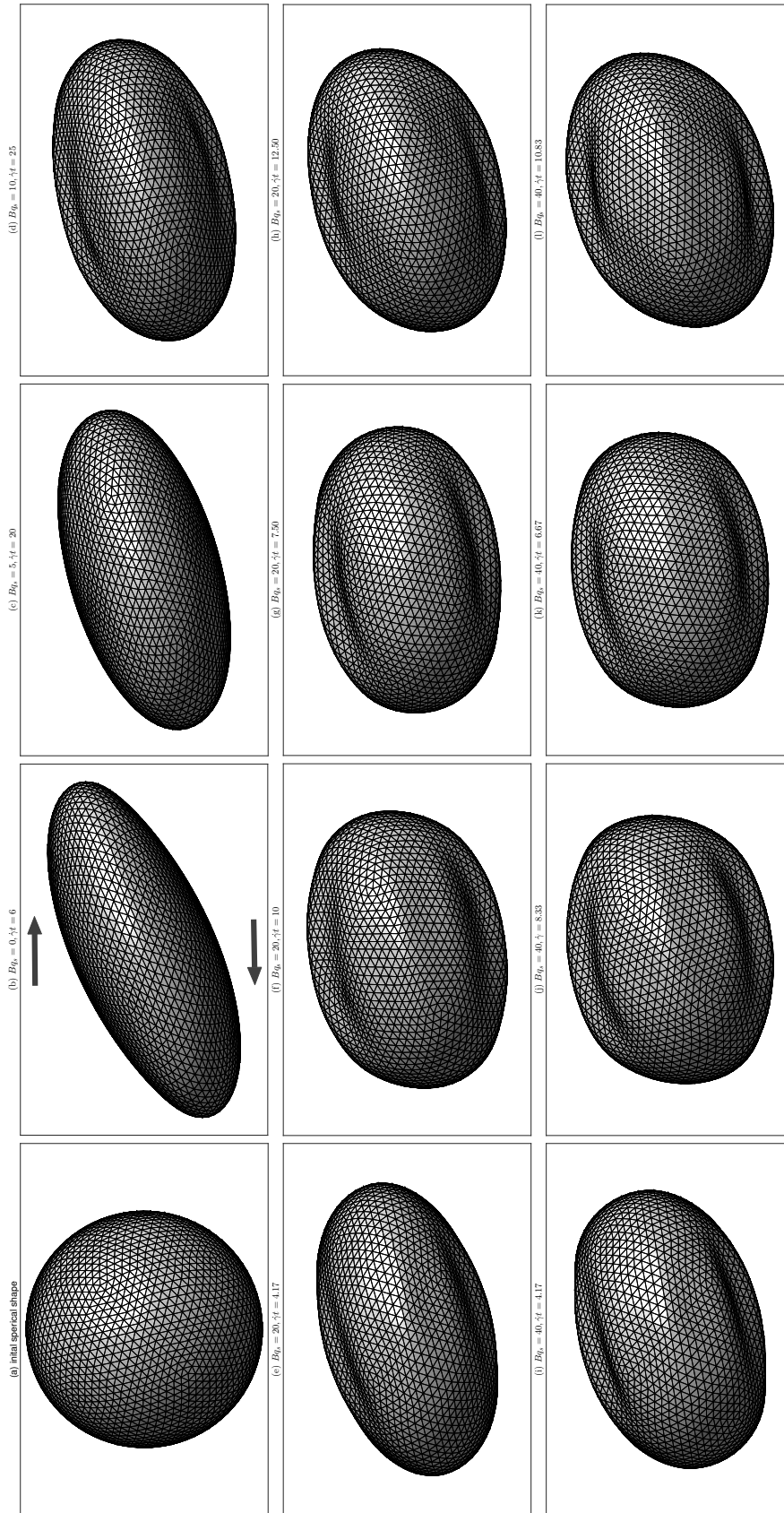


Figure 2.8: The initial (a) and deformed (b-l) capsule shapes selected from simulations in Figure 2.7. The Boussinesq number  $Bq_s$  and the snapshot time for each shape are indicated in the labels. The deformed shapes are taken at the steady states (b-d, circles in Figure 2.7) or at the states with the first maximum or minimum deformations (e-f and i-j, diamonds in Figure 2.7) or inclination angles (g-h and k-l, triangles in Figure 2.7). The arrows in (b) indicate the shear flow direction.

Wrinkles are also developed on the membrane for  $Bq_s = 10$  (Figure 2.8(d)), although the capsule shape and orientation are steady after the initial transient period  $\dot{\gamma}t > 20$ . Further increasing the membrane viscosity ( $Bq_s = 20$  and  $40$ ) results in a higher oscillation frequency and a longer decaying time. The equilibrium deformation index ( $D$  as  $t \rightarrow \infty$ ) keeps decreasing with  $Bq_s$  for these cases, although the decreasing becomes less steep at large  $Bq_s$ . On the other hand, the inclination angle decreases with the shear viscosity first, from  $23.3^\circ$  for  $Bq_s = 0$  to  $\sim 13.9^\circ$  for  $Bq_s = 10$ . After that ( $Bq_s = 20$  and  $40$ ), in addition to the stronger oscillation, the inclination angle starts to increase back: the equilibrium angle is  $\sim 14.9^\circ$  for  $Bq_s = 10$  and  $\sim 16.3^\circ$  for  $Bq_s = 40$ . These values are estimated based on our simulations up to time  $\dot{\gamma}t = 32.5$ . Such behaviors are different from those observed for the  $Bq_s$  effect on droplet deformations in Figure 2.6(a, b), where no oscillations are noticed and both  $D$  and  $\theta$  become insensitive to  $Bq_s > 20$ . The membrane wrinkle patterns appear stable during the deformation and inclination oscillation process for  $Bq_s > 10$  (Figures 2.8d-l). Similar membrane wrinkles have also been reported in previous studies [9, 69]. Despite the concerns regarding the numerical formulations in Refs. [9, 58], similar oscillations have been reported in these previous studies, indicating the membrane viscous effect has been somehow represented in those methods.

The above capsule calculations are performed with a triangular mesh of 5120 membrane elements based on previous studies for non-viscous membranes [66, 81]. Next we examine the mesh-accuracy dependence when the finite-difference method for membrane viscosity is involved. Unlike the general practices in IBM convergence studies where the Lagrangian-Eulerian grid ratio was fixed [91, 92], here we maintain the same Eulerian grid used in above droplet and capsule simulations: the  $120\delta x \times 120\delta x \times 120\delta x$  cubic simu-

lation box and the undeformed capsule radius  $a = 19.10\delta x$ . By doing so we can exclude the Eulerian grid resolution effect on simulation results from the flow solver (the lattice Boltzmann method in this work, see Appendix B for details). Four different membrane meshes are considered:

- Mesh #1: 320 elements with the average edge length of  $5.717\delta x$ ;
- Mesh #2: 1280 elements with the average edge length of  $2.879\delta x$ ;
- Mesh #3: 5120 elements with the average edge length of  $1.442\delta x$ ; and
- Mesh #4: 20480 elements with the average edge length of  $0.721\delta x$ .

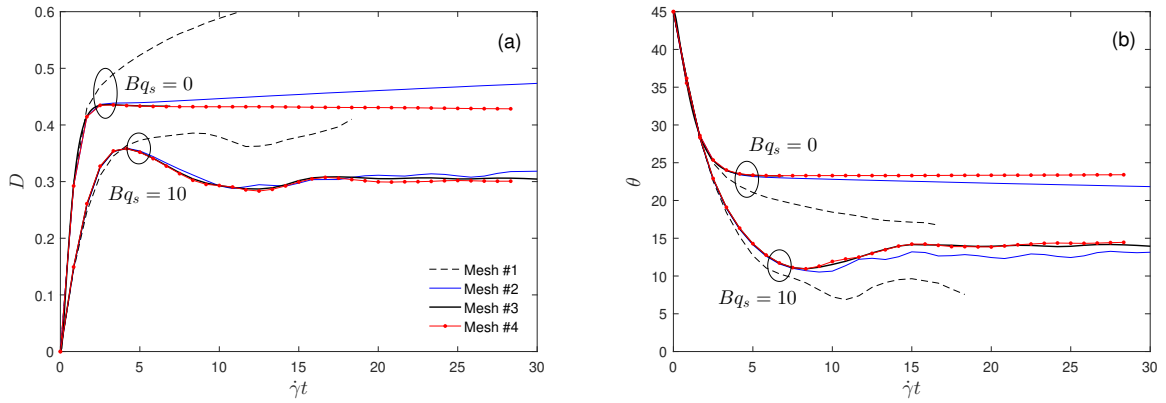


Figure 2.9: Comparisons of the simulated capsule deformation  $D$  (a) and inclination angle  $\theta$  (b) using different membrane meshes.

A finer level mesh is obtained by subdividing each triangular element of a course level mesh into four new elements, and the new nodes are then projected radially onto the sphere surface of radius  $a$  [43]. Mesh #1 is constructed by repeating the subdivision process twice from the regular icosahedron, which has 20 identical equilateral triangular faces. Mesh #3 has been used in the above droplet and membrane simulations. Figure 2.9 displays the capsule deformation index  $D$  (a) and inclination angle  $\theta$  (b) for the  $Bq_s = 0$  and  $Bq_s = 10$

cases. The calculations with Mesh #1 (black dashed lines) do not converge due to the large element size, and the results from Mesh #1 will not be considered in our next discussions. For the case with Mesh #2 at  $Bq_s = 0$ , the simulation does not converge either: the deformation  $D$  keeps increasing and the inclination angle  $\theta$  keeps decreasing, approximately linearly with simulation time (blue lines). However, using the same Mesh #2, the simulation for  $Bq_s = 10$  yields fairly good results in both deformation  $D$  and inclination  $\theta$ . This is probably due to the smaller capsule deformation with  $Bq_s = 10$ , meaning that the capsule is less stretched and therefore the relatively coarse Mesh #2 is less deteriorated. The results from Meshes #3 and #4 match each other very well in Figure 2.9, indicating that Mesh #3 used in above droplet and capsule simulations is fine enough and those simulation results are reliable. It should be noted that, although the average element edge length of Mesh #3 is relatively large ( $1.442\delta x$ ) compared to the Eulerian fluid grid  $\delta x$ , the  $4\delta x$ -thick immersed boundary layer in Eq. (2.2) helps to smooth out the discrete effect from the relatively sparse membrane nodes. For a more explicit comparison, we list the capsule deformation and inclination values at  $\dot{\gamma}t = 4.17$  (the instant of the maximum deformation for  $Bq_s = 10$ ) in Table 2.2a. The relative errors  $E_D$  and  $E_\theta$  between results from two consecutive meshes are also calculated there. We see the error magnitudes in the  $Bq_s = 10$  cases are smaller for  $E_D$  and slightly larger for  $E_\theta$ ; however, we would not overinterpret the differences in these small error values. For example, the inclination angle  $\theta$  has tiny differences between Meshes #3 and #4,  $0.016^\circ$  for  $Bq_s = 0$  and  $0.038^\circ$  for  $Bq_s = 10$ . Such  $< 0.05^\circ$  angle deviations are well acceptable in the literature for droplet and capsule simulations [81, 90].

We also notice that, unlike the small differences listed in Table 2.2a, the deviations in

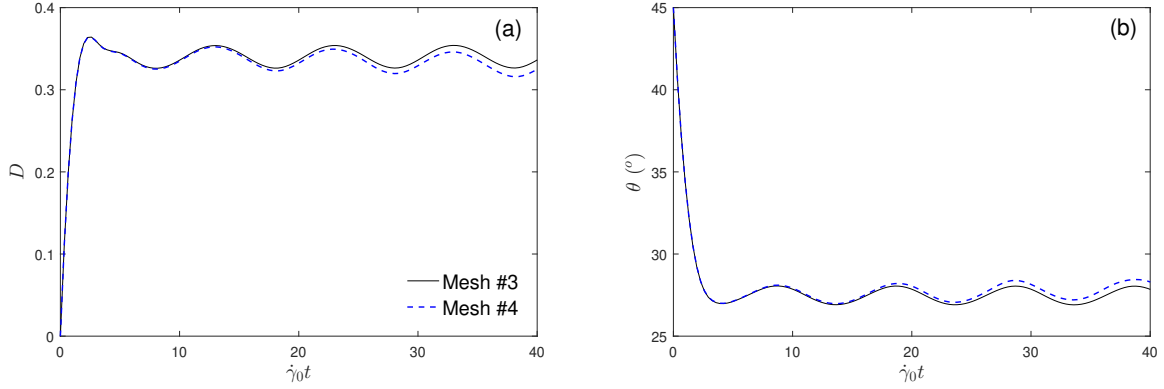


Figure 2.10: Comparisons of the simulated capsule deformation  $D$  (a) and inclination angle  $\theta$  (b) using Meshes #3 and #4 of under dynamic shear with  $Bq_s = 0$ .

both  $D$  and  $\theta$  between Meshes #3 and #4 for  $Bq_s = 10$  become slightly larger later of the simulations ( $\dot{\gamma}t > 10$ , Figure 2.9). Since this is not observed for the  $Bq_s = 0$  cases, which are stable in the later stage, we hypothesize the different behaviors are due to the unsteady capsule dynamics in  $Bq_s = 10$  cases. To verify this assumption, we simulate the capsule dynamics with  $Bq_s = 0$  under a dynamic shear rate  $\dot{\gamma}(t) = \dot{\gamma}_0[1 + 0.1 \sin(2\pi\dot{\gamma}_0 t/10)]$ , which varies about shear rate  $\dot{\gamma}_0$  at an amplitude of  $0.1\dot{\gamma}_0$  and a period of  $10/\dot{\gamma}_0$ . The shear rate  $\dot{\gamma}_0$  is set for a reduced capillary number  $Ca = \mu_0\dot{\gamma}_0 a/E_s = 0.15$  so we can have similar capsule deformations to that for  $Bq_s = 10$  in Figure 2.9(a) [81]. The oscillation period  $10/\dot{\gamma}_0$  is chosen according to the deformation variation curve in  $5 < \dot{\gamma}t < 15$  in Figure 2.9(a). The variations of deformation index and inclination angle in response to this dynamic shear rate are displayed in Figure 2.10. It can be seen there that, similar to the Meshes #3 and #4 curves in Figure 2.9, the agreement between the two sets of results is excellent in the early stage ( $\dot{\gamma}_0 t < 10$ ), and the deviations grow gradually as simulations proceed longer. This clearly confirms our initial hypothesis that the larger deviations in the later stage of simulations for  $Bq_s = 10$  in Figure 2.9 are due to accumulation of numerical errors and they are not introduced by our finite-difference method for membrane viscosity.

Table 2.2: Effects of different membrane mesh resolutions, simulation time steps, and finite-difference schemes on the result accuracy for capsule simulations.

(a) Effect of the membrane mesh resolutions in elastic ( $Bq_s = 0$ ) and viscoelastic ( $Bq_s = 10$ ) capsule simulations.

	Mesh	$D$	$E_D^{(1)}$	$\theta$ ( $^\circ$ )	$E_\theta^{(1)}$
$Bq_s = 0$	Mesh #2	0.4388722		23.40104	
	Mesh #3	0.4345484	$9.96 \times 10^{-3}$	23.51034	$4.65 \times 10^{-3}$
	Mesh #4	0.4342053	$7.92 \times 10^{-4}$	23.52626	$6.77 \times 10^{-4}$
$Bq_s = 10$	Mesh #2	0.3589808		16.18897	
	Mesh #3	0.3583316	$1.81 \times 10^{-3}$	16.29732	$6.65 \times 10^{-3}$
	Mesh #4	0.3583688	$1.04 \times 10^{-4}$	16.33489	$2.30 \times 10^{-3}$

(b) Effect of the simulation time steps in elastic ( $Bq_s = 0$ ) and viscoelastic ( $Bq_s = 10$ ) capsule simulations.

	$\delta t$	$D$	$E_D^{(1)}$	$\theta$ ( $^\circ$ )	$E_\theta^{(1)}$
$Bq_s = 0$	$1.333 \times 10^{-4}$	0.4346157		23.55958	
	$6.667 \times 10^{-5}$	0.4345484	$1.55 \times 10^{-4}$	23.51034	$2.09 \times 10^{-3}$
	$3.333 \times 10^{-5}$	0.4344999	$1.12 \times 10^{-4}$	23.48645	$1.02 \times 10^{-3}$
$Bq_s = 10$	$1.333 \times 10^{-4}$	0.3583676		16.59339	
	$6.667 \times 10^{-5}$	0.3583316	$1.00 \times 10^{-4}$	16.29732	$1.82 \times 10^{-2}$
	$3.333 \times 10^{-5}$	0.3582654	$1.85 \times 10^{-4}$	16.15217	$8.99 \times 10^{-3}$

(c) Comparison of the sub-sampling and moving-average schemes for the finite-difference approximation of strain rate in viscoelastic ( $Bq_s = 10$ ) capsule simulations.

	$D$	$E_D^{(2)}$	$\theta$ ( $^\circ$ )	$E_\theta^{(2)}$
Sub-Sampling Scheme	0.3583316		16.29732	
Moving-Average Scheme	0.3584090	$1.08 \times 10^{-4}$	16.31122	$4.26 \times 10^{-4}$

Notes: (1) The error is calculated by dividing the absolute difference of the two values in the same and above rows of the left column by the value in the same row of the left column. (2) The error is calculated by dividing the absolute difference of the two values in the same and above rows of the left column by the average of them.

Another concern is the time step effect associated with our finite-different method. Similar to the above comparisons for the membrane mesh effect, we simulate the capsule deformation processes for  $Bq_s = 0$  and  $Bq_s = 10$  using three different time steps:  $\delta t = 1.333 \times 10^{-4}$ ,  $\delta t = 6.667 \times 10^{-5}$  and  $\delta t = 3.333 \times 10^{-5}$ , all nondimensional. The intermediate time step  $\delta t = 6.667 \times 10^{-5}$  has been used in our above simulations. The deformation and inclination angle evolution curves would be visually indistinguishable if we plot them in graphs, and thus we list the  $D$  and  $\theta$  values at  $\dot{\gamma}t = 4.17$  in Table 2.2b. Again these values indi-

cate that the time step we use is appropriate and our method has not imposed any more strict requirements on the simulation time step. Furthermore, one anonymous reviewer has suggested the moving-average scheme instead of the sub-sampling scheme for the finite-difference approximation of strain rate. In place of the first equation in Eq. (2.15), the suggested moving-average finite-difference scheme can be expressed as

$$\dot{\epsilon}_M(t - \Delta t/2) \approx \frac{\bar{\epsilon}_M(t - \Delta t/2) - \bar{\epsilon}_M(t - 3\Delta t/2)}{\Delta t} \quad (2.36)$$

for the viscous stress calculation at  $t$ . Here  $\bar{\epsilon}_M$  is the average of strain  $\epsilon_M$  over a finite difference interval  $\Delta t$ :

$$\bar{\epsilon}_M(t - \Delta t/2) = \frac{\sum_{i=0}^{N-1} \epsilon_M(t - i\delta t)}{N}, \quad \bar{\epsilon}_M(t - 3\Delta t/2) = \frac{\sum_{i=0}^{N-1} \epsilon_M(t - \Delta t - i\delta t)}{N}. \quad (2.37)$$

Eqs. (2.21-2.23) should be modified accordingly by replacing the strain elements with these corresponding average values. This scheme is tested with the  $Bq_s = 10$  case. Again because of the excellent agreement to our sub-sampling scheme, we present the result comparison in Table 2.2c instead of using figures. The small relative differences in both  $D$  and  $\theta$  suggests both the sub-sampling and moving-average schemes can be adopted in combination with our finite-difference method for membrane viscous stress calculations.

## 2.4 Summary and Concluding Remarks

We have developed a finite-difference approach with sub-sampling for IBM simulations with membrane viscous effect considered. Due to the inherent numerical noise in the

membrane node velocity, direct implementation of the membrane viscosity in IBM calculations introduces severe numerical instability. Recognizing that the characteristic time of membrane dynamics is typically much larger than the time step of flow simulation, we propose to calculate the membrane viscous stresses via the finite-difference method from the membrane deformation over a time interval. The method has been described in details and its implementation in the general IBM algorithm has been outlined. Compared to the other few methods in the literature for membrane viscosity in IBM, our method has several theoretical and practical advantages, such as the consistency to the classical membrane viscosity definition, the ability to include independent shear and dilatational membrane viscosities, the simple algorithm formulation, and the easy implementation in IBM programs. The method has been further analyzed and validated by comparing our calculated results to theoretical solutions and previous numerical studies. Good agreement was observed in these comparisons. At last, we have also applied our method to simulate the capsule deformation process in shear flow. Our calculations reveal that the membrane viscosity can reduce the capsule deformation and even transfer the capsule motion from tank-treading to oscillation modes. The inclination angle decreases with the membrane viscosity to an apparent minimum value, before strong oscillations in capsule deformation and orientation are observed at high membrane viscosity. Accompanied with the appearance of capsule oscillation, the equilibrium inclination angle starts to increase from the minimum value. Similar behaviors have also been noticed in previous studies [9, 58]. Effects of the membrane mesh resolution and simulation time step have also been carefully examined, and the results show no apparent influence of our method on the simulation accuracy. These validation and demonstration simulations suggest that our method could be a better option for implementing membrane/interfacial viscosity in existing IBM programs for simulating

of droplet and capsule dynamics.

At last, we acknowledge that the main focus of this article is to present the method and algorithm. The simulations conducted in this work just serve the purposes of numerical confirmation, validation, and illustration. We have not attempted to investigate any particular systems or phenomena thoroughly. However, even with the limited cases calculated here, several interesting features have been noticed, including the opposite effects of shear and dilatational interfacial viscosities on droplet deformation, the insensitivity of droplet deformation and orientation to high interfacial viscosities, and the complex capsule response to membrane viscosity. These behaviors as well as their relationships to system parameters all deserve further careful examinations.

## **Acknowledgment**

This work was supported by the Natural Science and Engineering Research Council of Canada (NSERC). The calculations have been enabled by the use of computing resources provided by WestGrid ([westgrid.ca](http://westgrid.ca)), SHARCNet ([sharcnet.ca](http://sharcnet.ca)), and Compute/Calcul Canada ([compute canada.org](http://compute canada.org)). P.L. acknowledges the financial support from the Ontario Trillium Scholarship at Laurentian University. J.Z. thanks Dr. P. Bagchi (Rutgers University) and Dr. A. Yazdani (Brown University) for helpful communications.

## A Demonstration and Analysis of the Numerical Noise in Calculated Strain Rate from the IBM Interpolated Velocity

Here we present a 2D example to demonstrate the numerical noise resulted in the IBM calculated strain rate, and also the improvement from our finite-difference approach with sub-sampling. The flow considered here is the ideal corner flow, for which the stream function is given by

$$\psi = 3x^2y - y^3, \quad (2.38)$$

and the streamlines from this equation are plotted in Figure 2.11(a). We choose one streamline  $\psi = 0.2$  (the blue curve in Figure 2.11(a)), and assume a membrane is moving with the flow along this streamline. This system is purely for the demonstration purpose and one should not interpret it too much physically, such as how to generate this flow and how to force the membrane to move along the streamline. We now considered a point on the membrane, which locates at

$$\left( x_0 = \sqrt{\frac{0.2 + y_0^3}{3y_0}} = \frac{1}{350} \sqrt{\frac{142649}{3}} = 0.623, \quad y_0 = \frac{49}{50} = 0.98 \right)$$

at time  $t = 0$ , indicated as the first circle along the blue streamline in Figure 2.11(a). A time step  $\delta t = 0.0015$  is selected and the point positions  $(x_i, y_i)$  at  $t_i = i\delta t$  are obtained along the streamline. In total 500 such positions are considered in the following discussion, and the positions at every  $50\delta t$  are displayed in Figure 2.11(a) as circles. The particle displacement over each time step varies in a range of  $1.5 \sim 6 \times 10^{-3}$ , which is small enough considering the gentle flow variation in space. A smaller time step  $\delta t = 0.0005$  has also been tested, and

the observations are similar to those to be presented below; however, 1500 time steps are required to cover the same range along the streamline. This process can also be interpreted as the movement of a membrane element: The two nodes of this element locate at  $(x_0, y_0)$  and  $(x_1, y_1)$  at  $t = 0$ , and they move to, respectively,  $(x_i, y_i)$  and  $(x_{i+1}, y_{i+1})$  at  $t = i\delta t$ .

To mimic the discrete flow field from a numerical simulation, we create a  $100 \times 100$  grid for the space in Figure 2.11(a):  $x \in [0, 1]$  and  $y \in [0, 1]$ . The grid resolution is then  $\delta x = 0.01$ . The velocity at such grid nodes can be readily calculated from Eq. (2.38) using the grid node coordinates. The interpolated velocity for the membrane point at  $(x_i, y_i)$  is then obtained from the following 2D version of Eqs. (2.2-2.3):

$$D(\mathbf{x}) = \frac{1}{(4\delta x)^2} \left(1 + \cos \frac{\pi x}{2\delta x}\right) \left(1 + \cos \frac{\pi y}{2\delta x}\right), \quad |x| \leq 2\delta x \text{ and } |y| \leq 2\delta x, \quad (2.39)$$

$$D(\mathbf{x}) = 0, \quad \text{otherwise};$$

$$\mathbf{u}_n(\mathbf{x}_m) = (\Delta x)^2 \sum_{\mathbf{x}_f} D(\mathbf{x}_f - \mathbf{x}_m) \mathbf{u}(\mathbf{x}_f). \quad (2.40)$$

Here the membrane position  $\mathbf{x}_m = (x_i, y_i)$  is calculated above at different  $t_i$  by integrating the theoretical velocity along the streamline, and the fluid velocity  $\mathbf{u}(\mathbf{x}_f)$  is the IBM interpolated velocity at grid node  $\mathbf{x}_f$ . Hereafter, we use the subscript  $n$  for numerical values and the subscript  $t$  for theoretical values from Eq. (2.38). Figure 2.11(b) compares the interpolated ( $u_n$  and  $v_n$ , dashed lines) to the theoretical ( $u_t$  and  $v_t$ , solid lines) velocities along the streamline  $\psi = 0.2$ , and the differences are displayed in Figure 2.11(c). The error in the interpolated velocity is approximately 5% of the velocity magnitude. Please note that this is not relevant to the time step  $\delta t$  (see Eqs. 2.39-2.40), and the errors are purely from IBM interpolation since the flow velocities at grid nodes are exact. In spite of the deviation

noticed here, the velocity and the velocity difference curves in Figures 2.11(b, c) appear smooth with no significant noise.

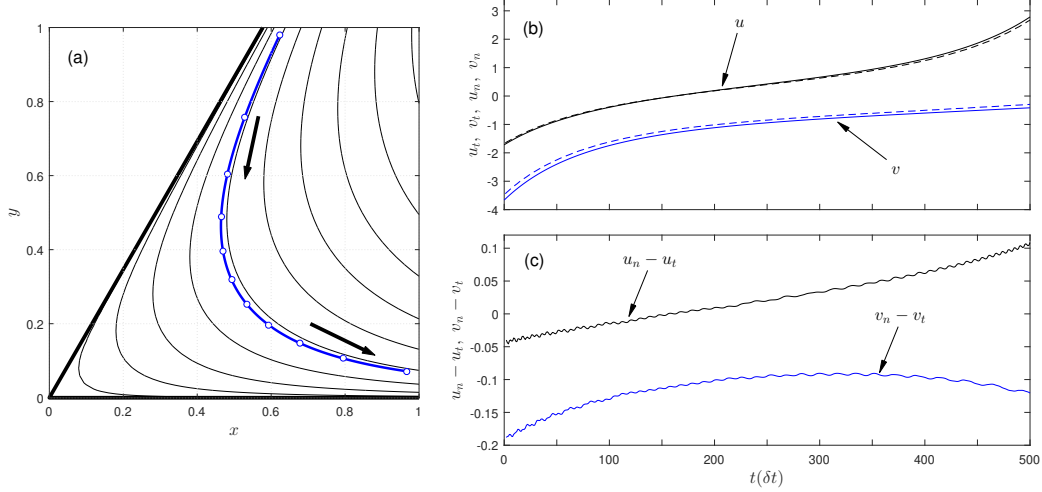


Figure 2.11: (a) The flow streamlines from the stream function Eq. (2.38), (b) the velocities  $u$  and  $v$  along the  $\psi = 0.2$  streamline (blue in a), and (c) the difference between the IBM interpolated velocity and the theoretical velocity from Eq. (2.38). The circles along the  $\psi = 0.2$  streamline in (a) show the positions of a particle along this streamline at different time instances: the first circle at  $t = 0$  and the last at  $t = 500\delta t$  with an interval of  $50\delta t$  between. The time step is  $\delta t = 0.0015$ .

We then examine the strain rate along the streamline calculated from the interpolated velocity  $(u_n, v_n)$  via the backward finite difference with different sampling interval  $N\delta t$  [82, 88]:

$$\dot{\epsilon}_n(\mathbf{x}_i) = \frac{(\mathbf{u}_n, i - \mathbf{u}_n, i-N) \cdot (\mathbf{x}_n, i - \mathbf{x}_n, i-N)}{|\mathbf{x}_n, i - \mathbf{x}_n, i-N|^2}. \quad (2.41)$$

When  $N = 1$ , the sampling interval  $\Delta t = \delta t$  and Eq. (2.41) is simply the regular backward finite-difference scheme. Figure 2.12 displays (a, a') the membrane strain rates obtained analytically ( $\dot{\epsilon}_t$ , solid lines) and numerically using different sampling frequency  $N$  ( $\dot{\epsilon}_n$ , dashed lines and symbols) and (b, b') the difference  $\dot{\epsilon}_n - \dot{\epsilon}_t$  as the membrane particle moving along the streamline. It can be seen that, unlike the relatively smooth curves for the interpolated velocity in Figure 2.11(b), the calculated strain rate from a simple backward

finite-difference scheme with  $N = 1$  (dashed lines in Figure 2.12) exhibits strong noisy variations all the way along the streamline. Clearly, the abruptly varying strain rate  $\dot{\epsilon}_n$  with  $N = 1$  will result in noisy viscous stresses according to Eqs. (2.9) and (2.13), and consequently the sudden variations in membrane nodal forces can damage the numerical stability of the IBM simulations, as mentioned in Ref. [9] and experienced in our previous attempts. The variations in  $\dot{\epsilon}_n$  with  $N = 1$  in Figures 2.12 (b, b') exhibit a smaller amplitude and a lower frequency in the period  $280\delta t < t < 360\delta t$ . The variations also show some periodicity, and the period is  $\sim 5\delta t$  for  $t < 50\delta t$  and  $\sim 15\delta t$  for  $280\delta t < t < 360\delta t$ . To understand this phenomenon more quantitatively, we check the sharp turning points (i.e., local minimums) in Figures 2.12 (b, b'), and find that they all occur when the membrane point crosses a grid line. For example,  $t = 21\delta t$  is one turning point at the early stage of the process, and we have  $y_{20} = 0.8840$  and  $y_{21} = 0.8793$ , indicating that the membrane point has just crossed the  $y = 88\delta x = 0.88$  horizontal grid line. Similarly,  $t = 326\delta t$  is another turning point in the center part of the streamline, and we read  $x_{325} = 0.5598$  and  $x_{326} = 0.5610$ , i.e., the membrane point has just crossed the  $x = 56\delta x = 0.56$  vertical grid line. This analysis clearly suggests that the quasi-periodic variations are induced by the interpolation scheme Eq. (2.40), since whenever a grid line is crossed, a different set of stencil grid nodes  $\mathbf{x}_f$  will be utilized in the interpolation. This yields discontinuity in the interpolated velocity (although almost invisible in Figure 2.11(b)) and the noise becomes much more profound when calculating the strain rate from the interpolated velocity via the regular backward finite-difference method.

When a larger sampling interval  $N\delta t$  is adopted, the improvement in the calculated  $\dot{\epsilon}_n$  is significant. For  $N = 5$  (black circles) and  $N = 10$  (blue squares), we still see some variations in Figure 2.12, but much less dramatic. Further increasing the sampling interval

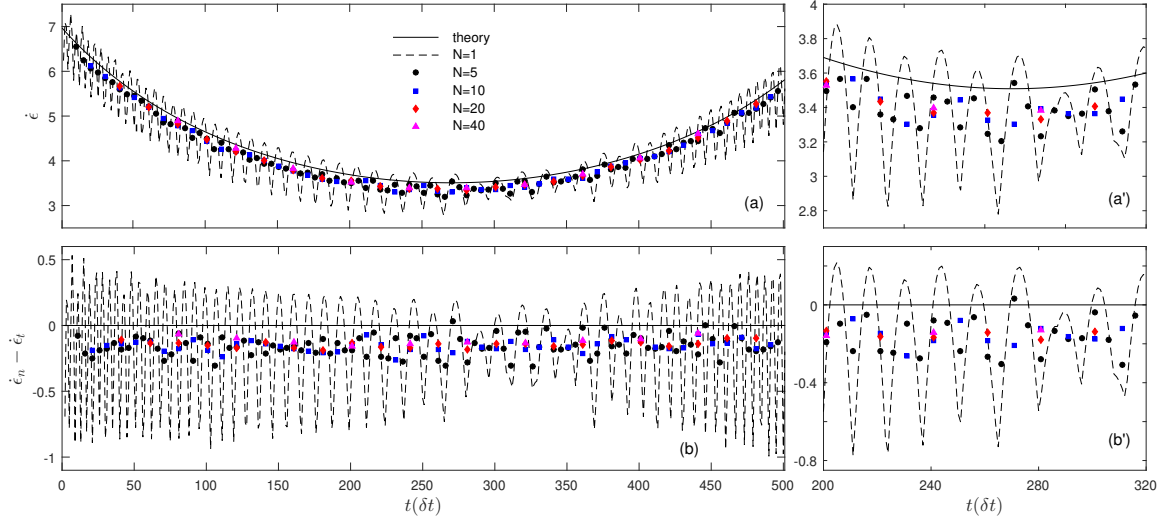


Figure 2.12: (a, a') The strain rates along the streamline  $\psi = 0.2$  from theory (solid lines) and calculated with different finite intervals (dashed lines and symbols), and (b, b') the differences of the calculated strain rates from the theory (dashed lines and symbols). The left panels show the entire time period  $0 \leq t \leq 500\delta t$ , and the right panels enlarge the period  $200\delta t \leq t \leq 320\delta t$  for a better view of details. The black straight lines in (b) and (b') are plotted to indicate the zero-difference state.

to  $N = 20$  (red diamonds) and 40 (purple triangles) can reduce the periodic noise more effectively, and the calculated  $\dot{\epsilon}_n$  appears more stable. We also calculate the  $L_2$  errors by

$$L_2 = \left[ \frac{\sum (\dot{\epsilon}_n - \dot{\epsilon}_t)^2}{\sum \dot{\epsilon}_t^2} \right]^{1/2}, \quad (2.42)$$

where the summations are conducted for all calculated  $\dot{\epsilon}_n$  values. The  $L_2$  errors are:  $8.63 \times 10^{-2}$  for  $N = 1$ ,  $3.93 \times 10^{-2}$  for  $N = 5$ ,  $3.66 \times 10^{-2}$  for  $N = 10$ ,  $3.40 \times 10^{-2}$  for  $N = 20$ , and  $2.88 \times 10^{-2}$  for  $N = 40$ . We do not see a quick decrease in the  $L_2$  errors with the increase in  $N$ , since the difference between  $\dot{\epsilon}_n$  and  $\dot{\epsilon}_t$  in Figure 2.12 does not become smaller as we have  $N$  increased from 20 to 40. The reason for this inefficiency of larger  $N$  values is simple:  $\dot{\epsilon}_n$  is calculated from the interpolated velocity, and the upstream interpolation errors in velocity cannot be removed by the *downstream* finite-difference schemes for the  $\dot{\epsilon}_n$  calculation.

## B The Lattice Boltzmann Method for Flow Field and Simulation Setup

In this work we employ the lattice Boltzmann method (LBM) [93] to solve the flow field. In LBM, the fluid is modeled as pseudo-particles moving over a lattice domain at discrete time steps. The major variables in LBM are the density distributions  $f_i(\mathbf{x}, t)$ , representing the particle amount moving with the  $i$ -th lattice velocity  $\mathbf{e}_i$  at position  $\mathbf{x}$  and time  $t$ . The time evolution of density distributions is governed by the so-called lattice Boltzmann equation:

$$f_i(\mathbf{x} + \mathbf{e}_i \delta t, t + \delta t) = f_i(\mathbf{x}, t) + \Lambda_i(f) \quad , \quad (2.43)$$

which can be considered as a discrete version of the Boltzmann equation in classical statistical physics [93]. Here  $\delta t$  is the time step, and  $\Lambda_i$  is the collision operator incorporating the change in  $f_i$  due to the particle collisions. When an external body force  $\mathbf{F}_f$  (such as gravity or the spread membrane force at fluid nodes in IBM) exists, a forcing term  $f_i^F$  should be added to the right-hand-side of Eq. (2.43) [94]:

$$f_i^F = \alpha_i \left( 1 - \frac{1}{2\tau} \right) \left( \frac{\mathbf{e}_i - \mathbf{u}}{c_s^2} + \frac{\mathbf{e}_i \cdot \mathbf{u}}{c_s^4} \mathbf{e}_i \right) \cdot \mathbf{F}_f \quad . \quad (2.44)$$

The collision operator is typically simplified with the single-time-relaxation approximation [93]

$$\Lambda_i(f) = - \frac{f_i(\mathbf{x}, t) - f_i^{eq}(\mathbf{x}, t)}{\tau} \quad , \quad (2.45)$$

where  $\tau$  is the relaxation parameter. The equilibrium distribution  $f_i^{eq}$  can be expressed as

$$f_i^{eq} = \rho \alpha_i \left[ 1 + \frac{\mathbf{u}^* \cdot \mathbf{e}_i}{c_s^2} + \frac{1}{2} \left( \frac{\mathbf{u}^* \cdot \mathbf{e}_i}{c_s^2} \right)^2 - \frac{\mathbf{u}^* \cdot \mathbf{u}^*}{2c_s^2} \right] . \quad (2.46)$$

Here  $\rho = \sum_i f_i$  is the fluid density and  $\mathbf{u}^* = \mathbf{u} + \delta t \mathbf{F} / (2\rho) = \sum_i f_i \mathbf{e}_i / \rho + \delta t \mathbf{F} / (2\rho)$  is the equilibrium velocity for  $f_i^{eq}$  calculation. Other parameters, including the lattice sound speed  $c_s$  and weight factors  $\alpha_i$ , depend on the lattice structure employed. Through the Chapman-Enskog expansion [94], one can recover the macroscopic continuity and momentum (Navier-Stokes) equations from the above-defined LBM algorithm:

$$\frac{\partial \rho}{\partial t} + \nabla \cdot (\rho \mathbf{v}) = 0 \quad , \quad (2.47)$$

$$\frac{\partial \mathbf{v}}{\partial t} + (\mathbf{v} \cdot \nabla) \mathbf{v} = -\frac{1}{\rho} \nabla P + \frac{\mu}{\rho} \nabla^2 \mathbf{v} + \mathbf{F}_f \quad ,$$

where  $\mu = (2\tau - 1)c_s^2 \delta t / 2\rho$  is the fluid viscosity,  $P = c_s^2 \rho$  is the fluid pressure, and  $\mathbf{v} = \mathbf{u} + \mathbf{F}_f \delta t / (2\rho)$  is the corrected flow velocity.

In this work, we utilize the D3Q19 (3D and 19-lattice velocity) lattice model, and the 19 lattice velocities are .

$$\begin{pmatrix} \mathbf{e}_0 \\ \mathbf{e}_1 \\ \mathbf{e}_2 \\ \vdots \\ \mathbf{e}_{18} \end{pmatrix}^T = \begin{bmatrix} 0 & 0 & 1 & 0 & -1 & 0 & 0 & 1 & 1 & -1 & -1 & 0 & 1 & 0 & -1 & 0 & 1 & 0 & -1 \\ 0 & 1 & 0 & -1 & 0 & 0 & 0 & 1 & -1 & -1 & 1 & 1 & 0 & -1 & 0 & 1 & 0 & -1 & 0 \\ 0 & 0 & 0 & 0 & 0 & 1 & -1 & 0 & 0 & 0 & 0 & 1 & 1 & 1 & 1 & -1 & -1 & -1 & -1 \end{bmatrix} \frac{\delta x}{\delta t} \quad ,$$

where  $\delta x$  is the lattice grid space. The lattice weight factors for the D3Q19 model are  $\alpha_0 = 1/3$ ,  $\alpha_{1-6} = 1/18$ , and  $\alpha_{7-18} = 1/36$ ; and the lattice sound speed is  $c_s = (1/\sqrt{3})\delta x/\delta t$ . The 3D simulation box is  $120\delta x \times 120\delta x \times 120\delta x$  in dimension, and the lattice grid is  $\delta x = 0.0524a$  ( $a$  is the radius of the undeformed droplet or capsule). The simulation time step  $\delta t = 6.667 \times 10^{-4}\dot{\gamma}^{-1}$  ( $\dot{\gamma}$  is the imposed shear rate). As in typical LBM calculations, the initial fluid density is  $\rho(t = 0) = 1$  and the relaxation parameter is  $\tau = 1$ . All these values are nondimensional, and other variables can be calculated from these values once the nondimensional control parameters  $Ca$ ,  $Bq_s$ , and  $Bq_d$  are given. The shear flow is introduced by applying boundary velocities with the same magnitude but opposite directions on the top and bottom boundaries. More details on the simulation setup can be found in Ref. [81].

## **Chapter 3**

### **Finite-Difference and Integral Schemes for Maxwell**

### **Viscous Stress Calculation in Immersed Boundary**

### **Simulations of Viscoelastic Membranes \***

Ping Li and Junfeng Zhang

Bharti School of Engineering, Laurentian University

935 Ramsey Lake Road, Sudbury, ON P3E 2C6, Canada

---

\*This Chapter has been published in *Biomechanics and Modeling in Mechanobiology*, 19(6):2667–2681,

## Abstract

The immersed boundary method (IBM) has been frequently utilized to simulate the motion and deformation of biological cells and capsules in various flow situations. Despite the convenience in dealing with flow-membrane interaction, direct implementation of membrane viscosity in IBM suffers severe numerical instability. It has been shown that adding an artificial elastic element in series to the viscous component in the membrane mechanics can efficiently improve the numerical stability in IBM membrane simulations. Recently Li and Zhang (*Int J Numer Meth Biomed Engng*, 35: e3200, 2019) proposed a finite-difference method for calculating membrane viscous stress. In the present paper, two new schemes are developed based on the convolution integral expression of the Maxwell viscoelastic element. We then conduct several tests for the accuracy, stability, and efficiency performances of these three viscous stress schemes. By studying the behavior of a one-dimensional Maxwell element under sinusoidal deformation, we find that a good accuracy can be achieved by selecting an appropriate relaxation time. The twisting sphere tests confirm that, compared to the numerical errors induced by other components in capsule simulations, such as the finite element method for membrane discretization and IBM for flow-membrane interaction, the errors from the viscous stress calculation are negligible. Moreover, extensive simulations are conducted for the dynamic deformation of a spherical capsule in shear flow, using different numerical schemes and various combinations of the artificial spring constants and calculation frequency for the membrane viscous stress calculation. No difference is observed among the results from the three schemes; and these viscous stress schemes require very little extra computation time compared to other components in IBM simulations. The simulation results converge gradually with the increase

of the artificial spring stiffness; however, a threshold value exists for the spring stiffness to maintain the numerical stability. The viscous stress calculation frequency has no apparent influence on the calculation results but a large frequency number can cause the simulation to collapse. We therefore suggest to calculate the membrane viscous stress at each simulation time step, such that a better numerical accuracy can be achieved. The three numerical schemes have nearly identical performances in all aspects and they can all be utilized in future IBM simulations of viscoelastic membranes.

## **Keywords**

Viscoelastic membrane · Membrane viscosity · Immersed boundary method · Red blood cell · Finite difference method · Integral scheme · Computational fluid dynamics

### 3.1 Introduction

The membrane viscous effect on deformation and dynamics of red blood cells and other biological vesicles has been of interest to fundamental and clinic research for decades [50, 57, 95–97]. Due to the difficulty in direct measurements, numerical simulations become valuable tools for such microscopic biological systems. The immersed boundary method (IBM) [60, 64, 98] has been utilized extensively to study many complex flow systems, including the motion and deformation of biological vesicles and cells in various flow situations [9, 47, 55, 58, 66, 68, 69]. However, numerical instability has been encountered when IBM is applied for viscoelastic biological membranes [9, 99]. Recently, Li and Zhang [99] explored the underlying mechanism and attributed the sudden change in the interpolated velocity when a boundary node crosses the Eulerian grid lines as the cause of the numerical instability. To overcome this difficulty, Yazdani and Bagchi [9] and Gounley and Peng [58] added an artificial spring in series to the viscous component of the membrane, and the stress in the combined Maxwell element was solved using the integral techniques that have been often used in finite element simulations of viscoelastic materials [59, 100]. As pointed out by Li and Zhang [99], several concerns exist in these attempts, including the contradiction between the Prony series expression and the neo-Hookean stress-strain relationship for the artificial elastic spring, the lack of capacity to model general membrane constitutive relationships, and the complex matrix computation required. For a better representation of the viscoelastic membranes in flows, a finite-difference (FD) approach has been developed in Ref. [99]. This method was carefully validated and numerical calculations were performed to demonstrate the membrane viscous effects on capsule deformation

dynamics in shear flows.

Despite the satisfactory performance of the FD algorithm, the successful applications of the integral approach in viscoelastic finite element calculations [59, 100] motivated us to devise appropriate numerical schemes based on the convolution integral expression of membrane viscous stress for IBM simulations. In this paper, two such integral algorithms are presented and their performances in accuracy, stability, and efficiency are compared to the FD method. Results show that all these three numerical models have virtually identical performances in our test simulations and they can be employed for IBM simulations of viscoelastic membranes. The analysis and discussions provide in-depth information on the effects of the numerical schemes and simulation parameters on the overall simulation accuracy, and such information could be helpful for selecting appropriate values for such parameters in future IBM simulations.

The rest of this paper is organized as follows. In Section 3.2, we briefly review the classical formulations for the IBM algorithm and membrane viscoelastic mechanics for biological cells and capsules. In Section 3.3, the FD method from Ref. [99] is described first and then the two new integral schemes for viscoelastic membranes are developed. The three numerical schemes are then evaluated for their performances in accuracy, stability, and efficiency in Section 3.4. At last, Section 3.5 summarizes the results and findings.

## 3.2 Immersed Boundary Method and Membrane Mechanics

### 3.2.1 The Immersed Boundary Method

A flexible membrane may deform significantly under the hydrodynamic interaction between the fluid flow and the membrane, and internal stresses will be developed according to the material constitutive relationship, as to be discussed in Sect. 3.2.2. In IBM simulations, a membrane is represented by a series of boundary nodes, and the membrane force  $\mathbf{F}_m$  at a membrane node  $\mathbf{x}_m$  can be calculated from the membrane stresses using the finite element theory [9, 99, 101]. The nodal force  $\mathbf{F}_m$  is then transferred to nearby fluid nodes  $\mathbf{x}_f$  as a body force  $\mathbf{F}_f$  in the Navier-Stokes equation:

$$\mathbf{F}_f(\mathbf{x}_f) = \sum_{\mathbf{x}_m} D(\mathbf{x}_f - \mathbf{x}_m) \mathbf{F}_m(\mathbf{x}_m) \quad (3.1)$$

where the discrete delta function  $D(\mathbf{x})$  is given by [46]:

$$D(\mathbf{x}) = \frac{1}{(4\delta x)^3} \left(1 + \cos \frac{\pi x}{2\delta x}\right) \left(1 + \cos \frac{\pi y}{2\delta x}\right) \left(1 + \cos \frac{\pi z}{2\delta x}\right), \quad (3.2)$$

$$|x| \leq 2\delta x, |y| \leq 2\delta x, \text{ and } |z| \leq 2\delta x$$

$$D(\mathbf{x}) = 0, \text{ otherwise.}$$

Here  $x, y, z$  are the three elements of location vector  $\mathbf{x}$ , and  $\delta x$  is the Euler grid resolution. Other forms for the function  $D(\mathbf{x})$  have also been proposed in the literature [60, 64, 66].

The membrane nodes move with the ambient flow and the configuration thus deforms continuously. The node velocity  $\mathbf{u}_m(\mathbf{x}_m)$  can be obtained from the flow field  $\mathbf{u}$  via interpolation,

which also uses function  $D$ :

$$\mathbf{u}_m(\mathbf{x}_m) = (\Delta x)^3 \sum_{\mathbf{x}_f} D(\mathbf{x}_f - \mathbf{x}_m) \mathbf{u}(\mathbf{x}_f) \quad . \quad (3.3)$$

Here the summation runs over all fluid nodes with  $D > 0$ . When neglecting the interpolation errors, the interpolated membrane node velocity matches the ambient flow and thus the no-slip requirement between fluid and membrane is satisfied. The membrane node locations can then be updated, for example, using the Euler approximation according to the membrane velocity  $\mathbf{u}_m$ .

### 3.2.2 Membrane Viscoelasticity

For a thin membrane with negligible thickness and mass, the elastic stress caused by in-plane membrane deformation can be obtained from the strain energy function, such as the Skalak function for red blood cell membrane [12]:

$$W_s = \frac{E_s}{8} (I_1^2 + 2I_1 - 2I_2) + \frac{E_a}{8} I_2^2 \quad , \quad (3.4)$$

where  $W_s$  is the strain energy per membrane area, and  $E_s$  and  $E_a$  are, respectively, the shear and dilation moduli.  $I_1$  and  $I_2$  are the strain invariants and they can be calculated from the two principle stretch ratios  $\varepsilon_1$  and  $\varepsilon_2$  in the local two-dimensional (2D) membrane plane as

$$I_1 = \varepsilon_1^2 + \varepsilon_2^2 - 2 \quad ; \quad I_2 = \varepsilon_1^2 \varepsilon_2^2 - 1 \quad . \quad (3.5)$$

The principle stresses associated with these two principle stretch ratios are

$$\tau_1^e = \frac{1}{\varepsilon_2} \frac{\partial W_s}{\partial \varepsilon_1} , \quad \tau_2^e = \frac{1}{\varepsilon_1} \frac{\partial W_s}{\partial \varepsilon_2} ; \quad (3.6)$$

and the principle directions  $\mathbf{e}_1$  and  $\mathbf{e}_2$  can be obtained as the unit eigenvectors of the left Cauchy–Green deformation tensor  $\mathbf{G} = \mathbf{F}\mathbf{F}^T$  with  $\mathbf{F}$  as the deformation gradient matrix [9, 66]. With the membrane being discretized into triangular elements, the matrix  $\mathbf{F}$  can be readily calculated by comparing the deformed and original configurations of each element [86]. The strain tensor  $\mathbf{E}$  is related to matrices  $\mathbf{G}$  or  $\mathbf{F}$  as:

$$\mathbf{E} = \frac{1}{2}(\mathbf{G}^T - \mathbf{I}) = \frac{1}{2}(\mathbf{F}^T \mathbf{F} - \mathbf{I}) . \quad (3.7)$$

The elastic stress tensor  $\tau^e$  can then be obtained from the principle stresses and directions [9, 12]

$$\tau^e = \tau_1^e \mathbf{e}_1 \otimes \mathbf{e}_1 + \tau_2^e \mathbf{e}_2 \otimes \mathbf{e}_2 . \quad (3.8)$$

For dynamic processes, the membrane deformation varies with time, and viscous stresses could be introduced as well in response to the strain change in membrane. The viscous stress  $\tau^v$  in membrane is typically expressed in two parts: the shear viscous stress  $\tau_s^v$  induced by the shear (deviatoric) part of the strain rate tensor  $\mathbf{D}$ , and the dilatational viscous stress  $\tau_d^v$  from the dilatational (hydrostatic) part of  $\mathbf{D}$  [2, 9, 82, 87, 88]:

$$\tau^v = \tau_s^v + \tau_d^v ; \quad \tau_s^v = \mu_s [2\mathbf{D} - \text{tr}(\mathbf{D})\mathbf{I}] ; \quad \tau_d^v = \mu_d \text{tr}(\mathbf{D})\mathbf{I} . \quad (3.9)$$

The coefficients  $\mu_s$  and  $\mu_d$  are the shear and dilatational membrane viscosities, respectively. The matrix  $\mathbf{D}$  is the strain rate tensor of the membrane and  $\mathbf{I}$  is the  $2 \times 2$  unit matrix. The strain rate tensor  $\mathbf{D}$  can be obtained via the membrane velocity gradient [2, 82, 87, 88]

$$\mathbf{D} = \frac{1}{2} [\nabla_m \mathbf{u}_m + (\nabla_m \mathbf{u}_m)^T] \quad , \quad (3.10)$$

where  $\nabla_m$  is the gradient operator and  $\mathbf{u}_m$  is the membrane velocity, both in the local membrane plane. Please note that we work in the local 2D plane of the membrane, and the projection tensor (typically denoted by  $\mathbf{P}$ ) for the three-dimensional strain rate tensor in previous studies [82, 87, 88] is not necessary here.

At last, the total viscoelastic stress  $\tau$  developed in membrane due to its dynamic deformation is simply the sum of the elastic and viscous stresses [9, 82, 87, 88]:

$$\tau = \tau^e + \tau^v. \quad (3.11)$$

With the total viscoelastic stress tensor  $\tau$  obtained from Eq. (3.11), the nodal force at each Lagrangian membrane node can be calculated using the shape functions of the triangular elements according to the finite element theory [9, 99, 101]. Other aspects of the membrane mechanics, such as the bending modulus, area conservation, and intercellular aggregation [9, 66, 81], are not considered in this study for simplicity.

### 3.3 Numerical Schemes for Membrane Viscosity in IBM

#### 3.3.1 The Maxwell Viscoelastic Model for Stability Improvement

The velocity interpolation in Eq. (3.3) inevitably introduces numerical errors in the calculated membrane velocity [99]. When calculating the membrane viscosity directly according to the mathematical formulation in Sect. 3.2.2, the noises in the calculated strain rate affect the numerical stability greatly and the simulations cannot proceed [9, 99]. To improve the system stability, Yazdani and Bagchi [9] proposed to add an artificial spring element in series to the original membrane viscous component; and this technique has been proven to be effective [9, 58, 99].

According to the membrane viscoelastic stress given in Eq. (3.11), the elastic and viscous stresses respond independently to the same membrane strain function. This suggests that membrane viscoelastic behavior can be conceptually visualized by the Kelvin–Voigt model in Figure 3.1(a). The elastic part of the membrane mechanics is represented by the spring element  $k$  and the viscous part is displayed as the dashpot element  $\mu$ . These two elements are connected in parallel and thus they share the same membrane deformation and strain. To improve the numerical stability, we follow previous practices [9, 58] and add an artificial spring element  $k'$  in series to the dashpot  $\mu$  (Figure 3.1b). Now the dashpot  $\mu$  and the new spring  $k'$  form a Maxwell viscoelastic element; and the original Kelvin–Voigt model is transferred into the so-called standard-linear-solid (SLS) model in the viscoelasticity theory [83]. When the stiffness of  $k'$  is sufficiently large, its effect on the system performance becomes negligible [99]. We would like to clarify that the elastic part of the membrane me-

chanics (Eq. 3.8, represented by the spring  $k$  in Figure 3.1) is not involved in the viscous stress calculation, and therefore in the next descriptions, we focus on the viscous stress part only.

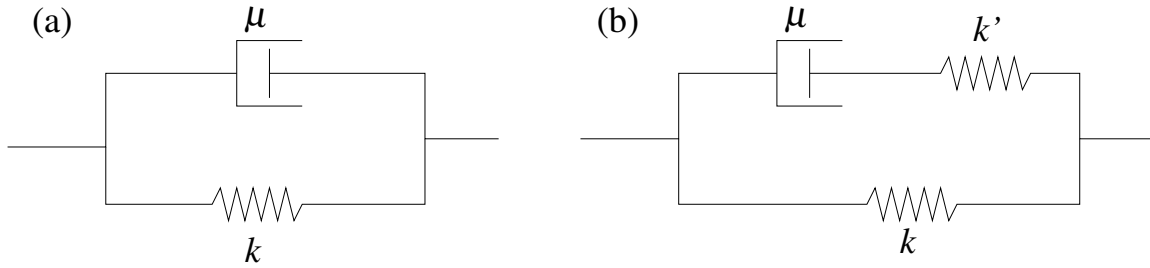


Figure 3.1: Schematic drawings showing (a) the Kelvin–Voigt model for viscoelastic membrane mechanics (spring  $k$  for membrane elasticity and dashpot  $\mu$  for membrane viscosity) and (b) the standard linear solid (SLS) model with an artificial spring  $k'$  added to improve the numerical stability in IBM simulations. In (b) the dashpot  $\mu$  and the spring  $k'$  together form a Maxwell viscoelastic model.

Since the dashpot  $\mu$  and the spring  $k'$  are connected in series, the internal stress in these two components is the same as that in the overall Maxwell element

$$\sigma_M = \sigma_\mu = \sigma_{k'} \quad ; \quad (3.12)$$

and the strain of the Maxwell element is the sum of those for the dashpot  $\mu$  and artificial spring  $k'$

$$\varepsilon_M = \varepsilon_\mu + \varepsilon_{k'} \quad ; \quad (3.13)$$

where all these strain terms are defined according to the same undeformed length of the Maxwell element. Here we use  $\sigma$  for the stresses and  $\varepsilon$  for the strains, and subscripts are used to indicate the corresponding components for these properties:  $M$  for the Maxwell element,  $\mu$  for the dashpot  $\mu$ , and  $k'$  for the spring  $k'$ . The stresses and strains in the dashpot  $\mu$  and spring  $k'$  are related via the coefficients for the viscous dashpot and the linear spring

as

$$\sigma_{\mu} = \mu \dot{\epsilon}_{\mu} \ ; \ \sigma_{k'} = k' \epsilon_{k'} \ . \quad (3.14)$$

In this equation,  $\mu$  and  $k'$  have also been used to denote, respectively, the viscosity of the dashpot  $\mu$  and the Hookean coefficient of the spring  $k'$ . Applying the time rate to Eq. (3.13) and utilizing relations in Eqs. (3.12) and (3.14) yield

$$\dot{\sigma}_M + \frac{1}{\tau} \sigma_M = k' \dot{\epsilon}_M \ , \quad (3.15)$$

where  $\tau = \mu/k'$  is the relaxation time of the Maxwell element [83]. This can be considered as the dynamic constitutive relation for the Maxwell element.

In IBM membrane dynamics simulations, the strain rate in a membrane element is available from the flow field via Eq. (3.10), and the viscous stress is required to calculate the membrane node forces [9, 58, 81]. Unlike the linear, straightforward relation between the viscous stress and strain rate in Eq. (3.9), the explicit solution for the Maxwell viscous stress  $\sigma_M(t)$  from Eq. (3.15) under an arbitrary strain function  $\epsilon_M(t)$  is not available. Therefore, appropriate numerical schemes are necessary to calculate the membrane viscous stress from the membrane strain. Below three numerical methods are presented for this purpose, including the FD method from Ref. [99] and two new methods based on the convolution integral solution of Eq. (3.15). Please note that the above relations and the numerical schemes below are all given for the one-dimensional (1D) Maxwell element in Figure 3.1b, which is just an illustrative representation of membrane mechanics. Table 3.1 lists the necessary substitutions when applying these relations to IBM membrane calculations.

Table 3.1: Parameter substitution for applying the numerical schemes in this work to IBM simulations of viscoelastic membranes.

1D Maxwell Model	Shear Membrane Viscosity	Dilatational Membrane Viscosity
$\varepsilon_M$	$\mathbf{E} - \text{tr}(\mathbf{E})\mathbf{I}/2$	$\text{tr}(\mathbf{E})\mathbf{I}/2$
$\dot{\varepsilon}_M$	$\mathbf{D} - \text{tr}(\mathbf{D})\mathbf{I}/2$	$\text{tr}(\mathbf{D})\mathbf{I}/2$
$\sigma_M$	$\tau_s^v$	$\tau_d^v$
$\mu$	$2\mu_s$	$2\mu_d$
$k'$	$k'_s$	$k'_d$

### 3.3.2 Scheme FD: The Finite-Difference Method for Maxwell Viscous Stress

Consider the IBM membrane simulation currently at time  $t$ . For the time interval from current time  $t$  to  $t + \Delta t$  (where  $\Delta t$  is the finite difference interval for viscous stress calculation), we can apply the central finite difference approximation for the time rate terms in Eq. (3.15) as

$$\dot{\varepsilon}_M(t + \Delta t/2) \approx \frac{\varepsilon_M(t + \Delta t) - \varepsilon_M(t)}{\Delta t} ; \quad (3.16)$$

$$\dot{\sigma}_M(t + \Delta t/2) \approx \frac{\sigma_M(t + \Delta t) - \sigma_M(t)}{\Delta t} . \quad (3.17)$$

In the meantime we write the stress at  $t + \Delta t/2$  as the average of those at  $t$  and  $t + \Delta t$ :

$$\sigma_M(t + \Delta t/2) \approx \frac{\sigma_M(t) + \sigma_M(t + \Delta t)}{2} . \quad (3.18)$$

Using these approximations, Eq. (3.15) now is written as

$$k' \left[ \frac{\varepsilon_M(t + \Delta t) - \varepsilon_M(t)}{\Delta t} \right] \approx \frac{1}{\mu} \left[ \frac{\sigma_M(t) + \sigma_M(t + \Delta t)}{2} \right] + \left[ \frac{\sigma_M(t + \Delta t) - \sigma_M(t)}{\Delta t} \right] , \quad (3.19)$$

from which the stress term  $\sigma_M(t)$  can then be solved as

$$\sigma_M(t + \Delta t) \approx \left( \frac{2\tau - \Delta t}{2\tau + \Delta t} \right) \sigma_M(t) + \left( \frac{2\Delta t}{2\tau + \Delta t} \right) \mu \left[ \frac{\varepsilon_M(t + \Delta t) - \varepsilon_M(t)}{\Delta t} \right] . \quad (3.20)$$

With the initial condition specified [typically the system dynamics starts from a stress-free state  $\varepsilon_M(0) = 0$  and  $\tau_M(0) = 0$ ], and a time interval  $\Delta t$  being selected properly, the above equation can be employed to calculate the stress in the Maxwell element  $\sigma_M(t)$  from the imposed strain function  $\varepsilon_M(t)$ . This method is referred to as the *FD* scheme in the rest of this paper.

### 3.3.3 Scheme Int1: The First Integral Scheme for the Maxwell Viscous Stress

In the viscoelasticity theory [83], the stress in the Maxwell element (Figure 3.1b) under a strain history  $\varepsilon_M(t)$  is given as a convolution integral

$$\sigma_M(t) = k' \int_0^t e^{-\frac{t-s}{\tau}} \dot{\varepsilon}_M(s) ds . \quad (3.21)$$

Similarly, the stress  $\sigma_M(t + \Delta t)$  at time  $t + \Delta t$  can be written as

$$\sigma_M(t + \Delta t) = k' \int_0^{t+\Delta t} e^{-\frac{t+\Delta t-s}{\tau}} \dot{\varepsilon}_M(s) ds , \quad (3.22)$$

which can be further expressed as

$$\sigma_M(t + \Delta t) = e^{-\frac{\Delta t}{\tau}} \sigma_M(t) + k' \int_t^{t+\Delta t} e^{-\frac{t+\Delta t-s}{\tau}} \dot{\varepsilon}_M(s) ds . \quad (3.23)$$

During the small time interval from  $t$  to  $t + \Delta t$ , we assume the strain rate  $\dot{\epsilon}_M$  constant as the finite-difference approximation in Eq. (3.16), and the integral term in Eq. (3.23) can be expressed as

$$\begin{aligned} \int_t^{t+\Delta t} e^{-\frac{t+\Delta t-s}{\tau}} \dot{\epsilon}_M(s) ds &\approx \left[ \frac{\epsilon_M(t+\Delta t) - \epsilon_M(t)}{\Delta t} \right] \int_t^{t+\Delta t} e^{-\frac{t+\Delta t-s}{\tau}} ds \\ &= \tau \left( 1 - e^{-\frac{\Delta t}{\tau}} \right) \left[ \frac{\epsilon_M(t+\Delta t) - \epsilon_M(t)}{\Delta t} \right] . \end{aligned} \quad (3.24)$$

Combining Eqs. (3.23) and (3.24), we now write the stress for the Maxwell element at  $t + \Delta t$  from the previous value at time  $t$  as

$$\sigma_M(t + \Delta t) \approx e^{-\frac{\Delta t}{\tau}} \sigma_M(t) + \left( 1 - e^{-\frac{\Delta t}{\tau}} \right) \mu \left[ \frac{\epsilon_M(t + \Delta t) - \epsilon_M(t)}{\Delta t} \right] . \quad (3.25)$$

This makes up another numerical scheme for membrane viscosity and we refer it as the scheme *IntI* since this is our first method based on the integral stress expression Eq. (3.21). This scheme may appear similar to the formulations in previous integral methods for membrane viscosity [9, 58]; however, fundamental differences exist among them. First, our method treats the artificial spring  $k'$  independently to the membrane elasticity (represented by the spring  $k$  in Figure 3.1). This allows us to use a linear Hookean spring for  $k'$  to apply the convolution integral expression Eq. (3.21), and in the meantime an appropriate constitutive relation for the membrane elasticity, such as the Skalak function Eq. (3.4), can be adopted in IBM simulations. As explained in Ref. [99], requiring the artificial spring  $k'$  to follow the same elastic relation as the membrane is unnecessary and also causes the convolution integral solution Eq. (3.21) invalid. Also, our method avoids the complex matrix computation in Refs. [9, 58], since each element of the membrane viscous stress tensor  $\tau^v$

is obtained individually from the corresponding strain and strain rate elements.

### 3.3.4 Scheme Int2: The Second Integral Scheme for the Maxwell Viscous Stress

The integral term in Eq. (3.23) can also be reformed as follows using the integration by parts rule:

$$\begin{aligned} \int_t^{t+\Delta t} e^{-\frac{t+\Delta t-s}{\tau}} \dot{\varepsilon}_M(s) ds &= \int_{\varepsilon_M(t)}^{\varepsilon_M(t+\Delta t)} e^{-\frac{t+\Delta t-s}{\tau}} d\varepsilon_M \\ &= \left[ \varepsilon_M(s) e^{-\frac{t+\Delta t-s}{\tau}} \right]_t^{t+\Delta t} - \int_{s=t}^{s=t+\Delta t} \varepsilon_M(s) d \left[ e^{-\frac{t+\Delta t-s}{\tau}} \right] . \end{aligned} \quad (3.26)$$

Similar to the approximation for the Maxwell viscous stress  $\sigma_M$  in Eq. (3.17), we assume that the strain  $\varepsilon_M$  during the time interval  $t$  to  $t + \Delta t$  is approximately constant as

$$\varepsilon_M(s) \approx \frac{\varepsilon_M(t) + \varepsilon_M(t + \Delta t)}{2} , \quad s \in [t, t + \Delta t] ; \quad (3.27)$$

and therefore the last term in Eq. (3.26) becomes integrable:

$$\begin{aligned} \int_{s=t}^{s=t+\Delta t} \varepsilon_M(s) d \left( e^{-\frac{t+\Delta t-s}{\tau}} \right) &\approx \left[ \frac{\varepsilon_M(t) + \varepsilon_M(t + \Delta t)}{2} \right] \int_{s=t}^{s=t+\Delta t} d \left( e^{-\frac{t+\Delta t-s}{\tau}} \right) \\ &= \left( 1 - e^{-\frac{\Delta t}{\tau}} \right) \left[ \frac{\varepsilon_M(t) + \varepsilon_M(t + \Delta t)}{2} \right] . \end{aligned} \quad (3.28)$$

Putting these relations together one can obtain the following expression as our second integral scheme *Int2*:

$$\sigma_M(t + \Delta t) \approx e^{-\frac{\Delta t}{\tau}} \sigma_M(t) + \left( 1 + e^{-\frac{\Delta t}{\tau}} \right) \left( \frac{\Delta t}{2\tau} \right) \mu \left[ \frac{\varepsilon_M(t + \Delta t) - \varepsilon_M(t)}{\Delta t} \right] . \quad (3.29)$$

Table 3.2: The coefficients in the general expression Eq. (3.30) for viscous stress  $\sigma_M$  for different numerical schemes and the key assumptions involved in the derivations of these schemes.

Numerical Schemes	FD	Int1	Int2
A	$\frac{2\tau - \Delta t}{2\tau + \Delta t}$	$e^{-\frac{\Delta t}{\tau}}$	$e^{-\frac{\Delta t}{\tau}}$
B	$\frac{2\Delta t}{2\tau + \Delta t}$	$1 - e^{-\frac{\Delta t}{\tau}}$	$\left(1 + e^{-\frac{\Delta t}{\tau}}\right) \left(\frac{\Delta t}{2\tau}\right)$
Assumptions	Eqs. (3.16–3.18)	Eq. (3.16)	Eqs. (3.17) and (3.27)

It is interesting to notice that the three numerical schemes in Eqs. (3.20), (3.25) and (3.29) have similar expressions for the viscous stress  $\sigma_M(t + \Delta t)$ , and we hence write them in the following unified form:

$$\sigma_M(t + \Delta t) \approx A\sigma_M(t) + B\mu \left[ \frac{\varepsilon(t + \Delta t) - \varepsilon(t)}{\Delta t} \right] = A\sigma_M(t) + B\mu \dot{\varepsilon}_M(t + \Delta t/2) \quad , \quad (3.30)$$

with the expressions for coefficients  $A$  and  $B$  varying with different schemes as given in Table 3.2. Also listed there are the key assumptions adopted in the derivations of these schemes.

### 3.4 Results and Discussion

Three numerical schemes are described in the previous section for calculating the membrane viscous stress. Although with similar final expressions, they are established via different mathematical paths and adopt different assumptions. In this section, we examine their performances from three different perspectives, namely the accuracy, stability, and efficiency. The test systems include the 1D Maxwell unit under a cosine-like imposed strain,

the twisting deformation of a spherical shell, and the deformation dynamics of a spherical capsule in shear flow. These systems are carefully designed and selected to serve our evaluation and comparison purposes.

### 3.4.1 1D Maxwell Element Test

To test the validity and accuracy of a numerical algorithm, usually one can compare the results from this algorithm with theoretical or reliable numerical results. Scheme FD has been validated in Ref. [99] by comparing its results to the theoretical solution of the 1D Maxwell model and to the numerical results from boundary integral method simulations for drop deformation and inclination in shear flows with various interfacial viscous situations. No such tests were performed for the previous methods in Refs. [9, 58]. Next, we first apply the three schemes to the 1D Maxwell system in Ref. [99] and examine the effect of the spring constant  $k'$  on the relative errors to the theoretical solution.

We consider the 1D Maxwell element in Figure 3.1b (including the dashpot  $\mu$  and the artificial spring  $k'$ ). The spring  $k$  (representing the elastic part of membrane mechanics) is not involved in the viscous stress calculation and it will not be discussed here. We impose a model deformation

$$\varepsilon_M(t) = \varepsilon_0[1 - \cos(2\pi t/T_0)] \quad , \quad (3.31)$$

where  $\varepsilon_0$  serves as the variation amplitude and  $T_0$  as the variation period. Assuming the system starts from the stress-free state with  $\sigma_M(0) = 0$ , the viscous stress can be solved

theoretically with the following solution:

$$\sigma_{M,t}(t) = \mu \omega \varepsilon_0 \left( \frac{\sin \omega t - \omega \tau \cos \omega t + \omega \tau e^{-t/\tau}}{\omega^2 \tau^2 + 1} \right) , \quad (3.32)$$

where  $\omega = 2\pi/T_0$  is the variation frequency. For a large artificial spring constant  $k'$ , the relaxation time  $\tau = \mu/k'$  approaches 0. Under this situation, the last two terms in the numerator and the  $\omega^2 \tau^2$  term in the denominator in the above equation become negligible, and the solution is simplified to

$$\sigma_{\mu}(t) = \lim_{k' \rightarrow \infty} \sigma_{M,t}(t) = \mu \omega \varepsilon_0 \sin \omega t = \mu \dot{\varepsilon}_M(t) , \quad (3.33)$$

meaning that the Maxwell element reduces back to the original dashpot  $\mu$  only and the effect of the artificial spring  $k'$  disappears.

In our next calculations, we use the following parameters for the Maxwell element: strain variation amplitude  $\varepsilon_0 = 1$ , variation period  $T_0 = 600$ , and dashpot viscosity  $\mu = 100$ . The spring constant  $k'$  varies in a range of  $1 \sim 750$ , and its effect on the accuracy in the calculated viscous stress using different numerical schemes is examined. In addition, two values for the viscous stress calculation interval are considered:  $\Delta t = 1$  and 6. All these parameter values are non-dimensional and they are related to dimensional physical values via characteristic quantities. For example, when using the characteristic time 0.1 s and characteristic force 5 N, the corresponding physical system has the variation period  $600 \times (0.1 \text{ s}) = 60 \text{ s}$ , the dashpot viscosity of  $100 \times (5 \text{ N}) \times (0.1 \text{ s}) = 50 \text{ N}\cdot\text{s}$ , and the artificial spring constant  $k'$

varies in  $(1 \sim 750) \times (5 \text{ N}) = (5 \sim 3650) \text{ N}$ .

To quantify the inaccuracy induced by adding the artificial spring  $k'$  to the dashpot  $\mu$  and the numerical errors from the numerical schemes, we define the following three discrepancy parameters for this 1D Maxwell system:

$$L_0 = \left[ \frac{\sum (\sigma_{M,t} - \sigma_\mu)^2}{\sum \sigma_\mu^2} \right]^{\frac{1}{2}} ; L_1 = \left[ \frac{\sum (\sigma_{M,n} - \sigma_{M,t})^2}{\sum \sigma_{M,t}^2} \right]^{\frac{1}{2}} ; L_2 = \left[ \frac{\sum (\sigma_{M,n} - \sigma_\mu)^2}{\sum \sigma_\mu^2} \right]^{\frac{1}{2}} . \quad (3.34)$$

The stress terms in these equations are:  $\sigma_{M,t}$  - the theoretical stress value of the Maxwell element given by Eq. (3.32),  $\sigma_\mu$  - the dashpot stress as  $k' \rightarrow \infty$  given by Eq. (3.33), and  $\sigma_{M,n}$  - the numerical stress value of the Maxwell element calculated from different schemes. The summations in these equations run through the first period of the strain variation. According to their respective definitions,  $L_0$  represents the artificial effect caused by adding the spring  $k'$  and it is independent of the numerical schemes for viscous stress;  $L_1$  indicates the numerical errors introduced by a specific numerical scheme for the Maxwell element; and  $L_2$  is the overall deviation of the calculated viscous stress  $\sigma_{M,n}$  from the original dashpot stress  $\sigma_\mu$  by a numerical scheme.

Figure 3.2 collects the error values for the 1D Maxwell system discussed above. As the spring constant  $k'$  increases,  $L_0$  decreases, suggesting the artificial effect from  $k'$  becomes less significant for a stiffer spring  $k'$ . A non-dimensional analysis has been conducted for the 1D Maxwell model in Ref. [99], and it shows that error  $L_0$  depends on the non-dimensional relaxation time  $\tau/T_0$  only. This is consistent to the  $L_0$  results in Figure 3.2(a): as  $k'$  increases, the relaxation time  $\tau = \mu/k'$  and therefore the non-dimensional relaxation time  $\tau/T_0$  decrease. To expect a reasonable numerical accuracy, one should select a suf-

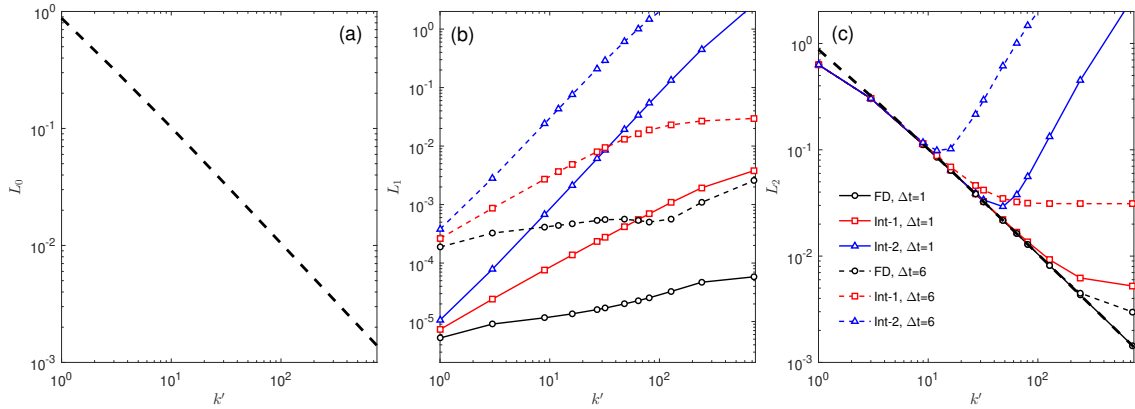


Figure 3.2: Numerical accuracy for the 1D Maxwell element using different artificial spring constant  $k'$ : (a) Error  $L_0$  for the stress discrepancy in the Maxwell element from the original dashpot element; (b) Error  $L_1$  for the stress inaccuracy caused by the numerical schemes FD, Int1, and Int2 for the Maxwell element; and (c) Error  $L_2$  for the overall difference between the numerical calculated Maxwell stress and the original dashpot stress. In (b) and (c), two viscous stress calculation intervals  $\Delta t = 1$  (solid lines) and  $\Delta t = 6$  (dashed lines) are used for each numerical scheme. Also the  $L_0$  line in (a) has been re-presented in (c) as the thick dashed line for a direct comparison of  $L_0$  and  $L_2$ .

ficiently large  $k'$  value such that the Maxwell model does not deviate from the original dashpot too much. When solving the viscous stress using a numerical scheme, additional errors, which are represented by  $L_1$  in Eq. (3.34), are introduced. Figure 3.2(b) shows the  $L_1$  values from different numerical schemes. Unlike the  $L_0$  errors in Figure 3.2(a),  $L_1$  is increasing with the spring constant  $k'$ , especially for the two integral schemes Int1 and Int2. The rapid increase in  $L_1$  for Schemes Int1 and Int2 is due to the assumptions adopted when simplifying the integral terms for the interval  $t \sim t + \Delta t$  in Eqs. (3.24) and (3.28). For large  $k'$  values, the relaxation time  $\tau = \mu/k'$  can be comparable to or even smaller than the time interval  $\Delta t$ . In such situations, the value of the exponential term  $e^{-(t+\Delta t-s)/\tau}$  in the first integral in Eqs. (3.24) and (3.28) varies largely in the  $t \sim t + \Delta t$  interval, and this makes the approximations there less accurate. On the other hand, for Scheme FD, the assumptions Eq. (3.16) and (3.17) are applied to rate terms in the original differential equation Eq. (3.15), and thus the accuracy is less sensitive to the  $\tau$  decrease caused by the  $k'$

increase. Nevertheless, a large  $k'$  value can amplify the finite difference error for  $\dot{\epsilon}_M$  in Eq. (3.15), and consequently increase the  $L_1$  error for Scheme FD as well in Figure 3.2(b). As for the effect of the viscous stress calculation interval  $\Delta t$ , obviously a larger  $\Delta t$  makes the assumptions less accurate for the numerical schemes, and this is evident in Figure 3.2(b).

The overall error  $L_2$  in Figure 3.2(c), although not a simple sum of  $L_0$  and  $L_1$ , can be considered as a combination of the opposite effects of  $k'$  on the calculated viscous stress: the favorable lower  $L_0$  from the smaller non-dimensional relaxation time  $\tau/T_0$  versus the unfavorable larger  $L_1$  due to the less accurate assumptions in the numerical schemes. For low  $k'$  values, the viscous scheme error  $L_1$  is small, the overall error  $L_2$  is dominated by the relatively large artificial spring error  $L_0$ , and the difference among numerical schemes is indistinguishable. On the other hand, at the larger  $k'$  end, the increase in  $L_1$  surpasses the decrease in  $L_0$ . As a result, the overall error  $L_2$  starts to deviate from the declining trend of  $L_0$ . For Scheme Int2, the fast growing of  $L_1$  with  $k'$  quickly turns the overall error  $L_2$  from declining to increasing and V-shape  $L_2$  profiles are produced in Figure 3.2(c). The turning point shifts to the left at the larger  $\Delta t$  because of the larger  $L_1$ . For Scheme FD, because of the small magnitude and the slow increase in  $L_1$  ( $10^{-5} \sim 10^{-4}$ ) for  $\Delta t = 1$ , the overall error  $L_2$  follows the  $L_0$  line (dashed thick line) up to the maximum  $k'$  value in our test. For the Scheme FD with  $\Delta t = 6$ , the effect of  $L_1$  only becomes apparent after  $k' > 100$ .

Scheme Int1 has intermediate  $L_1$  values in Figure 3.2(b) and correspondingly its  $L_2$  curves lie between those from Schemes FD and Int2 in Figure 3.2(c). It is also interesting to notice that, at very low  $k'$  values ( $k' < 3$ ), we have the overall error  $L_2$  less than the artificial spring error  $L_0$ , implying that the inaccuracy from the numerical schemes, by chance, has reversed

the error induced by the artificial spring.

Figure 3.2 and the above analysis suggest that, for a reasonable overall accuracy in the calculated viscous stress, the spring constant  $k'$  should be selected such that the relaxation time  $\tau$  is sufficiently smaller than the characteristic time  $T_0$  of the strain variation, and meanwhile sufficiently larger than the viscous stress calculation time interval  $\Delta t$ . Fortunately, in general IBM simulations, the capsule deformation process (corresponding to the strain variation) is orders longer than the calculation time interval, and the above requirement for  $k'$  is not difficult to meet. In addition, with the large difference between  $T_0$  and  $\Delta t$ , a relatively large  $k'$  value can be utilized to reduce the overall error  $L_2$  without triggering the severe deviation of  $L_2$  from  $L_0$  in Figure 3.2(c).

### 3.4.2 Twisting Spherical Shell Test

The 1D Maxwell model investigated above is a highly simplified representation of the viscous effect in biological membranes. It is helpful for our analysis of the numerical accuracy of individual schemes; however, for practical IBM simulations of biological capsules, the overall accuracy of the simulation results depends on many other factors, including the discretization and resolutions for the fluid domain and the membrane surface, the numerical method for solving the flow field, and the IBM algorithm for the flow-membrane interaction. While it is out of the scope of this current research to conduct a comprehensive study of their individual and coupled effects, here we present some demonstration results for the relative magnitudes of individual effects from membrane discretization and force calculation, IBM velocity interpolation, and our numerical schemes for viscous stress.

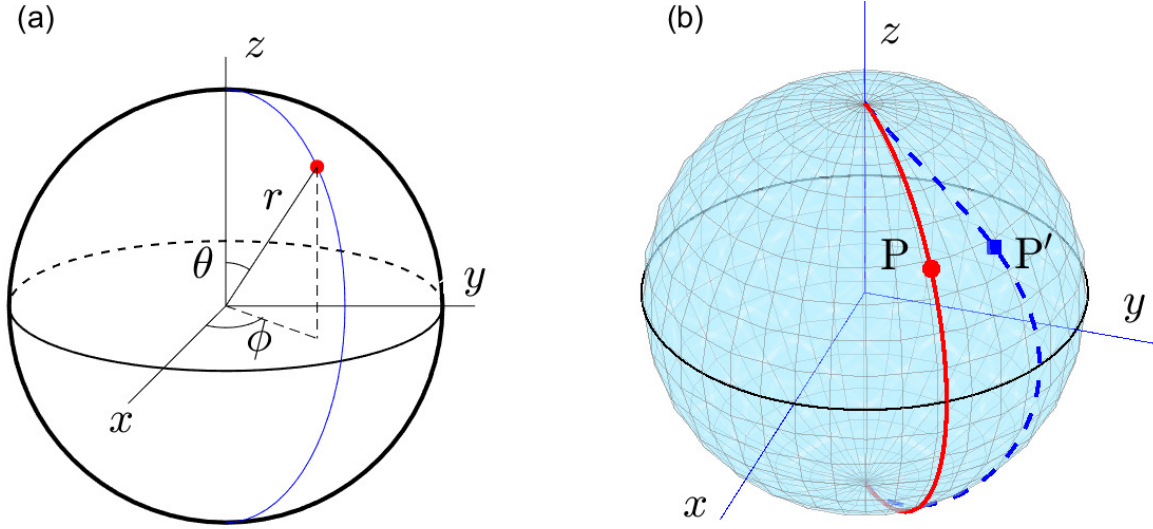


Figure 3.3: (a) The spherical coordinate system adopted in the twisting sphere test and (b) a schematic visualization of the surface deformation under Eq. (3.35): The original  $\phi=\text{constant}$  arc (solid line) deforms into the dashed curve, and the position of a surface point originally at  $P$  moves to the new position  $P'$ .

Consider a spherical surface with radius  $R$  shown in Figure 3.3. The position of a point on this shell surface is denoted by the polar angle  $\theta$  and the azimuthal angle  $\phi$  (Figure 3.3(a)). To generate strain and stress in the shell, we impose the following artificial dynamic displacement in the azimuthal angle  $\phi$ :

$$\phi(t) = \phi_0 + A_0 \sin \theta (1 - \cos \omega t) \quad , \quad (3.35)$$

where  $\phi_0$  is the original azimuthal angle at  $t = 0$ ,  $\omega$  is the twisting frequency and therefore the period is  $T_0 = 2\pi/\omega$ , and  $A_0$  is the twisting amplitude. This particular deformation is designed such that non-uniform strain and stress variations are developed in the shell surface and analytical solutions for the strain and stress are attainable. The velocity on the shell surface from this deformation is

$$u_r = u_\theta = 0 \quad ; \quad u_\phi(t) = R \sin \theta \frac{d\phi(t)}{dt} = A_0 R \omega \sin^2 \theta \sin \omega t \quad . \quad (3.36)$$

Then the strain rates can be obtained from the velocity and the only non-zero item is the shear element

$$\dot{\epsilon}_{\theta\phi}(t) = \dot{\epsilon}_{\phi\theta}(t) = \frac{A_0\omega}{4} \sin 2\theta \sin \omega t \quad . \quad (3.37)$$

This expression is similar to that in Eq. (3.33) for the 1D Maxwell system and thus the corresponding viscous stress developed in the shell surface is

$$\sigma_{\phi\theta}(t) = \sigma_{\theta\phi}(t) = \frac{A_0\omega\mu_s}{4} \sin 2\theta \left( \frac{\sin \omega t - \omega\tau_s \cos \omega t + \omega\tau_s e^{-t/\tau_s}}{\omega^2\tau_s^2 + 1} \right) \quad , \quad (3.38)$$

where  $\tau_s = \mu_s/k'_s$  is the relaxation time from the shear viscosity  $\mu_s$  and the artificial membrane elasticity  $k'_s$  for shear viscous stress calculation.

In our next calculations, the shell surface with  $R = 20$  is discretized into 5120 triangular elements, similar to those in typical IBM capsule simulations [9, 66, 81]. The shear membrane viscosity is set as  $\mu_s = 10$  and the corresponding artificial elasticity is  $k'_s = 0.1$ , resulting in a relaxation time  $\tau_s = 100$ . The deformation defined in Eq. (3.35) does not introduce any dilatational strain in the shell surface and thus the dilatational viscosity is not involved in this twisting shell system. The membrane elasticity is not involved either in the following tests of viscous stress calculation algorithms. The variables for the deformation dynamics are: the variation period is  $T_0 = 10^4$  and the angle variation amplitude is  $A_0 = \pi/18$ . The time interval for viscous stress calculation is taken as  $\Delta t = 1$ . Based on our analysis above, with this large difference between  $\tau_s$  and  $\Delta t$ , the performances among the three schemes (FD, Int1, and Int2) would be very close, as to be seen below.

Two groups of calculations are conducted here. First, we use Eq. (3.35) to calculate the surface node positions changing with time, and the strain of each triangular element is

calculated from the positions of its three nodes using the finite element method (FEM) [66, 101]. The viscous stress is then obtained from the calculated strain via one of the three numerical schemes. We call this method as the *twisting surface* approach. Please note that IBM is not involved in this approach. Considering that the purpose for the viscous stress schemes is for IBM simulations of viscoelastic membranes, we extend the surface velocity in Eq. (3.36) to the space surrounding the sphere surface:

$$u_r = u_\theta = 0 \quad ; \quad u_\phi(r, \theta, t) = A_0 \omega r \sin^2 \theta \sin \omega t \quad . \quad (3.39)$$

Assuming the surface at  $r = R$  is moving with this swirling flow with no relative slip, the surface velocity Eq. (3.36) and surface position Eq. (3.35) can be recovered exactly. In our second group of calculations, we use Eq. (3.39) to define the flow velocity at Eulerian nodes. As in typical IBM simulations, the surface node velocity is obtained via local interpolation Eq. (3.3), and the surface node position is then updated according to this interpolated velocity. The rest steps are the same as the first group: The element strain is calculated from the node positions via FEM, and one viscous stress scheme can be used to find the viscous stress in the element. This later method is termed as the *swirling flow* approach.

Figure 3.4 collects the shear strain rate (left panels) and viscous stress (right panels) results from the FD scheme at  $t/T_0 = 1/4$  and  $t/T_0 = 3/4$  (dots) and compares them to the theoretical solutions Eqs. (3.37) and (3.38) (solid lines). The strain rate and stress values have been normalized, respectively, with respect to the following nominal strain rate  $\dot{\epsilon}^*$  and  $\sigma^*$ :

$$\dot{\epsilon}^* = A_0 \omega / 4, \quad \sigma^* = \mu_s \dot{\epsilon}^* \quad (3.40)$$

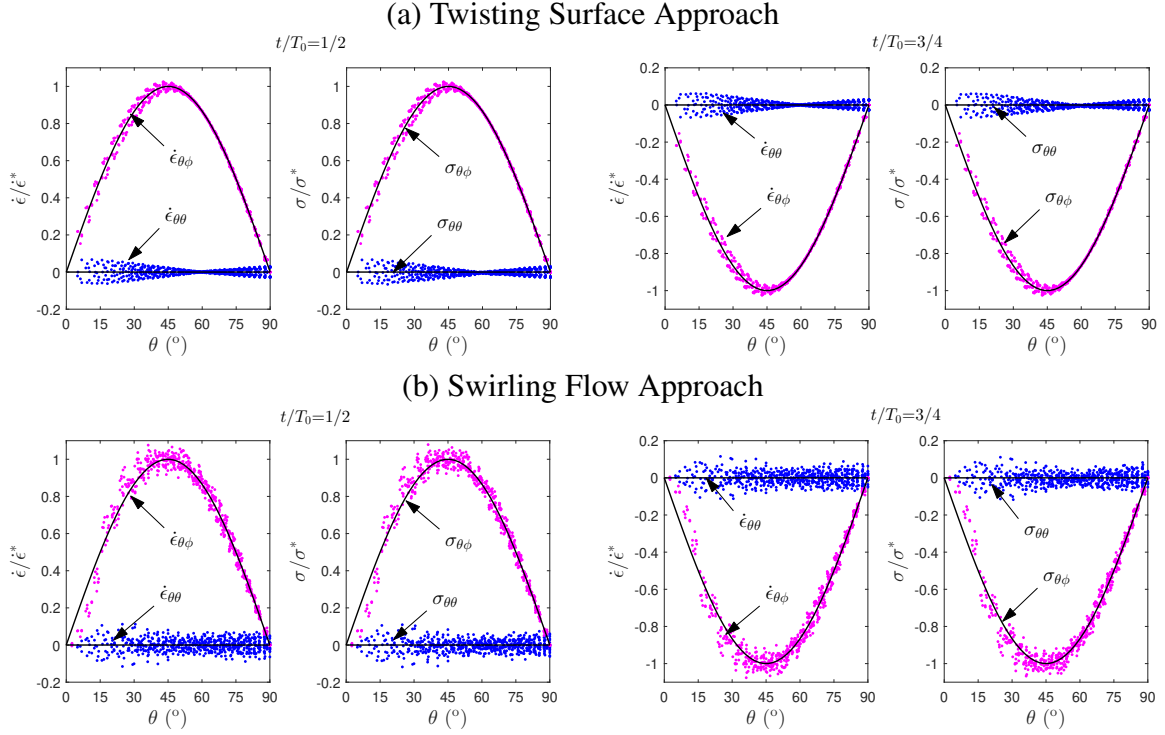


Figure 3.4: Comparisons of the calculated strain rates (left panels) and viscous stresses (right panels) using Scheme FD (symbols) with theoretical solutions (solid lines) in the spherical shell under the twisting deformation defined in Eq. (3.35). The numerical results from the other two schemes Int1 and Int2 are not displayed since they would be indistinguishable from those from Scheme FD shown here.

according to the theoretical expressions in Eqs. (3.37) and (3.38). The linear strain rate and stress components  $\dot{\epsilon}_{\theta\theta}$  and  $\sigma_{\theta\theta}$  are also displayed since the numerical values for them are not exact zeros as predicted by theory. Due to the axisymmetry about the azimuthal angle  $\phi$ , both the theoretical and numerical values for the linear components  $\dot{\epsilon}_{\phi\phi}$  and  $\sigma_{\phi\phi}$  are zeros and thus they are not shown in Figure 3.4. For both the twisting surface and swirling flow approaches and at both  $t/T_0 = 1/4$  and  $t/T_0 = 3/4$  instants, we find the scattering patterns and deviation magnitudes are similar in the strain rate (left panels) and viscous stress plots (right panels). This similarity suggests that inaccuracy in the calculated stress is mainly caused by the upstream errors in the strain rate, and the FD viscous stress scheme has no apparent adverse influence on the final stress accuracy. The agreement between the numerical results and the analytical solutions is better in the twisting surface approach. The

errors observed in strain rates in Figure 3.4(a) are purely due to the surface triangulation and FEM. On the other hand, for the swirling flow approach, additional steps are involved: the node position is obtained from the interpolated node velocity. Accordingly, extra errors are introduced by this IBM velocity interpolation and node position update, and therefore the agreement in the calculated strain rate becomes less accurate than that in the twisting surface approach.

The three viscous stress schemes generate almost identical results. For this reason, we do not plot the results from Schemes Int1 and Int2 in Figure 3.4. To show the closeness of their performances quantitatively, we introduce the following error parameters:

$$L_{\dot{\epsilon}} = \frac{\left[ \frac{1}{N_e} \sum (\dot{\epsilon}_n - \dot{\epsilon}_t)^2 \right]^{1/2}}{\dot{\epsilon}^*} , \quad L_{\sigma} = \frac{\left[ \frac{1}{N_e} \sum (\sigma_n - \sigma_t)^2 \right]^{1/2}}{\sigma^*} ; \quad (3.41)$$

where the summations run over all surface elements and  $N_e = 5120$  is the total number of triangular surface elements. The calculated error values for both the shear ( $\theta\phi$ ) and linear ( $\theta\theta$ ) components from the three schemes are summarized in Table 3.3. These values confirm our visual observations in Figure 3.4: The  $L_{\sigma}$  errors from the FD scheme are very close to  $L_{\dot{\epsilon}}$  values for all cases, and the error values for the swirling flow system are larger than those in the twisting surface system. The  $L_{\sigma}$  errors are almost identical among the three numerical schemes, due to the relatively small time interval  $\Delta t$  compared to the relaxation time  $\tau_s$ . It is interesting to notice that, for the swirling flow approach, the  $L_{\sigma}$  values from all the three schemes are slightly smaller than  $L_{\dot{\epsilon}}$ , meaning that the schemes take a less accurate strain rate and produce a more accurate viscous stress. This is similar to our observation of  $L_2 < L_0$  at low  $k'$  values in Figure 3.2(c). One hypothetical explanation

Table 3.3: Numerical errors for the calculated strain rates ( $L_{\dot{\epsilon}}$ ) and viscous stresses ( $L_{\sigma}$ ) from different numerical schemes. Only the digit terms are listed and the common exponential term  $10^{-4}$  has been omitted for clarity.

$t/T_0$	shear, $\theta\phi$ -components				linear, $\theta\theta$ -components			
	$L_{\dot{\epsilon}}$	$L_{\sigma}$ , FD	$L_{\sigma}$ , Int1	$L_{\sigma}$ , Int2	$L_{\dot{\epsilon}}$	$L_{\sigma}$ , FD	$L_{\sigma}$ , Int1	$L_{\sigma}$ , Int2
Twisting Surface Approach								
1/4	2.834806	2.887311	2.887312	2.887145	2.681534	2.722547	2.722548	2.722570
3/4	2.834816	2.889782	2.889783	2.889617	2.681686	2.741682	2.741683	2.741706
Swirling Flow Approach								
1/4	6.538770	6.273621	6.273618	6.273725	4.832064	4.562048	4.562045	4.562083
3/4	6.538093	6.228608	6.228605	6.228714	4.832441	4.626541	4.626539	4.626578

could be: while the strain rate is purely determined by the simultaneous node positions, the viscous stress depends on the viscous stress at the previous step and the current strain rate (see Eq. 3.30). The viscous stress schemes happen to offset the original discrepancy in strain rates slightly and to yield slightly more accurate viscous stresses. However, it is difficult to identify the exact mechanism, considering the complexity in this system, which involves the IBM velocity interpolation, FEM calculation of surface strain, and viscous stress schemes. Nevertheless, the graphic comparison in Figure 3.4 and the error values in Table 3.3 demonstrate that, compared to IBM and FEM, the viscous stress schemes should not be a significant contributor to the overall numerical errors in IBM simulations of biological membranes.

### 3.4.3 Capsule Deformation in Shear Flow

The above tests use highly simplified systems, and several necessary components of IBM simulations, such as the IBM force distribution and flow field computation, are not involved. Next, we test the realistic performances of the three viscous stress algorithms by simulating the dynamic deformation of a spherical capsule with a viscoelastic membrane in shear flows [9, 58, 87, 99]. Following our recent publication [99], we adopt the

Skalak strain function Eq. (3.4) for the membrane elasticity, and the spherical surface of the undeformed capsule is discretized into 5120 triangular elements. The capillary number  $Ca = \mu_o \dot{\gamma} a / E_s$  is 0.3 and the fluid viscosity contrast ratio is  $\lambda = \mu_i / \mu_o = 1$ . Here  $\mu_i$  and  $\mu_o$  are respectively the interior and ambient fluid viscosities,  $\dot{\gamma}$  is the imposed shear rate, and  $a$  is the capsule radius before deformation. The simulation box is cubic with size of  $L$ , and the initial capsule radius is  $a = L/2\pi$  [9, 99]. The capsule is set at the center of the simulation box at the beginning of the calculation, and the shear flow is imposed by moving the top and bottom boundaries at velocity  $U_0$ , however, in opposite horizontal directions. The shear rate induced from such a configuration is then  $\dot{\gamma} = 2U_0/L$ . Periodic boundaries are applied on the other sides of the simulation box. The flow field is solved by the lattice Boltzmann method (LBM) [102], and the flow-membrane interaction is incorporated via IBM [98]. In our LBM calculations, we set the fluid density  $\rho = 1 \delta m / \delta x^3$ , the fluid viscosity  $\mu_o = \mu_i = 1/6 \delta m / \delta x \delta t$ , the simulation domain size  $L = 120 \delta x$ , and the boundary velocity  $U_0 = 2 \times 10^{-4} \delta x / \delta t$ . The average edge length for the triangular membrane elements is  $1.442 \delta x$  and this resolution has been tested in our previous publications with good accuracy [81, 99]. More details on the numerical implementation of this immersed boundary-lattice Boltzmann method (IB-LBM) can be found in the literature [66, 81, 99]. The exact values for these simulation units  $\delta m$ ,  $\delta x$  and  $\delta t$  depend on the particular properties of the physical system being simulated. The time interval  $\Delta t$  for the membrane viscous stress calculation, in principle, is not necessary to be the same as the LBM simulation time step  $\delta t$ , and a calculation frequency  $N = \Delta t / \delta t$  ( $N \geq 1$ ) can be introduced [99].

We only consider the shear membrane viscosity  $\mu_s$  as in previous studies [9, 58, 99], since the membrane of biological capsules and cells typically has a large dilatation module and

the dilatation deformation is negligible [50]. Two representative values, 10 and 40, for the Boussinesq number  $Bq_s = \mu_s/\mu_o a$  are examined. The corresponding artificial elastic modulus  $k'_s$  is implemented via a non-dimensional stiffness parameter  $\kappa = Lk'_s/U_0\mu_s$  in our IBM simulations.

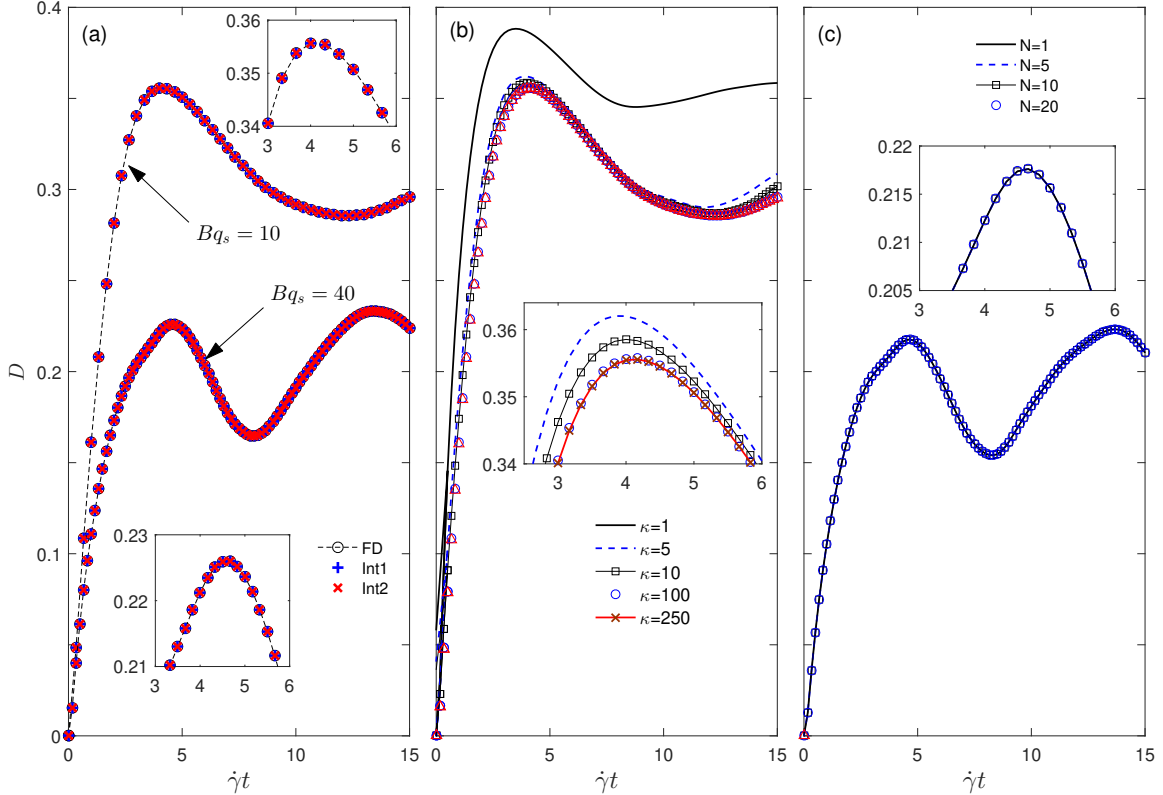


Figure 3.5: Profiles of deformation index  $D$  of a spherical capsule in shear flows: (a) Comparisons of the deformation index  $D$  from different numerical schemes for  $Bq_s = 10$  (with  $N = 25$  and  $\kappa = 100$ ) and  $Bq_s = 40$  (with  $N = 50$  and  $\kappa = 10$ ); (b) The  $\kappa$  effect on the simulated capsule deformation for  $Bq_s = 10$  with  $N = 25$ ; and (c) The  $N$  effect on the simulated capsule deformation for  $Bq_s = 40$  with  $\kappa = 70$ . The inset figures enlarge the  $D$  profiles at the profile peaks for a close view of the influences of  $N$  and  $\kappa$  values and the numerical schemes on simulation results.

Figure 3.5(a) displays the capsule deformation index  $D = (l - w)/(l + w)$  ( $l$  and  $w$  represent, respectively, the major and minor axes of the deformed capsule in the shear plane) for  $Bq_s = 10$  and 40 obtained from the three different numerical schemes. These schemes produce virtually identical results. This is consistent to our observations and analysis in

previous sections: Figure 3.2(c) shows that the difference among the three schemes would be notable only when the viscous stress calculation interval  $\Delta t$  is comparable to the relaxation time  $\tau_s = \mu_s/k'_s$ ; whereas in Figure 3.5(a) we have  $\tau_s/\Delta t = 240$  for  $Bq_s = 10$  and  $\tau_s/\Delta t = 1200$  for  $Bq_s = 40$ . The similar error values in Table 3.3 also suggest that the three schemes should yield similar simulation results. We have tested more cases and the three schemes always generate almost identical results. Based on this observation, we only present results from the FD scheme in the rest of this section, except otherwise mentioned.

The motivation for adding the artificial elastic element  $k'$  in series to the viscous dashpot in Figure 3.1(b) is to improve the numerical stability [9, 58, 99]. In general, a large value of  $k'$  is favorite for a good accuracy in the calculated viscous stress; on the other hand, a too large spring constant  $k'$  may cause the simulation to collapse. This issue has not been carefully tested in previous studies. Figure 3.5(b) shows the capsule deformation for  $Bq_s = 10$  using  $N = 25$  but different  $\kappa$  values. For  $\kappa = 1$ , it seems the artificial spring is too weak and the deformation is relatively large. As  $\kappa$  increases (i.e., the artificial spring becomes stiffer), the capsule deformation decreases and the profiles gradually approach to a steady curve. The difference between the deformation profiles from  $\kappa = 100$  and 250 is negligible (see Figure 3.5(b) inset), indicating that the results from such high  $\kappa$  values are reliable. Further increasing the  $\kappa$  value (for example, to  $\kappa = 300$ ) causes the computation to break down soon after the shear boundary velocity imposed. We then examine the effect of the viscous stress calculation frequency  $N$  using the  $Bq_s = 40$  system with  $\kappa = 70$ , and the results are displayed in Figure 3.5(c). It is evident that in the range of  $1 \sim 20$ ,  $N$  has no influence on the calculated results; however, the calculation breaks down when  $N = 25$  is

tried.

To have a better understanding of the effects of  $\kappa$  and  $N$  on the simulation accuracy and stability, we conduct extensive calculations for the  $Bq_s = 10$  and  $40$  systems with various  $\kappa$ - $N$  combinations, and take  $D_1$ , the first peak value of deformation index  $D$ , as a measure of the simulation accuracy. Again the results from the three different schemes appear identical and thus here we only present those from the FD method. Figure 3.6 collects results for all these calculations, with black crosses ( $\times$ ) for the unstable calculations and boxes for the stable calculations. In addition, the peak deformation  $D_1$  for the stable simulations are indicated by the filling colors of those boxes. The critical  $\kappa$  value for the stable-unstable transition decreases approximately linearly with the viscous stress calculation frequency  $N$  in the  $\log_{10} \kappa \sim \log_{10} N$  graphs (see the dashed lines). Comparing Figure 3.6(a) for  $Bq_s = 10$  and Figure 3.6(b) for  $Bq_s = 40$ , one can see that the critical  $\kappa$  values are also smaller for more viscous membranes, meaning simulations are less stable for higher membrane viscosities.

For the stable simulations with a same  $N$  value (along a vertical line in Figure 3.6), the peak deformation  $D_1$  decreases gradually with  $\kappa$  and a stable value is gradually approached (0.355 for  $Bq_s = 10$  and 0.215 for  $Bq_s = 40$ ). On the other hand, for a fixed  $\kappa$  (along a horizontal line in Figure 3.6), the simulated peak deformation  $D_1$  appears insensitive to the change in the viscous stress calculation frequency  $N$ , as indicated by the same filling color of the boxes. The dependence of  $D_1$  on  $\kappa$  and  $N$  is more quantitatively shown in Figure 3.7, where the peak deformation  $D_1$  is plotted versus the non-dimensional stiffness  $\kappa$  for all stable simulations. Apparently, the two sets of data points, one for  $Bq_s = 10$  and one for  $Bq_s = 40$ , follow two smooth curves (dashed curves), which can be nicely described by

the following power function

$$D_1 = a\kappa^{-b} + c, \quad (3.42)$$

where the fitting parameters are  $(a, b, c) = (0.0329, 0.997, 0.355)$  for  $Bq_s = 10$  and  $(0.0588, 0.728, 0.215)$  for  $Bq_s = 40$ . The difference in  $D_1$  from simulations with a same  $\kappa$  but different  $N$  is negligible.

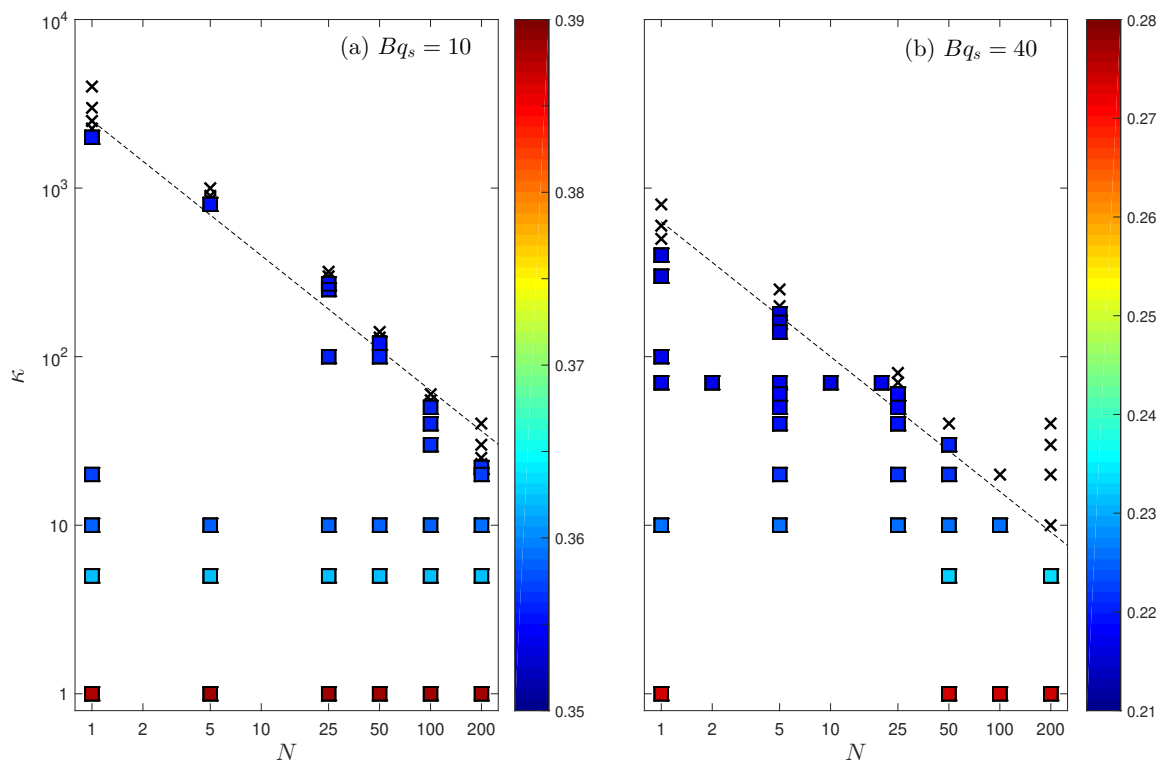


Figure 3.6: Phase diagrams for the simulation stability (crosses: unstable; boxes: stable) and accuracy (the filling color of each box represents the calculated  $D_1$  value according to the color bar on the right) of capsule deformation in shear flow with (a)  $Bq_s = 10$  and (b)  $Bq_s = 40$ . The dashed lines separate the stable and unstable regions approximately.

Another important concern for scientific simulations is the computational efficiency. With the relatively simple expressions in Eq. (3.30) and Table 3.2, one can expect that the extra computation cost for the membrane viscous stress would not be significant when compared to other parts of IBM simulations. For more quantitative information, we record the computation time of one single CPU for repeating  $10^5$  executions of one specific computational

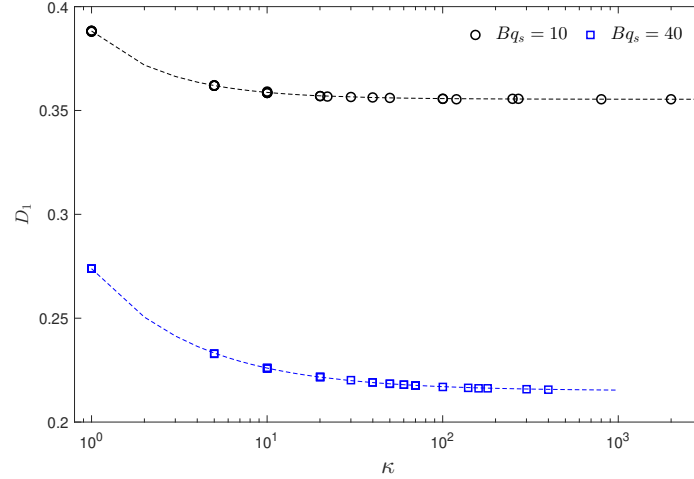


Figure 3.7: Dependence of the peak deformation  $D_1$  on the non-dimensional stiffness  $\kappa$  for all stable simulations in Figure 3.6. The dashed curves are obtained by fitting the  $D_1 \sim \kappa$  data points with the power function Eq. (3.42).

component in our capsule simulation. The test results are listed in Table 3.4. Clearly, the three schemes for the membrane viscous stress calculation have similar computational efficiency, and moreover, they take a nearly negligible fraction of the total computation time, the majority of which is spent on the LBM calculation solving the flow field and the IBM treatment for the flow-membrane interaction. The numbers in Table 3.4 are collected from our homemade program, and they may vary with the computer hardware, programming and coding, IBM algorithms, and numerical methods for solving the flow field. However, the difference by orders of magnitude evidently demonstrates that the membrane viscous stress calculation should not be a concern for computation time in IBM simulations.

Table 3.4: The one-CPU computation time (in seconds) for  $10^5$  executions of individual computational components in our capsule IBM simulation.

FD	Int1	Int2	IBM	LBM
7.220	5.793	5.809	1510.2	78201.8

Based on the capsule simulation results and analysis of the computational accuracy, stability and efficiency, we find that the viscous stress calculation frequency  $N$  has no impact on

the simulation accuracy; however, a large  $N$  value can reduce the simulation stability and thus prevent the use of a large  $\kappa$  value for a better accuracy. Li and Zhang [99] proposed that a large  $N$  could be helpful for improving the simulation accuracy and stability based on the interpolated velocity of a particle moving along a streamline in a two-dimensional flow. Clearly this is not the case for the capsule deformation simulations in this study. The disagreement might be due to the over simplification in Ref. [99] for the complex IBM simulation of a viscoelastic capsule. Another potential benefit by using a large  $N$  is that the membrane viscous stress can be calculated less often (i.e., once every  $N$  simulation time steps). However, the reduction in computation time is tiny considering the negligible execution time for the membrane viscous stress calculation compared to other parts of IBM computation. Therefore, we recommend  $N = 1$  (i.e.,  $\Delta t = \delta t$ ) for future IBM simulations.

### 3.5 Summary

We have developed two numerical schemes based on the convolution integral expression of the Maxwell viscoelastic element for membrane viscous stress calculation in IBM simulations. These two integral schemes as well as the recent finite-difference approach [99] have been carefully tested for their performances in accuracy, stability and efficiency. First, the stress of a 1D viscoelastic Maxwell element was calculated using individual schemes and their results were compared to analytical solutions. Our analysis showed that, to have a good accuracy from these schemes, one should properly select the relaxation time: it should be sufficiently smaller than the characteristic time  $T_0$  of the strain variation and, in the meantime, it should be sufficiently larger than the viscous stress calculation interval

$\Delta t$ . With the large difference between  $T_0$  and  $\Delta t$  in typical IBM simulations for biological capsules, this requirement is easily to be met. We then compared the relative error magnitudes from the viscous stress schemes, the membrane discretization, and the IBM velocity interpolation, and found that the errors due to viscous stress schemes are negligible. Furthermore, the dynamic deformation of a spherical capsule in shear flow has been simulated using these different numerical schemes and various combinations of the artificial spring stiffness  $\kappa$  and the viscous stress calculation frequency  $N$ . The three schemes (FD, Int1 and Int2) show virtually identical performances in simulation accuracy and stability, and the computation time of such schemes is insignificant compared to other calculations in IBM simulations. The simulation accuracy improves with the stiffness  $\kappa$ , and it appears independent to the change in the viscous stress calculation frequency  $N$ . On the other hand, simulations become unstable when large  $\kappa$  and  $N$  values are used, and the critical  $\kappa$  value for the stable-unstable transition decreases with the frequency  $N$  and the membrane viscosity. Based on these results, we recommend to set  $N = 1$  (i.e., calculate the viscous stress at each simulation time step) in future IBM simulations. In summary, the three methods for membrane viscous stress calculation have nearly identical numerical performances and they can all be adopted for future IBM simulations of viscoelastic membranes. The analysis and discussions in this paper are also useful for selecting proper simulation parameters in such IBM simulations. Considering that most previous IBM simulations of biological cells and vesicles and even liquid droplets have not considered the membrane/interfacial viscous effect, it would be interesting to revisit such systems to pursue a better understanding of the roles that the membrane/interfacial viscosity plays in various biological and industrial situations.

## **Acknowledgment**

The authors sincerely thank one anonymous reviewer of our previous publication [99] for inspiring comments. This work was supported by the Natural Science and Engineering Research Council of Canada (NSERC). The calculations have been enabled by the use of computing resources provided by WestGrid ([westgrid.ca](http://westgrid.ca)), SHARCNet ([sharcnet.ca](http://sharcnet.ca)), and Compute/Calcul Canada ([computecanada.org](http://computecanada.org)). P.L. acknowledges the financial support from the Ontario Trillium Scholarship at Laurentian University.

## **Chapter 4**

### **Similar but Distinct Roles of Membrane and Interior Fluid**

### **Viscosities in Capsule Dynamics in Shear Flows \***

Ping Li and Junfeng Zhang

Bharti School of Engineering, Laurentian University

935 Ramsey Lake Road, Sudbury, ON P3E 2C6, Canada

---

\*This Chapter has been published in Cardiovascular Engineering and Technology (in press), 2021.

## Abstract

*Purpose:* The dynamics of biological capsules and red blood cells in shear flows have been studied extensively with experimental, analytical, and numerical methods. In particular, the effects of various parameters, including the shear rate or shear stress, membrane elasticity, capsule shape, and interior fluid viscosity, have been investigated carefully. The role of the membrane viscosity for capsule deformation dynamics has not been examined adequately. In previous studies, the so-called energy dissipation ratio has been used to account for the membrane viscosity effect by increasing the interior viscosity; however, the applicability and accuracy of this treatment have not been evaluated carefully.

*Methods:* In this study, using the recently developed finite-difference scheme for immersed boundary simulations of viscoelastic membranes, we conduct comprehensive numerical simulations of the deformation processes of an originally spherical capsule in shear flows with various combinations of membrane and interior fluid viscosities.

*Results:* Our results show that the membrane and interior fluid viscosity have similar however different effects on the capsule deformation dynamics. While the capsule deformation decreases with both membrane and interior fluid viscosities, a typical decrease-then-increase variation is observed for the inclination angle as the membrane viscosity increases, instead of the monotonic decrease in the inclination angle with the interior fluid viscosity increase. Also, although both large membrane and interior fluid viscosity values can introduce oscillations in the capsule deformation and inclination, larger amplitudes and slow decay processes are noticed at larger membrane viscosities. The variations of other dynamic parameters of the capsule, including the circumference, average membrane velocity,

and rotation frequency, are also analyzed, and an intuitive mechanism is proposed to relate the membrane velocity and rotation frequency to the capsule deformation and inclination angle. The simple mechanism is then applied to explain the spoon-like variation patterns for membrane velocity and rotation frequency observed in our results. Furthermore, we examine the validity of the energy dissipation ratio approach based on the mathematical functional dependence.

*Conclusions:* Our results and analysis show that the dissipation ratio is a system and process dependent variable and it cannot be treated as a constant even for the same capsule. This research is valuable for a better understanding of the complex capsule dynamics in flows and also suggests that the membrane viscosity needs to be considered explicitly for accurate and reliable results in future studies.

## **Keywords**

Membrane Viscosity, Interior Fluid Viscosity, Capsule Deformation, Energy Dissipation Ratio, Red Blood Cells, Immersed Boundary Method

## 4.1 Introduction

Liquid drops enclosed by thin flexible membranes, usually called capsules (with solid-like polymerized membranes) or vesicles (with fluid-like lipid bilayer membranes), are often encountered in biological and artificial systems and process [103–107]. For example, the erythrocytes or red blood cells (RBCs) can be considered as liquid capsules and they play critical roles in the transport of oxygen and other gases in the bodies of human and other animals. For these reasons, the dynamics of capsules in a flow has received considerable attention in experimental, theoretical and computational studies [30, 47, 81, 103, 108–113].

To simulate the dynamics of a deformable capsule in flow field, several challenges exist due to the continuous deformation of capsule membrane and the simultaneously flow-structure interaction [50]. Tremendous efforts have been devoted to study the membrane dynamics with the shear, bending, and dilation stresses considered [66, 81, 114]. In addition, biological capsule membranes also exhibit viscous resistance to strain rate due to dynamic membrane deformation [57, 71, 72, 115, 116]. While the effect of interior fluid viscosity on capsule deformation in shear flows and migration in channel flows have been investigated extensively [43, 81, 117], the influence from the membrane viscosity on capsule dynamics has not been addressed adequately. Evans and Hochmuth [118] and Chien et al. [119] proposed that the energy dissipation rate in the membrane may exceed that in the interior hemoglobin solution for RBCs. Fischer [120] found that although both dissipation rates showed a strong increase with flow shear rate, their ratio was essentially constant and of the order of 1. Accordingly, Keller and Skalak [112] introduced the energy dissipation ratio

$d$  to take account of the membrane viscous effect by increasing the interior fluid viscosity from the real value  $\mu_c$  to  $(1 + d)\mu_c$ . Recently, Vlahovska [104] conducted asymptotic analysis for small deformations of a spherical capsule in shear flows, and an explicit relation for the coefficient  $d$  was obtained. Clearly these theoretical studies were limited to the tank-treading situation of originally spherical capsules with small deformations in shear flows. In practice, however, this concept has been applied in later studies of capsules and RBCs with larger deformations and unsteady dynamics. Fischer [120] and Tran-son-Tay et al. [57] suggested the energy dissipation ratio  $d$  between 2 and 4 based on their experimental measurements. Skotheim and Secomb [33] chose the apparent internal viscosity as 4 times of the actual cytoplasm viscosity (corresponding to a membrane dissipation ratio  $d = 3$ ) in their theoretical analysis of the oscillatory dynamics and the tank-treading-to-tumbling transition for RBCs and other nonspherical capsules. Recently, Yazdani and Bagchi [9] numerically calculated the energy dissipation rates in the membrane and in the interior fluid for capsules with different membrane viscosities, and they also suggested that it might be possible to model a viscoelastic capsule as a purely elastic capsule with a higher internal viscosity. The convenience for this equivalence (i.e., the membrane viscous effect can be represented by an elevated interior fluid viscosity), if true, is apparent: one can simply increase the interior fluid viscosity to compensate for the membrane viscous effect, and the membrane can be treated as a purely elastic material. However, because of the validity and accuracy for this treatment has not been examined carefully, the results from such a simplification could be open to question.

Among the several numerical methods commonly used to simulate the motion and deformation of capsules in flow fields, the immersed boundary method (IBM) has several

attractive features [9, 47, 65–69]. It combines the Lagrangian description for the moving/deforming objects and the Eulerian description for the surrounding flow in a novel approach and thus avoids the complicated and time-consuming mesh regeneration. Moreover, in IBM, we solve the induced nodal forces from the deformation of the discretized structure, instead of solving the structure deformation from the applied nodal forces as in typical finite element calculations. This is computationally favorable since the nodal forces can be efficiently calculated as the product of the nodal displacements and the stiffness matrix [121]. Also, IBM can be easily integrated with typical computational methods for fluid flows, such as the finite volume method, the finite element method, the finite-difference method, and the recent lattice Boltzmann method (LBM) [9, 47, 65–69]. Unfortunately, direct implementation of membrane viscosity in IBM calculations suffers severe numerical instability, which may cause an IBM simulation to break down before generating any useful results [9, 99]. To improve the numerical stability, an artificial elastic element has been introduced in series to the membrane viscous component [9, 58, 99]. The spring stiffness needs to be large enough so its effect on the membrane dynamics can be neglected, as shown by the non-dimensional analysis in Ref. [99]. Recently, Li and Zhang [99] proposed a finite-difference approach for implementing membrane viscosity in IBM simulation. This method had been carefully validated and its numerical performance, such as accuracy, stability, and efficiency have been examined [122], and recently it has been adopted to study the RBC relaxation process after removing external mechanical loads [116].

In this study, we use the finite-difference method for IBM simulations of viscoelastic membranes in Ref. [99] to examine the individual and combined effects of the membrane and interior fluid viscosities on capsule dynamics in shear flows. Our results show that the

membrane and interior fluid viscosities have similar but different effects on the capsule behaviors. A simple intuitive mechanism is also proposed for the relationships among the capsule membrane velocity, rotation frequency, deformation index, and inclination angle. Based on this mechanism, qualitative explanations are provided for the spoon-like variations of membrane velocity and rotation frequency with membrane and interior fluid viscosities. At last, the validity of the energy dissipation ratio treatment for modelling viscoelastic capsules as pure elastic ones is analyzed using mathematical functional relationships and numerical results of deformation and inclination angle. Based on our results and analysis for systems considered in this study, it appears inappropriate to replace the membrane viscosity with an elevated interior fluid viscosity. The results and analysis in this paper could be valuable for a better understanding of the complex capsule dynamics in flows, and also suggest that the membrane viscosity needs to be considered explicitly for accurate and reliable results in the future.

## **4.2 Model and Methods**

### **4.2.1 Membrane viscoelasticity**

Considering the tiny membrane thickness for typical biological capsules (e.g.,  $\sim 10$  nm for RBCs) compared to the capsule size (e.g.,  $\sim 8$   $\mu\text{m}$  in diameter for RBCs), the capsule membrane can be treated as a two-dimensional (2D) sheet with no mass and thickness. The elastic stress induced by the membrane in-plane deformation usually is expressed in terms

of the strain energy function, such as the Skalak function for RBCs [12]:

$$W_s = \frac{E_s}{8}(I_1^2 + 2I_1 - 2I_2) + \frac{E_a}{8}I_2^2 \quad , \quad (4.1)$$

where  $W_s$  is the strain energy per membrane area, and  $E_s$  and  $E_a$  are, respectively, the shear and dilation moduli. The strain invariants  $I_1$  and  $I_2$  are related to the two principle stretch ratios  $\varepsilon_1$  and  $\varepsilon_2$  for a 2D membrane by

$$I_1 = \varepsilon_1^2 + \varepsilon_2^2 - 2 \quad ; \quad I_2 = \varepsilon_1^2 \varepsilon_2^2 - 1 \quad . \quad (4.2)$$

The elastic stress tensor  $\tau^e$  can then be obtained from this energy function as [12, 85]

$$\tau^e = \tau_1^e \mathbf{e}_1 \otimes \mathbf{e}_1 + \tau_2^e \mathbf{e}_2 \otimes \mathbf{e}_2 \quad , \quad (4.3)$$

where

$$\tau_1^e = \frac{1}{\varepsilon_2} \frac{\partial W_s}{\partial \varepsilon_1} \quad ; \quad \tau_2^e = \frac{1}{\varepsilon_1} \frac{\partial W_s}{\partial \varepsilon_2} \quad ; \quad (4.4)$$

are the two principal stresses; and  $\mathbf{e}_1$  and  $\mathbf{e}_2$  are their corresponding directions. The principle directions  $\mathbf{e}_1$  and  $\mathbf{e}_2$  can be obtained as the unit eigenvectors of the left Cauchy-Green deformation tensor  $\mathbf{G} = \mathbf{F}\mathbf{F}^T$  with  $\mathbf{F}$  as the deformation gradient matrix [9, 66]. With the membrane being discretized into triangular elements, the matrix  $\mathbf{F}$  can be readily calculated by comparing the deformed and original configurations of each element [86]. The strain tensor  $\mathbf{E}$  is related to matrices  $\mathbf{G}$  or  $\mathbf{F}$  as [103]:

$$\mathbf{E} = \frac{1}{2}(\mathbf{G}^T - \mathbf{1}) = \frac{1}{2}(\mathbf{F}^T \mathbf{F} - \mathbf{1}) \quad . \quad (4.5)$$

The viscous stress  $\boldsymbol{\tau}^v$  in membranes or fluid interfaces is typically split into two parts: the shear viscous stress  $\boldsymbol{\tau}_s^v$  induced by the shear (deviatoric) part of the strain rate tensor  $\mathbf{D}$ , and the dilatational viscous stress  $\boldsymbol{\tau}_d^v$  from the dilatational (hydrostatic) part of  $\mathbf{D}$  [2, 9, 82, 87, 88, 103]:

$$\boldsymbol{\tau}^v = \boldsymbol{\tau}_s^v + \boldsymbol{\tau}_d^v = \mu_s [2\mathbf{D} - \text{tr}(\mathbf{D})\mathbf{I}] + \mu_d \text{tr}(\mathbf{D})\mathbf{I} \quad , \quad (4.6)$$

where  $\mu_s$  and  $\mu_d$  are the shear and dilatational membrane viscosities, respectively. The matrix  $\mathbf{D}$  is the strain rate tensor of the membrane and  $\mathbf{I}$  is the  $2 \times 2$  unit matrix. A convenient way to numerically obtain the strain rate tensor  $\mathbf{D}$  is to apply a backward finite-difference approximation to the strain tensor  $\mathbf{E}$ ; whereas another approach is via the membrane velocity gradient [2, 82, 88, 103]

$$\mathbf{D} = \frac{1}{2} [\nabla_m \mathbf{u}_m + (\nabla_m \mathbf{u}_m)^T] \quad , \quad (4.7)$$

where  $\nabla_m$  is the gradient operator and  $\mathbf{u}_m$  is the membrane velocity, both in the local membrane plane.

As to be seen below, IBM requires the nodal force at each Lagrangian membrane node. This can be accomplished with the help of the shape functions of the triangular elements according to the finite element theory [9]. The elastic part of the nodal force can also be calculated directly from the energy function according to the virtual work principle [66, 81]. Other aspects of membrane mechanics, including the bending modulus, area conservation and intercellular aggregation, can be considered as well [9, 66, 81].

## 4.2.2 Immersed Boundary Method (IBM)

Following the previous studies [47, 66, 99], we use the IBM [46] to model the dynamic interaction between flow field and membrane motion and deformation. To solve the flow field (both inside and outside of the capsule), we apply the lattice Boltzmann method over a uniform Eulerian grid. In the meanwhile, the membrane surface is represented by a triangular Lagrangian grid. IBM couples the fluid and structure meshes via two steps: the force distribution and the velocity interpolation. When a membrane is deformed, the membrane force will be developed according to the material constitutive relationship, as discussed above in Sect.4.2.1. The membrane force  $\mathbf{F}_m$  calculated at a membrane node  $\mathbf{x}_m$  is then transferred to local fluid nodes  $\mathbf{x}_f$  as body forces  $\mathbf{F}_f$ :

$$\mathbf{F}_f(\mathbf{x}_f) = \sum_{\mathbf{x}_m} D(\mathbf{x}_f - \mathbf{x}_m) \mathbf{F}_m(\mathbf{x}_m) \quad (4.8)$$

using a discrete delta function  $D(\mathbf{x})$ , which is chosen to approximate the properties of the Dirac delta function [46]:

$$D(\mathbf{x}) = \frac{1}{(4\delta x)^3} \left(1 + \cos \frac{\pi x}{2\delta x}\right) \left(1 + \cos \frac{\pi y}{2\delta x}\right) \left(1 + \cos \frac{\pi z}{2\delta x}\right), \quad (4.9)$$

$$|x| \leq 2\delta x, |y| \leq 2\delta x, \text{ and } |z| \leq 2\delta x$$

$$D(\mathbf{x}) = 0, \text{ otherwise.}$$

Here  $x, y, z$  are the three elements of location vector  $\mathbf{x}$ , and  $\delta x$  is the Euler grid resolution.

On the other hand, as the fluid flows, the membrane moves with the ambient flow and deforms accordingly. To enforce the no-slip requirement between the flow and the mem-

brane surface, the membrane velocity  $\mathbf{u}_m(\mathbf{x}_m)$  is obtained from the local flow field  $\mathbf{u}$  via interpolation, which also uses the kernel function  $D(\mathbf{x})$ :

$$\mathbf{u}_m(\mathbf{x}_m) = (\Delta x)^3 \sum_{\mathbf{x}_f} D(\mathbf{x}_f - \mathbf{x}_m) \mathbf{u}(\mathbf{x}_f) . \quad (4.10)$$

Here the summation runs over all fluid nodes with  $D(\mathbf{x}) > 0$ . The membrane location and configuration can then be updated, for example, using the Euler approximation according to the membrane velocity  $\mathbf{u}_m$ .

$$\mathbf{x}_m(t + \Delta t) = \mathbf{x}_m(t) + \mathbf{u}_m(t) \Delta t . \quad (4.11)$$

### 4.2.3 Finite-Difference Method for Membrane Viscosity in IBM Simulations

For simplicity and clarity, we employ the Kelvin-Voigt model (Figure 4.1(a)) as an idealization of the membrane viscoelastic behavior described in Sect. 4.2.1. The elastic part of the membrane mechanics is represented by the spring element  $k$  and the viscous part is displayed as the dashpot element  $\mu$ . These two elements are connected in parallel and thus they share the same membrane deformation and strain. Since in IBM the flow-membrane coupling process is a strain-imposed problem (i.e., we are calculating the membrane stress from the membrane deformation), the significant errors in strain rate discussed above produce abrupt variations in the viscous stress from the dashpot. To overcome this difficulty in numerical stability, we follow previous practices [9, 58] and add an artificial spring element  $k'$  in series to the dashpot  $\mu$  (Figure 4.1(b)). Now the dashpot  $\mu$  and the new spring  $k'$  form a Maxwell viscoelastic element; and the original Kelvin–Voigt model is transferred into the so-called standard-linear-solid (SLS) model in the viscoelasticity theory [83]. As shown in

Ref. [99], when the stiffness of  $k'$  is sufficiently large, its effect on the system performance becomes negligible. However, with the addition of this spring  $k'$ , the stress induced in the Maxwell element cannot be expressed explicitly for a given strain  $\varepsilon(t)$ . Previous attempts used the integral approach [9, 58]; however, several physical and mathematical concerns exist in these implementations [99]. Here we adopt the finite-difference method recently developed by Li and Zhang [99] to calculate the viscous stress in the Maxwell element.

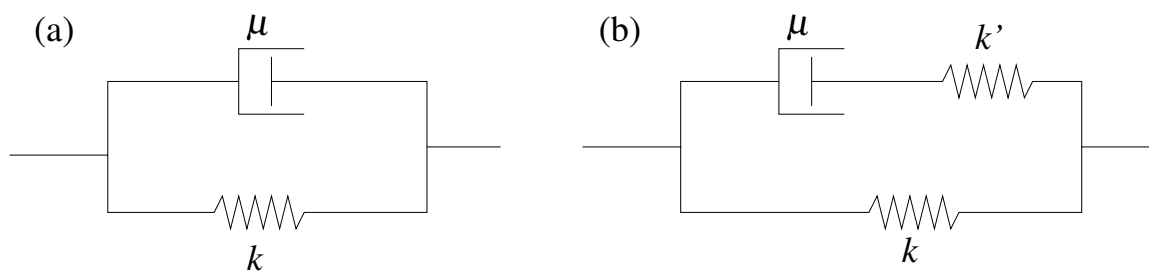


Figure 4.1: Schematic drawings showing (a) the Kelvin–Voigt model for viscoelastic membrane mechanics (spring  $k$  for membrane elasticity and dashpot  $\mu$  for membrane viscosity) and (b) the standard linear solid (SLS) model with an artificial spring  $k'$  added to improve the numerical stability in IBM simulations. In (b) the dashpot  $\mu$  and the spring  $k'$  together form a Maxwell viscoelastic model.

Since the dashpot  $\mu$  and the spring  $k'$  are connected in series, the internal stress in these two components is the same as that in the overall Maxwell element

$$\sigma_M = \sigma_\mu = \sigma_{k'} \quad ; \quad (4.12)$$

and the strain of the Maxwell element is the sum of those for the dashpot  $\mu$  and artificial spring  $k'$

$$\varepsilon_M = \varepsilon_\mu + \varepsilon_{k'} \quad ; \quad (4.13)$$

where all these strain terms are defined according to the same undeformed length of the Maxwell element. Here we use  $\sigma$  for the stresses and  $\varepsilon$  for the strains, and subscripts

are used to indicate the corresponding components for these properties:  $M$  for the Maxwell element,  $\mu$  for the dashpot  $\mu$ , and  $k'$  for the spring  $k'$ . The stresses and strains in the dashpot  $\mu$  and spring  $k'$  are related via the coefficients for the viscous dashpot and the linear spring as

$$\sigma_{\mu} = \mu \dot{\varepsilon}_{\mu} \ ; \ \sigma_{k'} = k' \varepsilon_{k'} \ . \quad (4.14)$$

In this equation,  $\mu$  and  $k'$  have also been used to denote, respectively, the viscosity of the dashpot  $\mu$  and the Hookean coefficient of the spring  $k'$ . Applying the time rate to Eq. (4.13) and utilizing relations in Eqs. (4.12) and (4.14) yield

$$\dot{\varepsilon}_M = \frac{\sigma_M}{\mu} + \frac{\dot{\sigma}_M}{k'} \ . \quad (4.15)$$

This can be considered as the dynamic constitutive relation for the Maxwell element. For a time interval from  $t - \Delta t$  to  $t$ , we can apply the central finite-difference approximation for the time rate terms

$$\dot{\varepsilon}_M(t - \Delta t/2) \approx \frac{\varepsilon_M(t) - \varepsilon_M(t - \Delta t)}{\Delta t} \ ; \ \dot{\sigma}_M(t - \Delta t/2) \approx \frac{\sigma_M(t) - \sigma_M(t - \Delta t)}{\Delta t} \ . \quad (4.16)$$

In the meantime we write the stress at  $t - \Delta t/2$  as the average of those at  $t - \Delta t$  and  $t$ :

$$\sigma_M(t - \Delta t/2) \approx \frac{\sigma_M(t - \Delta t) + \sigma_M(t)}{2} \ . \quad (4.17)$$

Using these approximations, Eq. (4.15) now is written as

$$\frac{\varepsilon_M(t) - \varepsilon_M(t - \Delta t)}{\Delta t} \approx \frac{\sigma_M(t - \Delta t) + \sigma_M(t)}{2\mu} + \frac{\sigma_M(t) - \sigma_M(t - \Delta t)}{k' \Delta t} \ , \quad (4.18)$$

Table 4.1: Simulation parameters used in this work. All values are non-dimensional based on LBM simulation units: length in the lattice grid  $\delta x$ , time in the simulation time step  $\Delta t$ , and mass in the reference mass  $\delta m$ . The physical values of these simulation units can only be determined when a specific system is given.

parameters	values
domain size $H$	120
capsule radius $a$	19.10
fluid density $\rho$	1
boundary velocity $U_0$	$(1 \sim 4) \times 10^{-3}$
exterior viscosity $\mu_0$	$0.0333 \sim 0.1667$

from which the stress term  $\sigma_M(t)$  can then be solved as

$$\sigma_M(t) \approx \frac{(2\mu - k'\Delta t)\sigma_M(t - \Delta t) + 2\mu k'[\varepsilon_M(t) - \varepsilon_M(t - \Delta t)]}{2\mu + k'\Delta t} . \quad (4.19)$$

With the initial condition specified [typically the system dynamics starts from a stress-free state  $\varepsilon_M(0) = 0$  and  $\tau_M(0) = 0$ ], and a time interval  $\Delta t$  being selected properly, the above equation can be employed to calculate the stress in the Maxwell element  $\sigma_M(t)$  from the imposed strain function  $\varepsilon_M(t)$ .

## 4.3 Results and Discussion

### 4.3.1 Simulation Setup and Parameters

In this research, we consider the dynamic response of a spherical capsule of radius  $a$  in shear flow, with the flow-membrane interaction incorporated via IBM [81]. The capsule membrane is discretized into 5120 triangular elements from an icosahedron using recursive subdivision [43, 66]. The side length  $H$  of the cubic computational domain is set as  $2\pi a$ .

To generate a shear flow, the top and bottom domain boundaries are treated as solid walls moving with the same velocity magnitude  $U_0$  but in opposite directions, generating a shear rate  $\dot{\gamma} = 2U_0/H$ . Periodic boundary conditions are applied on the other four sides of the simulation domain [102]. The exterior suspending fluid viscosity is  $\mu_0$ , and the interior fluid viscosity is  $\mu_c$ . The fluid viscosity contrast is then defined as the fluid viscosity ratio  $\lambda = \mu_c/\mu_0$ . To solve the flow field, we use the two-relaxation-time (TRT) lattice Boltzmann method (LBM) for its good performance in reducing the artificial slip between the membrane surface and fluid [123, 124]. The different fluid viscosities across the capsule membrane are accomplished by assigning different relaxation times in LBM calculations on the fluid nodes [124]. Table 4.1 lists the simulation parameters used in this research. For the capsule membrane, we take  $E_s = E_a$  in the Skalak energy function Eq. (4.1). The capillary number  $Ca = \mu_0\dot{\gamma}a/E_s$  is kept as 0.3 for the simplicity of this study. In this work, we mainly focus on the shear membrane viscosity as in previous studies [9, 58, 99], since the membrane of biological capsules and cells typically have a large dilatation modulus and the dilatation deformation is negligible [50]. The effect from the dilatational membrane viscosity will be also be briefly examined in Sect. 4.3.5. The shear membrane viscosity is represented by the shear Boussinesq number  $Bq_s = \mu_s/\mu_0a$ , where  $\mu_s$  is the membrane shear viscosity. For RBCs, the membrane viscosity values reported in the literature range in  $(0.53 \sim 10) \times 10^{-7}$  mPas [116]. Take the plasma viscosity as  $\mu_0 = 1.2$  cP and the RBC radius as  $a = 4 \mu\text{m}$ , the corresponding Boussinesq number for RBCs is in the range of 11~208. As described in Sect. 4.2.1, an artificial elastic element is added in series to the viscous component in the membrane mechanics to improve the numerical stability. The corresponding artificial elastic modulus  $k'$  is implemented via a non-dimensional stiffness parameter  $\kappa = Hk'/U_0\mu_s$ , and we take  $\kappa = 1000$  in the following simulations to minimize

the artificial effect from the spring  $k'$  [122]. The methods and programs used in this work have been carefully validated in previous studies [81, 99, 122].

Typically, the capsule deformation in shear flow is described using two parameters: the Taylor deformation index  $D$  and the inclination angle  $\theta$ . Both are evaluated in the shear plane. The deformation index is defined as  $D = (L - W)/(L + W)$ , where  $L$  and  $W$  represent the major and minor axes of the deformed ellipsoid-like capsule in the shear plane. The inclination angle  $\theta$  is the one between the flow direction and the major axis. These parameters are calculated from the principal directions of the inertia tensor of the deformed capsule [43]. In addition, we also calculate the capsule rotation frequency, which can be readily obtained from the rotation period. There are two typical methods to find the capsule rotation period  $T$ : (a) from the trajectory of a membrane marker point or (b) by integrating the travel time of a membrane marker [43, 44, 125]. The results from these two methods are very close, as reported in Ref. [125] and confirmed in this current work. Here we prefer to the latter approach since we can relate the rotation frequency  $\nu$  to the circumference  $C$  and average velocity  $V_m$  of the membrane in the shear plane as  $\nu = 2\pi/T = 2\pi V_m/C$ , and this is helpful for analyzing the frequency relation to the capsule deformation and rotation. In this work, these quantities are normalized as follows:  $T^* = \dot{\gamma}T$ ,  $C^* = C/2\pi a$ ,  $V_m^* = V_m/\dot{\gamma}a$ , and  $\nu^* = V_m^*/C^* = 2\pi/T^*$ .

#### 4.3.2 Individual Effects of $\lambda$ and $Bq_s$ on Capsule Deformation

We first perform two series of simulations for the capsule deformation processes in shear flows: (a) pure elastic membrane (i.e.,  $Bq_s = 0$ ) with varying fluid viscosity contrast  $\lambda=0.2$ ,

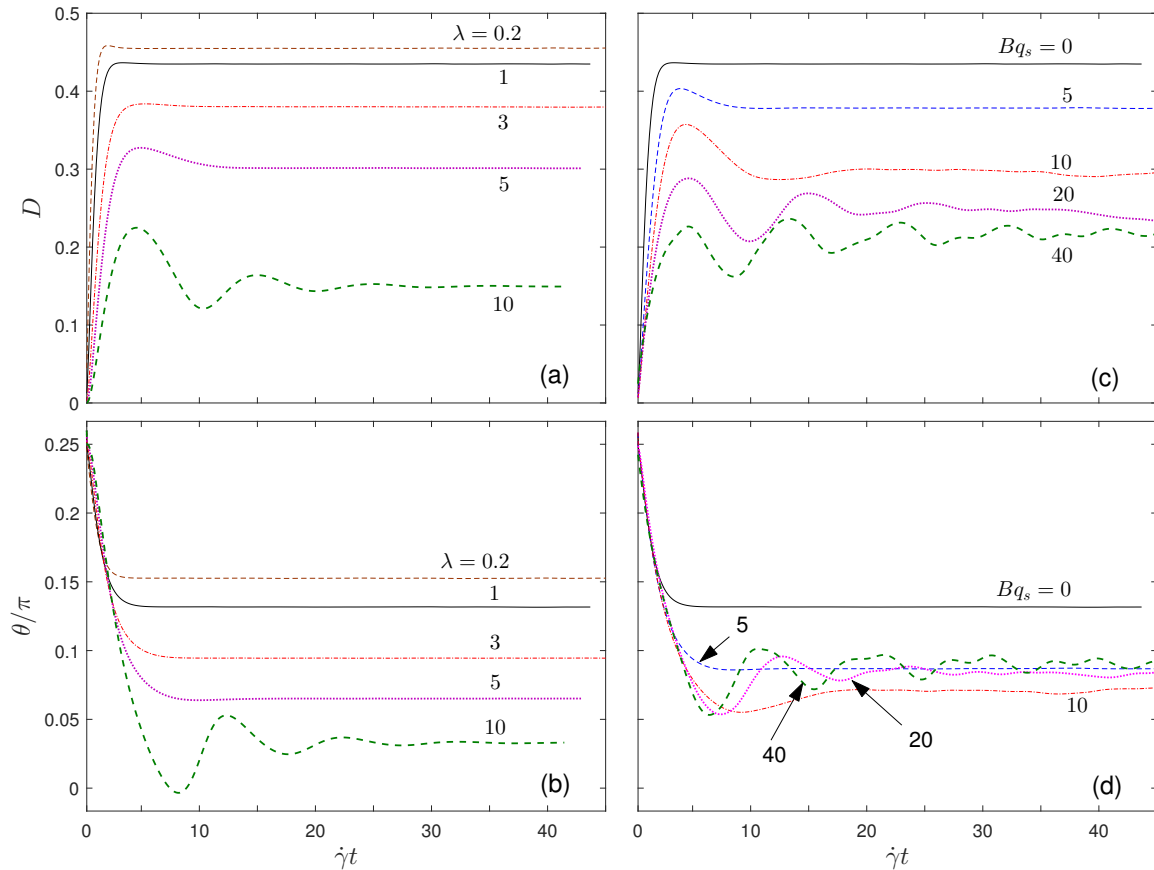


Figure 4.2: Variations of the capsule deformation  $D$  (a and c) and inclination angle  $\theta$  (b and d) with time in shear flows in responding to increases in interior fluid viscosity (a and b,  $Bq_s = 0$ ) and membrane viscosity (c and d,  $\lambda = 1$ ), respectively.

1, 3, 5, and 10; and (b) fluid viscosity ratio  $\lambda = 1$  with varying membrane viscosity  $Bq_s=0$ , 5, 10, 20, and 40. Figure 4.2 displays the evolution profiles of deformation index  $D$  and inclination angle  $\theta$  for capsules with these different fluid viscosity contrast  $\lambda$  or membrane viscosity  $Bq_s$  values. Starting from the case  $(\lambda, Bq_s)=(1, 0)$  (black solid lines), deformation index  $D$  decreases as the fluid viscosity contrast  $\lambda$  or the membrane viscosity  $Bq_s$  increases. Larger values of  $\lambda$  and  $Bq_s$  can introduce oscillations in the deformation index  $D$ , and a longer time is required for the capsule to reach a stable deformation state, the tank-treading state. It seems that  $Bq_s$  has a more significant effect on the deformation oscillation than the deformation magnitude when compared to the viscosity contrast  $\lambda$ . As an example, we look at the  $D$  variations for cases  $(\lambda, Bq_s)=(10, 0)$  in Figure 4.2(a) and  $(1, 40)$  in Figure

4.2(c), both as green dashed lines. Case (10, 0) reduces the deformation index  $D$  lower than Case (1, 40), however, the oscillation in  $D$  dies out quickly in case (10, 0) but it lasts much longer in case (1, 40). The different responses in the inclination angle  $\theta$  to the  $\lambda$  and  $Bq_s$  changes are more profound. While  $\theta$  continuously decreases as  $\lambda$  increases in Figure 4.2(b), the  $Bq_s$  effect is more complicated in Figure 4.2(d).  $\theta$  reduces with  $Bq_s$  first and reaches a minimum value at  $\sim 0.072\pi$  ( $13^\circ$ ) for  $Bq_s = 10$ . Further increasing  $Bq_s$  to 20 and 40, in addition to generating more significant and long-lasting oscillations, causes the inclination angle  $\theta$  rebound slightly. Based on these brief observations for  $D$  and  $\theta$ , it is evident that the membrane viscous effect cannot be simply represented by increasing the interior viscosity. Again we can take the case with  $(\lambda, Bq_s) = (1, 40)$  as a specific example. The equilibrium deformation 0.219 (the deformation as  $t \rightarrow \infty$ , estimated as the mean values of the last peak and valley values at  $\dot{\gamma} \sim 45$ ) might be generated using  $\lambda \sim 7.72$  and  $Bq_s = 0$  (purely elastic membrane); however, the strong oscillations in  $D$  and  $\theta$  and also the rebounded inclination angle cannot be reproduced from this pure elastic capsule.

Despite that several technical concerns have been raised [99, 122] for the membrane viscosity implementation in Ref. [9], we compare the capsule deformation  $D$  and inclination angle  $\theta$  results from our simulations to those from Ref. [9] in Fig. 4.3 for cases with  $Ca = 0.3$  and  $\lambda = 1$ . Similar calculations were also conducted by Gounley and Peng [58]; however, different membrane mechanics model and capillary number were used there. The general variation trends with  $Bq_s$  for both  $D$  and  $\theta$  from these two studies are similar: As the membrane viscosity  $Bq_s$  increases, the deformation index  $D$  decreases continuously, while the inclination angle  $\theta$  exhibits a decrease-then-increase dependence on  $Bq_s$ . When membrane viscosity is not involved ( $Bq_s=0$ ), a relatively good agreement is observed; how-

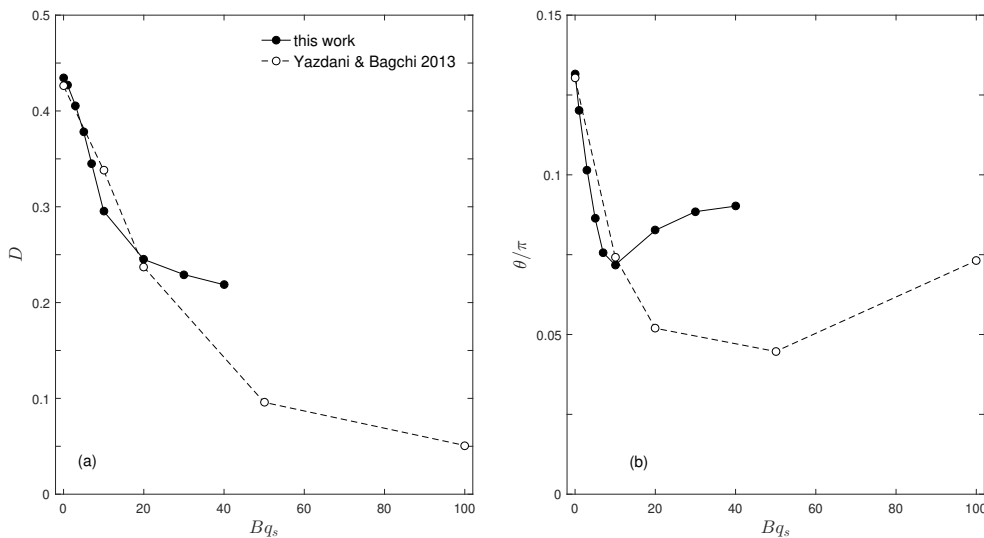


Figure 4.3: Comparison of the capsule deformation  $D$  (a) and inclination angle  $\theta$  (b) obtained in this work and those from Ref. [9] for  $Ca = 0.3$  and  $\lambda = 1$ .

ever, for  $Bq_s > 5$ , significant deviations exist between our results and those from Ref. [9]. Obviously this is due to the different methods used for the membrane viscosity. In particular, Yazdani and Bagchi [9] used the same elasticity ratio  $k'/k = 50$  for all cases. On the contrary, our non-dimensional analysis and numerical experiments [99, 122] have shown that  $k'$  is not related to the membrane elasticity  $k$ , instead, for a good accuracy, it should increase with the membrane viscosity  $Bq_s$ . In addition, our membrane viscosity method has been carefully validated by comparing simulation results to those from the boundary integral method for droplets with interfacial viscosity [2] and a satisfactory agreement is observed [99].

In addition to the deformation  $D$  and inclination angle  $\theta$ , we also examine several parameters for the capsule dynamics. Figure 4.4 shows the temporal variations of the position and velocity of a membrane marker point and the membrane circumference in the shear plane. For the convenience of our discussion, the deformed capsule shapes at  $\dot{\gamma}t=40$  are

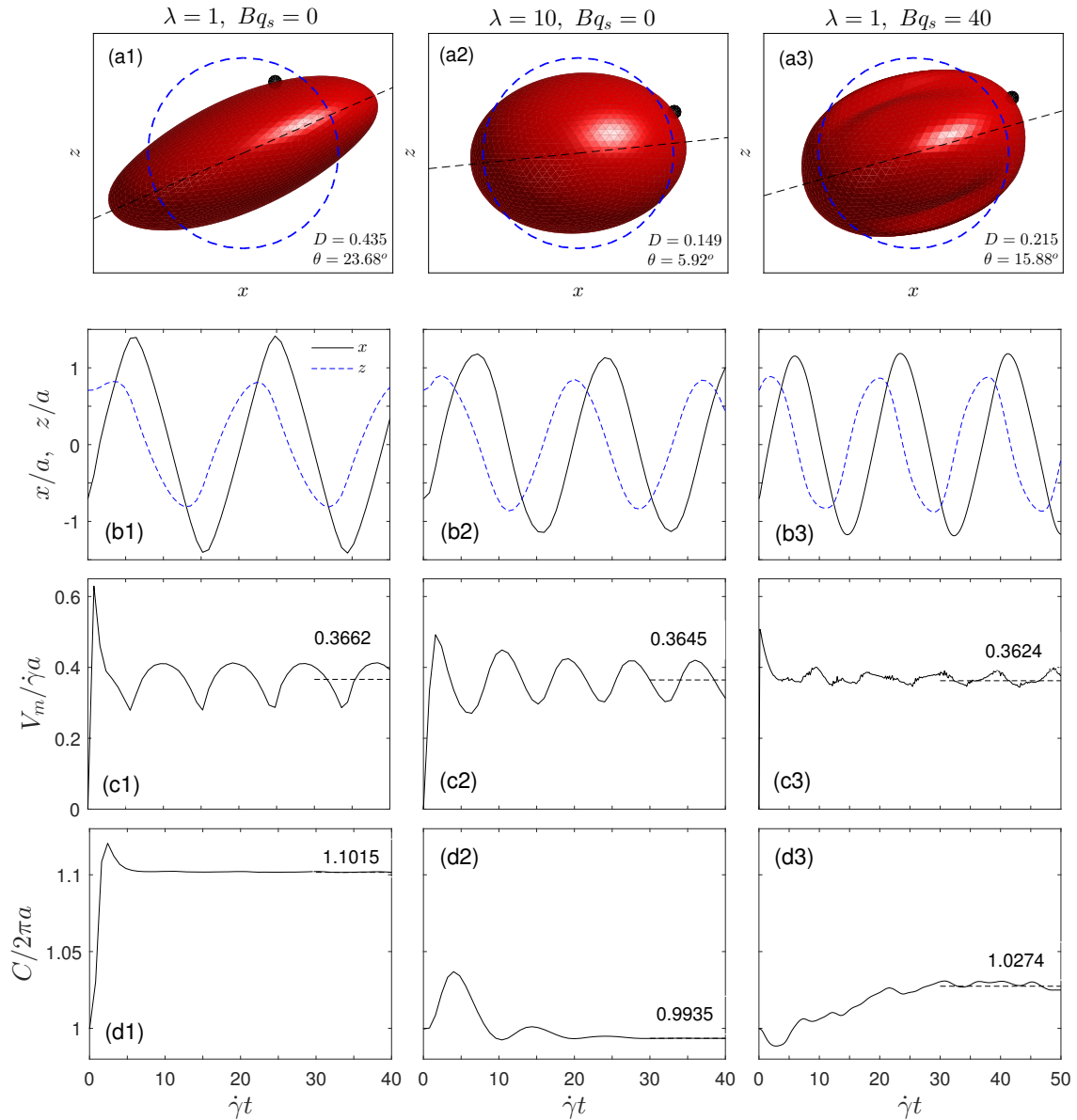


Figure 4.4: Three representative cases (labeled on top) for the individual effects of  $\lambda$  and  $Bq_s$  on capsule deformation dynamics: the deformed shapes at  $\dot{\gamma}t = 40$  (top row), the  $x$  and  $z$  positions of a membrane marker in the shear plane (second row); the marker velocity (third row), and the membrane circumference in the shear plane (bottom row). Also displayed in the top row panels are the black particles for a membrane node, the dashed circles for the original undeformed capsule shape, and the dashed straight lines for the inclination angle. In the third and bottom rows, the mean values calculated at the late stage of the simulations ( $\dot{\gamma}t = 30 \sim 50$ ) are displayed and indicated by dashed segments on the right.

also shown in the top row, with the black circle for the membrane marker and the blue dashed circles for the initial capsule shape in each panel. The  $x$ -position variation amplitude and circumference magnitudes can be intuitively related to the capsule deformation: The larger the deformation index  $D$ , the longer the capsule stretched in the shear flow, and therefore the larger  $x$  variation of the marker position and the longer capsule circumference. The  $z$  position of the marker point is related to the deformation  $D$  and the inclination angle  $\theta$ , and hence its variation is more complicated. For these three cases, the average membrane velocities (Figures 4.4(c1 to c3)) are very similar. The variations are significant for the two cases with  $Bq_s=0$ ; however, the strong membrane viscous effect in the case  $(\lambda, Bq_s)=(1, 40)$  inhibits the membrane velocity variation and therefore the strain rate of membrane deformation. As mentioned, there are two approaches to obtain the period and frequency of capsule rotation in shear flows: (a) from the periodic variations in the marker positions or (b) integrating the marker travel time along the membrane. The non-dimensional frequency values from these two methods for the three cases in Figure 4.4 are:  $\nu^* = 0.33490$  (method a) vs.  $0.33243$  (method b) for  $(\lambda, Bq_s)=(1, 0)$ ;  $0.36682$  vs.  $0.36685$  for  $(10, 0)$ ; and  $0.34874$  vs.  $0.35274$  for  $(1, 40)$ . The largest deviation, with a relative error of 1.14%, is observed in the case for  $(1, 40)$ , where the exact steady state has not been established and therefore the calculations are less accurate. Nevertheless, this comparison suggests that the two methods for rotation period and frequency yield close results; we only present frequency values from the travel time integration method (b) in the next sections. For these three cases, since the membrane velocity  $V_m^*$  is approximately the same ( $0.3624 \sim 0.3662$ ), and thus the relative frequency magnitude  $\nu^*$  is mainly determined by the circumference  $C^*$ : The maximum  $C^* = 1.1015$  corresponds to the minimum frequency in case  $(1, 0)$ , and the minimum  $C^* = 0.9935$  yields the maximum frequency in

case (10, 0). As to be seen in the next section, in general, the membrane velocity  $V_m^*$  actually plays a more determinant role than the circumference for the variation features of rotation frequency  $v^*$ .

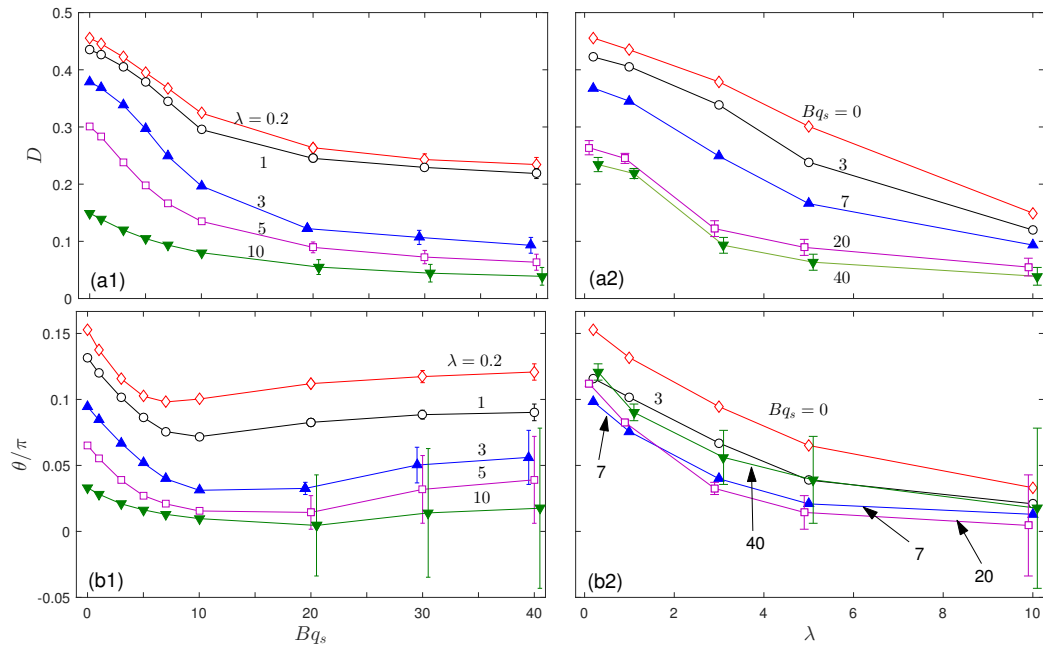


Figure 4.5: Simulated deformation  $D$  (top panels) and inclination angle  $\theta$  (bottom panels) with various  $\lambda$  and  $Bq_s$  combinations. Error bars are utilized to show the property variations at  $\dot{\gamma}t \sim 40$ , and the horizontal positions for data points with error bars at  $Bq_s = 20$ , 30, and 40 have been slightly shifted to avoid the overlapping of error bars.

### 4.3.3 Capsule Dynamics with Various $\lambda - Bq_s$ Combinations

Without considering the membrane viscosity, the effect of fluid viscosity contrast  $\lambda$  on the capsule and RBC dynamics in shear flows has been studied extensively [43, 44, 66, 81]. On the other hand, in the few numerical studies of membrane viscosity effect [9, 99], the fluid viscosity contrast  $\lambda$  is set at 1. For a more complete picture of the capsule behaviors in shear flows under different fluid and membrane viscosity situations, extensive calculations are conducted in this research with a  $\lambda \times Bq_s$  matrix covering ranges of  $0.2 \sim$

10 for  $\lambda$  and of  $0 \sim 40$  for  $Bq_s$ . In these simulations, the change of capsule volume is limited in a range of  $\pm 0.2\%$  of the initial volume, indicating the numerical mass leakage is negligible. Results for deformation index  $D$  and inclination angle  $\theta$  from these simulations are collected in Figure 4.5. For a better visualization of the dependence of  $D$  and  $\theta$  on  $\lambda$  and  $Bq_s$ , we plot the same set of results in two different ways: one as constant- $\lambda$  curves in the left panels, and one as constant- $Bq_s$  lines in the right panels. For cases with large  $\lambda$  ( $\geq 3$ ) and  $Bq_s$  ( $\geq 20$ ) values, the oscillations observed in Figure 4.2, especially for the inclination angle  $\theta$ , become more profound. For these cases, we show the estimated equilibrium values with error bars for the variation ranges in the left panels. Also to avoid the overlapping of error bars, we shift the horizontal positions slightly for data points with larger variation magnitudes. The error bars are not displayed in the right panels for clarity. The observations for  $D$  and  $\theta$  with  $\lambda = 1$  in the previous section, namely the monotonic decrease in  $D$  and the decrease-then-increase transition in  $\theta$  with  $Bq_s$ , are confirmed for other  $\lambda$  values (Figures 4.5(a1, b1)). The decreasing slope in  $D$  is steeper at low  $Bq_s$  values and it becomes more gentle at high  $Bq_s$  values. For the  $\theta \sim Bq_s$  curves with  $\lambda = \text{constant}$ , the turning point from the relatively fast declining to the slow recovery shifts to the right (i.e., higher  $Bq_s$  values) for larger viscosity contrast  $\lambda$  values. For the constant- $Bq_s$  curves in the right panels, both  $D$  and  $\theta$  decrease monotonically with  $\lambda$ , consistent with the lower curves at higher  $\lambda$  values in Figures 4.5(a1, b1). The  $D \sim \lambda$  curve for  $Bq_s = 0$  appears linear, however, the non-linearity becomes more evident at high  $Bq_s$  values. Due to the  $\theta$  rebound with  $Bq_s$ , the  $\theta \sim \lambda$  curves with constant- $Bq_s$  tangle together, except the  $Bq_s = 0$  curve. These curves are concave and the declining slope becomes flatter at larger  $\lambda$  values. For  $\lambda$  up to 10 calculated here, we do not see the turning-up trend in  $\theta \sim \lambda$  curves.

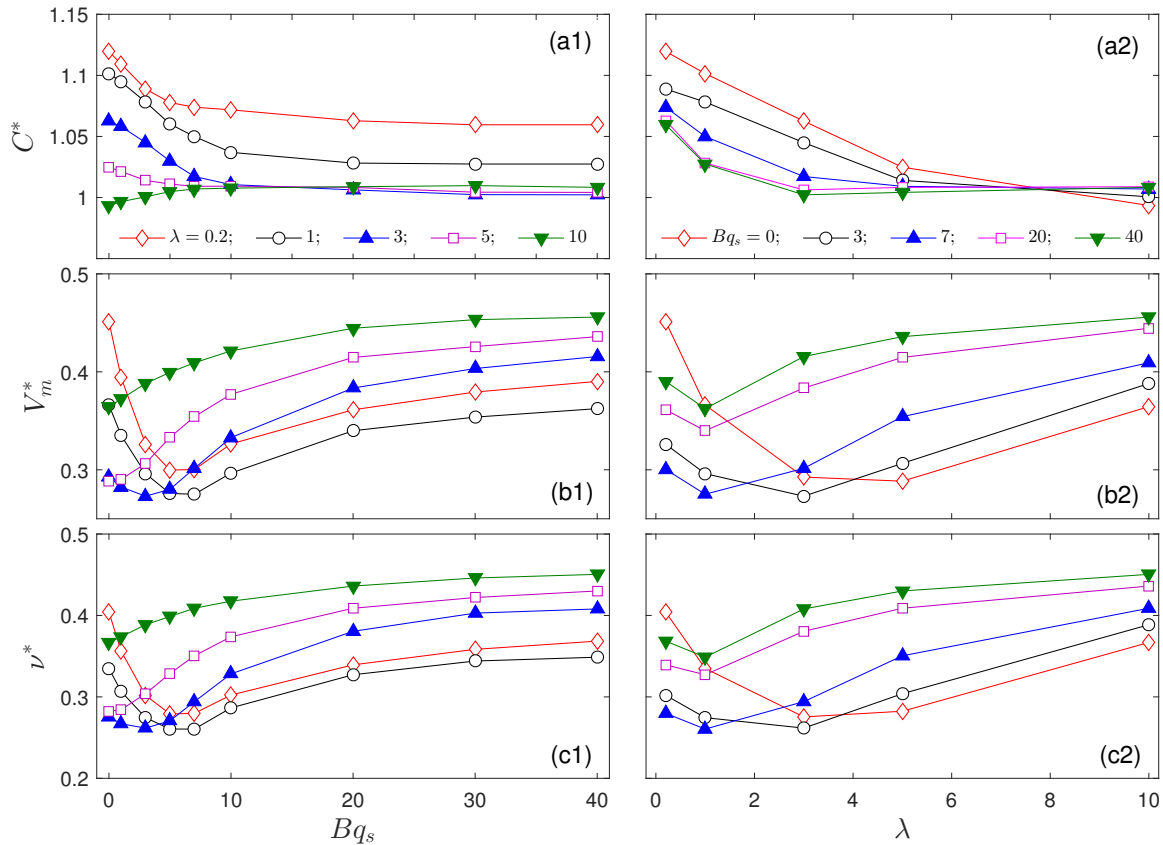


Figure 4.6: Simulated capsule circumference  $C^*$  (a1 and a2), membrane velocity  $V_m^*$  (b1 and b2) and rotation frequency  $\nu^*$  (c1 and c2) changing with membrane viscosity coefficient  $Bq_s$  (left) and fluid viscosity ratio  $\lambda$  (right).

To examine the rotation frequency behaviors, we plot the circumference  $C^*$ , mean membrane velocity  $V_m^*$ , and the rotation frequency  $\nu^*$  in Figure 4.6. The circumference  $C^*$  and the deformation index  $D$  are both calculated in the shear plane, and they are both determined directly by the deformed capsule shape. A larger  $D$  means that the capsule has deformed more severely from the original spherical shape, and thus a longer circumference  $C^*$  is expected. This is true for most cases with relatively large deformation index  $D$  in our simulation results, as indicated by the general decreasing trend in the  $C^* \sim Bq_s$  and  $C^* \sim \lambda$  plots (Figures 4.6 (a1, a2)). For those cases with  $D < 0.2$  in Figures 4.5(a1, a2), the corresponding circumference  $C^*$  are approximately 1 and no apparent difference is observed. In particular, for the cases of  $\lambda = 10$  (green downward triangles in Figure 4.6(a1)),

we have  $C^* = 0.9935$  at  $Bq_s = 0$  (see the capsule shape in Figure 4.4(a2)), and it gradually increases with  $Bq_s$ , while the deformation index  $D$  is decreasing with  $Bq_s$ .  $C^* < 1$  suggests that the cross-sectional area in the shear plane has reduced and accordingly the dimension in the rotation axial direction (the direction perpendicular to the shear plane) will increase, considering the nearly constant capsule volume during the simulation. For example, for the minimum  $C^*$  case in Figure 4.6(a1) with  $\lambda = 10$  and  $Bq_s = 0$ , the capsule dimension in the rotation axial direction increases to  $2.08a$  from the original capsule diameter  $2a$ .

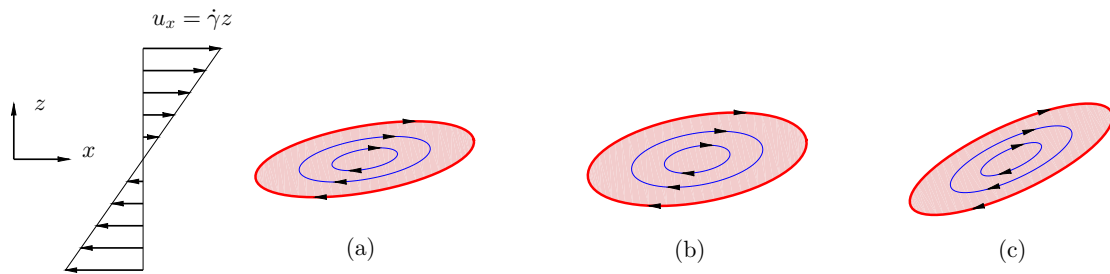


Figure 4.7: Schematic illustrations for the effects on capsule deformation and inclination on membrane velocity in shear flow. Compared to the reference configuration in (a), Capsule (b) has the same inclination angle but a smaller deformation, and Capsule (c) has the same deformation but a larger inclination angle.

The membrane velocity  $V_m^*$  in Figures 4.6(b1, b2) exhibits interesting patterns. In general, a spoon-like curve is noticed in for both  $V_m^* \sim Bq_s$  and  $V_m^* \sim \lambda$  curves. The membrane velocity decreases first and then turns up and starts to increase with  $Bq_s$  or  $\lambda$ . With the relatively small variation range in the circumference  $C^*$  ( $0.9935 \sim 1.1196$ , variation  $\pm 5.97\%$ ) compared to that in the membrane velocity  $V_m^*$  ( $0.273 \sim 0.456$ , variation  $\pm 25.08\%$ ), the rotation frequency  $\nu^* = V_m^*/C^*$  in Figures 4.6(c1, c2) has very similar spoon-like variations to  $V_m^*$ . Similar behaviors for the rotation frequency  $\nu^*$  has also been reported by Yazdani and Bagchi [9] for systems with  $\lambda = 1$  and different capillary numbers  $Ca$ , although

some technical concerns have been raised [99]. The authors provided qualitative analysis on the correlation between the inclination angle  $\theta$  and rotation frequency  $v^*$  in terms of the competition and balance of moments from the external shear flow, capsule inclination oscillation, and capsule rotation. Here we attempt to explore the mechanism for the spoon-like  $V_m^*$  profile shape based on the deformation  $D$  and inclination angle  $\theta$ , both commonly measured in capsule and RBC rheology experiments. Consider the three capsule configurations in the same external shear flow as shown in Figure 4.7. Here capsule (a), with a certain deformation index  $D_a$  and inclination angle  $\theta_a$ , serves as the comparison reference. Capsule (b) has the same inclination angle  $\theta_b = \theta_a$ , but with a smaller deformation index  $D_b < D_a$ . On the other hand, capsule (c) has the same deformation index  $D_c = D_a$  however a larger inclination angle  $\theta_c > \theta_a$ . A capsule with a smaller  $D$  (cases b vs. a) is associated with a larger width  $W$  in the minor axis direction (close to the shear gradient direction). Similarly, for the same capsule shape in (a) and (c), the larger inclination angle  $\theta_c$  makes the capsule tilted more vertically. From an intuitive, fluid mechanics point of view, the disturbance on the external shear flow caused by the capsule, and therefore the resulted membrane movement, are more profound in cases (b) and (c) than in case (a). A general statement can be made based on this simple analysis: the membrane velocity  $V_m^*$  increases with the inclination angle  $\theta$  and decreases with the deformation index  $D$ . With this general relation established, now we can look back at the spoon-like variation of  $V_m^*$  again. We take the  $V_m^* \sim Bq_s$  curve with  $\lambda = 0.2$  (red line with diamonds in Figure. 4.6-b1) as an example. For low  $Bq_s$  values ( $Bq_s < 6$ ), the inhibiting effect from the declining  $\theta$  (Figure 4.5(b1)) and the promoting effect from the declining  $D$  (Figure 4.5(a1)) compete with each other, and it appears that the fast drop in  $\theta$  (Figure 4.5(b1)) dominates more on the membrane velocity behavior, resulting in a decrease in  $V_m^*$  in this  $Bq_s$  range. As  $Bq_s$  further increases

( $Bq_s > 6$ ),  $\theta$  increases up slightly and then stays approximately constant. In the meantime, deformation  $D$  keeps decreasing with  $Bq_s$ . Consequently, the membrane velocity  $V_m^*$  starts to increase after  $Bq_s > 6$ . However, due to the relatively slow increase trend in  $D$ , and probably also the less profound influence of  $D$  than  $\theta$  as discussed in the  $Bq_s < 6$  range, the increase of  $V_m^*$  for  $Bq_s > 6$  is gentle and becomes very slow at high  $Bq_s$ . Connecting the fast drop at low  $Bq_s$  and the slow increase at high  $Bq_s$ , we have the spoon-like  $V_m^*$  variation in Figure 4.6(b1). As the fluid viscosity ratio  $\lambda$  increases from 0.2 to 10, the declining slope of  $\theta$  in the low  $Bq_s$  end flattens, and the inhibiting effect from the reducing  $\theta$  becomes less dominant compared to the promoting effect from the reducing  $D$ . This causes the minimum location of  $V_m^*$  shift left and the  $V_m^*$  valley become less apparent, and even completely disappear for  $Bq_s \geq 5$ . With the circumference  $C^*$  approximately constant, the rotation frequency  $v^*$  shows very similar variation patterns as those for  $V_m^*$  we describe above. However, for quantitative values, the circumference may play the determinant role on the frequency value when the membrane viscosity is relatively constant, just like the three cases in Figure 4.4.

After discussing the  $V_m^*$  and  $v^*$  variations with  $Bq_s$  in Figure 4.6(b1), the  $V_m^* \sim \lambda$  plot in Figure 4.6(b2) can be understood easier. Unlike the decrease-then-increase response of  $\theta$  to  $Bq_s$  in Figure 4.5(b1), the declination of angle  $\theta$  with  $\lambda$  in Figure 4.5(b2) is monotonic. Nevertheless, the different declining fashions for deformation  $D$  and inclination angle  $\theta$  with the fluid viscosity ratio  $\lambda$  (i.e., the approximately linear  $D \sim \lambda$  curves in Figure 4.5(a2) versus the gradual decrease in the  $\theta$  declination slope in Figure 4.5(-b2)) implies that the promoting effect from deformation angle  $D$  could have overcome the inhibiting effect for inclination  $\theta$  as  $Bq_s$  increases. The combined promoting and inhibiting effects result

in the particular decrease-then-increase variations in Figure 4.6-b2. The relatively wide transition range of  $\lambda$  here could be attributed to the gentle variations in the declination slope in Figures 4.5(a2, b2). The minimum locations of the  $V_m^* \sim \lambda$  curves also shift left as  $Bq_s$  increases, and this might be related to the more profound non-linearity in  $D \sim \lambda$  curves at larger  $Bq_s$  values in Figure 4.5(a2). Again, with the limited variation range for the circumference  $C^*$ , the rotation frequency  $\nu^*$  shown in Figure 4.6(c2) exhibits similar variation features as the membrane velocity  $V_m^*$  in Figure 4.6(b2). We would like to clarify that all the above analysis and discussions for the correlations among  $D$ ,  $\theta$ ,  $V_m^*$  and  $\nu^*$  are at the qualitative level, and one should not apply them for quantitative comparisons.

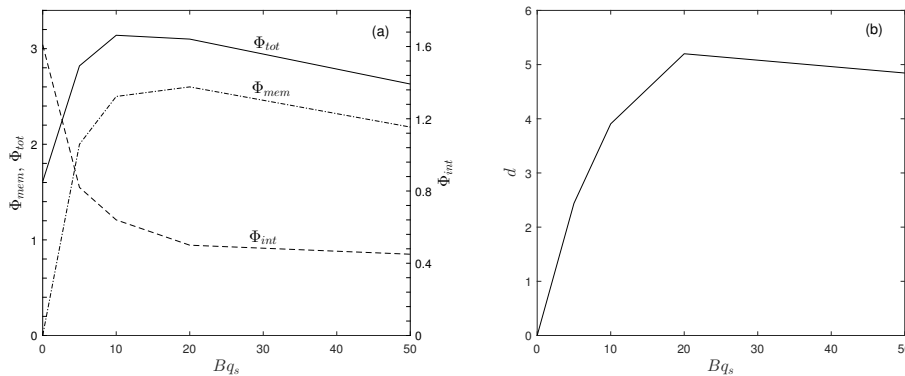


Figure 4.8: A reproduction of Figure 13b in Ref. [9] for the energy dissipation rates  $\Phi_{mem}$  due to membrane viscosity  $\mu_s$ ,  $\Phi_{int}$  due to interior fluid viscosity  $\mu_c$ , and the sum of them  $\Phi_{tot} = \Phi_{mem} + \Phi_{int}$  at different membrane viscosity  $Bq_s$ . The energy dissipation ratio  $d$  calculated from these dissipation rates via  $d = \Phi_{mem}/\Phi_{int}$  is plotted in (b), showing a strong non-linear relationship between  $d$  and  $Bq_s$ .

#### 4.3.4 On the Energy Dissipation Ratio $d$

As briefly reviewed in the Introduction section, the energy dissipation ratio  $d$ , defined as the ratio of the energy dissipation rate due to the membrane viscosity to that due to the interior fluid viscosity, has been often used to characterize the membrane viscous effect for

capsule and cell dynamics [9, 33, 57, 112, 120]. In particular, Tran-Son-Tay et. al [57] calculated the membrane viscosity  $\mu_s$  and energy dissipation ratio  $d$  from experimental results of RBCs using the mathematical description for tank-treading elliptical capsules by Keller and Skalak [112]. The membrane viscosity is found approximately constant at high shear rates ( $\dot{\gamma} > 100 \text{ s}^{-1}$ ), but the dissipation ratio  $d$  appears continually increase with the shear rate even for the same RBCs. Also, Yazdani and Bagchi [9] presented the dissipation rates due to membrane and interior fluid viscosities with different membrane viscosity  $Bq_s$  for constant fluid viscosity ratio  $\lambda = 1$  and capillary number  $Ca = 0.3$ . One may expect a linear relationship between the dissipation ratio  $d$  and the only variable  $Bq_s$  there. We calculate the dissipation ratio  $d$  from the dissipation rates in Ref. [9], and the calculated  $d \sim Bq_s$  plot shows strong non-linearity (Figure 4.8). In particular, the membrane dissipation rate decreases with the membrane viscosity increase for larger  $Bq_s$  values, meaning the membrane-interior dissipation ratio is smaller for capsules with more viscous membranes. This analysis implies that it is not appropriate to elevate the interior fluid viscosity to compensate the membrane viscous effect.

In this section, other than calculating the membrane and interior dissipation rates explicitly, we check the functional relationships among the system parameters. For all the cases we simulate in this research, we have two independent input variables,  $\lambda$  and  $Bq_s$ . The systems we consider here then is a 2D system in mathematics, and all parameters for the capsule dynamics description are functions of  $\lambda$  and  $Bq_s$  only, for example,  $D = D(\lambda, Bq_s)$  and  $\theta = \theta(\lambda, Bq_s)$ . If the membrane viscous effect due to a certain  $Bq_s$  can be accurately represented by an elevated interior fluid viscosity  $\lambda_{app} = \lambda + d$  and  $Bq_s = 0$  (the ratio  $d$  does not need to be a constant), then the 2D  $(\lambda, Bq_s)$  system is then converted to a 1D system

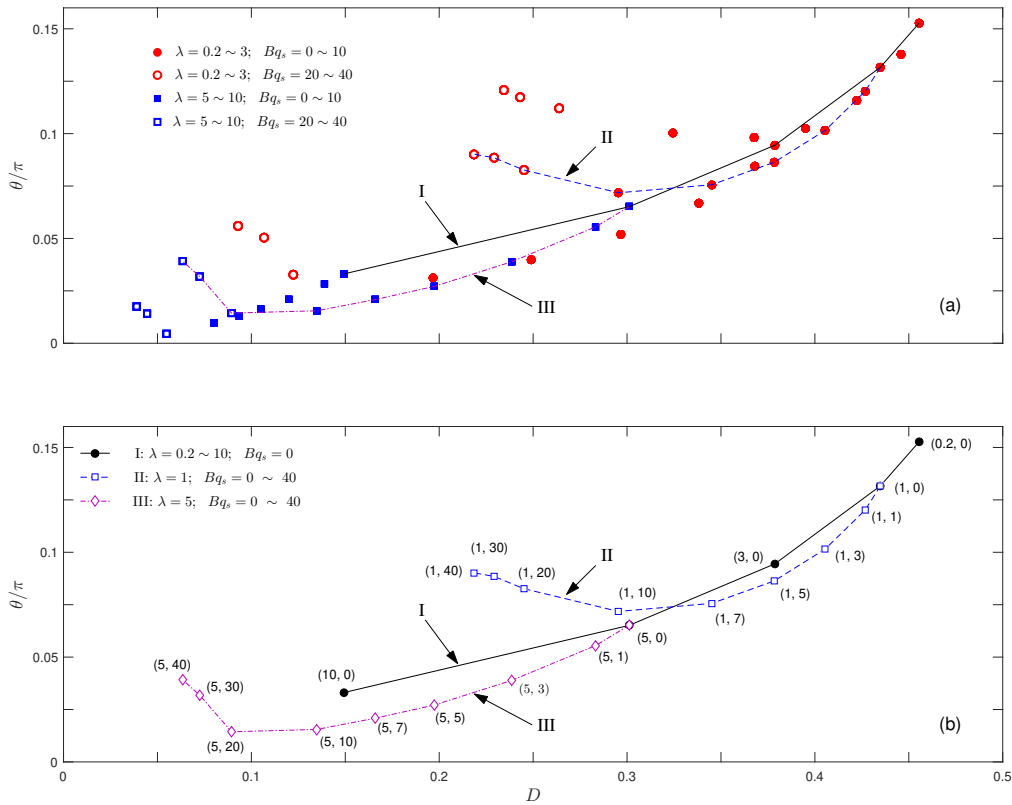


Figure 4.9: Simulated capsule deformation  $D$  and inclination angle  $\theta$  for all cases considered in this study with various  $(\lambda, Bq_s)$  combinations. Four different symbols are adopted to indicate the  $\lambda$  and  $Bq_s$  ranges: red circles for  $\lambda$  in  $0.2 \sim 3$  versus blue squares for  $\lambda$  in  $5 \sim 10$ , and filled symbols for  $Bq_s$  in  $0 \sim 10$  versus open symbols for  $Bq_s$  in  $20 \sim 40$ . Three specific series of such  $(\lambda, Bq_s)$  data points are connected by lines: Curve I for  $\lambda = 0.2 \sim 10$  and  $Bq_s = 0$ , Curve II for  $\lambda = 1$  and  $Bq_s = 0 \sim 40$ , and Curve III for  $\lambda = 5$  and  $Bq_s = 0 \sim 40$ . These curves and data points are re-presented in (b) for clarity and convenience of our discussions in the text. The respective  $\lambda$  and  $Bq_s$  values for each data point in (b) are also provided in parenthesis in the format of  $(\lambda, Bq_s)$ .

with the only independent variable  $\lambda_{app}$ . Therefore all parameters for the capsule dynamics are single-variable functions of  $\lambda_{app}$  such as  $D = D(\lambda_{app})$ ,  $\theta = \theta(\lambda_{app})$ ,  $V_m^* = V_m^*(\lambda_{app})$ ,  $v^* = v^*(\lambda_{app})$ , etc. Since all these single-variable functions depend on the same variable  $\lambda_{app}$ , we should see a smooth curve if we plot a pair of any these parameters in a graph. To verify this hypothesis, we plot the  $\theta \sim D$  data points for all cases considered in this research in Figure 4.9. Four types of symbols are employed to indicate the ranges of  $\lambda$  and  $Bq_s$ : filled red circles for  $\lambda \leq 3$  and  $Bq_s \leq 10$ , open red circles for  $\lambda \leq 3$  and  $Bq_s \geq 20$ , filled blue squares for  $\lambda \geq 5$  and  $Bq_s \leq 10$ , and open blue squares for  $\lambda \geq 5$  and  $Bq_s \geq 20$ . Clearly no one-to-one correlation can be established and the points are scattered in a wide area in the  $\theta \sim D$  space: For a same deformation  $D = 0.24$ , the inclination angle  $\theta$  can vary in a range of  $7^\circ \sim 21^\circ$  ( $\theta/\pi = 0.0389 \sim 0.1167$ ); and for a same angle  $\theta = 16^\circ$  ( $0.0889 \pi$ ), the deformation  $D$  can assume a value between 0.22 and 0.39. Even for the filled symbols (low membrane viscosity,  $Bq_s \leq 10$ ) where a general variation trend might be established, significant dispersion still exists. In the group of  $\lambda \leq 3$  and  $Bq_s \leq 10$  (filled red circles), for a deformation  $D \sim 0.33$ , the inclination angle  $\theta$  varies in a range of  $(0.067 \sim 0.1)\pi$  ( $12^\circ \sim 18^\circ$ ); and for the angle  $\theta \sim 0.1\pi$  ( $18^\circ$ ), the deformation  $D$  can have values from 0.33 to 0.40. Similarly for the group of  $\lambda \geq 5$  and  $Bq_s \leq 10$  (filled blue squares), at  $\theta = 0.033\pi$  ( $6^\circ$ ), the deformation  $D$  can be as small as 0.15 or as large as 0.22. Obviously large errors would be introduced if one attempts to fit them with a smooth curve. This clearly illustrates that for the two commonly used tank-treading parameters,  $D$  and  $\theta$ , no such one-to-one relationship exists, even for systems with limited  $\lambda$  and  $Bq_s$  ranges.

Furthermore, we connect the data points for three series: Curve I for  $Bq_s = 0$  and  $\lambda = 0.2 \sim 10$ , Curve II for  $\lambda = 1$  and  $Bq_s = 0 \sim 40$ , and Curve III for  $\lambda = 5$  and  $Bq_s = 0 \sim$

40; and these data points and curves are displayed separately in Fig. 4.9b for clarity and convenience of our following discussions. Curve I describes the  $D \sim \theta$  dependence for capsules with non-viscous membrane as the fluid viscosity ratio  $\lambda$  varies from 0.2 to 10. When the membrane viscosity is introduced, the  $D \sim \theta$  curves, Curve II for  $\lambda = 1$  and Curve III for  $\lambda = 5$ , deviate from the non-viscous Curve I quickly from the starting points, case  $(\lambda, Bq_s)=(1, 0)$  for Curve II and case  $(5, 0)$  for Curve III. The viscous Curves II and III proceed first below the non-viscous Curve I, then bend upward and finally overpass Curve I at high  $Bq_s$  values. This is consistent to the continuous decrease in  $D$  and the decrease-then-increase variation pattern of  $\theta$  with  $Bq_s$  as discussed above. The deviation of Curves II and III from Curve I in Fig. 4.9b clearly illustrates the impropriety for compensating membrane viscosity with an elevated interior fluid viscosity. Take the case  $(\lambda^0, Bq_s^0)=(1, 5)$  on Curve II as an example, and we denote its deformation as  $D^0$  and its inclination angle as  $\theta^0$ . Assume this capsule can be represented with an equivalent capsule (i.e., same deformation  $D^* = D^0$  and same inclination angle  $\theta^* = \theta^0$ ) with no membrane viscosity  $Bq_s^* = 0$  but a higher interior fluid viscosity  $\lambda^* > \lambda^0$ . Considering the relatively low membrane viscosity  $Bq_s^0 = 5$ , it is reasonable to assume  $\lambda^* < 10$ . Since the new capsule  $(\lambda^*, 0)$  has no membrane viscosity, its deformation and inclination  $(D^*, \theta^*)$  should correspond to a point on the non-viscous Curve I in Fig. 4.9b. Clearly this is not what we see in the plot: instead  $(D^* = D^0, \theta^* = \theta^0)$  for case  $(1, 5)$  locates below the point for case  $(3, 0)$  on Curve I. Similar discussions can be made for other points on Curves II and III such as cases  $(1, 20)$  and  $(5, 3)$ . Based on these results from the systems we consider, we therefore question the appropriateness and accuracy of using an elevated interior fluid viscosity to compensate the membrane viscous effect in theoretical and numerical analysis

of capsule dynamics.

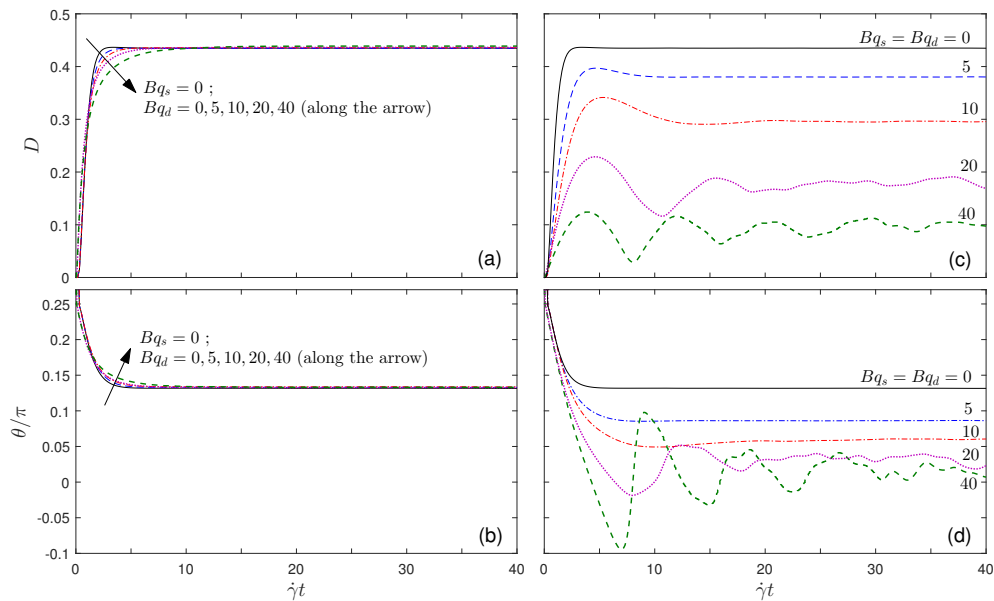


Figure 4.10: Variations of the capsule deformation  $D$  (a and c) and inclination angle  $\theta$  (b and d) with time in shear flows in responding to increases in dilatational viscosity  $Bq_d$  alone (a and b,  $Bq_s = 0$ ) and in combination with the shear viscosity (c and d,  $Bq_s = Bq_d$ ), respectively.

### 4.3.5 Effect of Dilatational Membrane Viscosity

Considering the large dilation modulus for biological vesicle and cell membranes [50], we have been focusing on the effect of shear membrane viscosity  $Bq_s$  so far in this research, as in previous studies [9, 58]. However, the relatively low dilation modulus  $C = 1$  used in this work does allow the membrane area to change, especially for large deformation  $D$ : For the cases with  $D = 0.4 \sim 0.5$ , the membrane area increases  $\sim 14\%$  from the original area  $4\pi a^2$ . Here we examine the dilatational membrane viscosity effect, alone and in combination with the shear membrane viscosity. Similarly, a dilatational Boussinesq number is defined as  $Bq_d = \mu_d / \mu_0 a$ , where  $\mu_d$  is the dilatational membrane viscosity in Eq. (4.6). Two sets of simulations are performed: (1) with the dilatational viscosity  $Bq_d = 0 \sim 40$  but no shear

viscosity ( $Bq_s = 0$ ), and (2) with the shear and dilatational viscosities varying together as  $Bq_s = Bq_d = 0 \sim 40$ . The fluid viscosity contrast  $\lambda$  is held at 1 in these simulations.

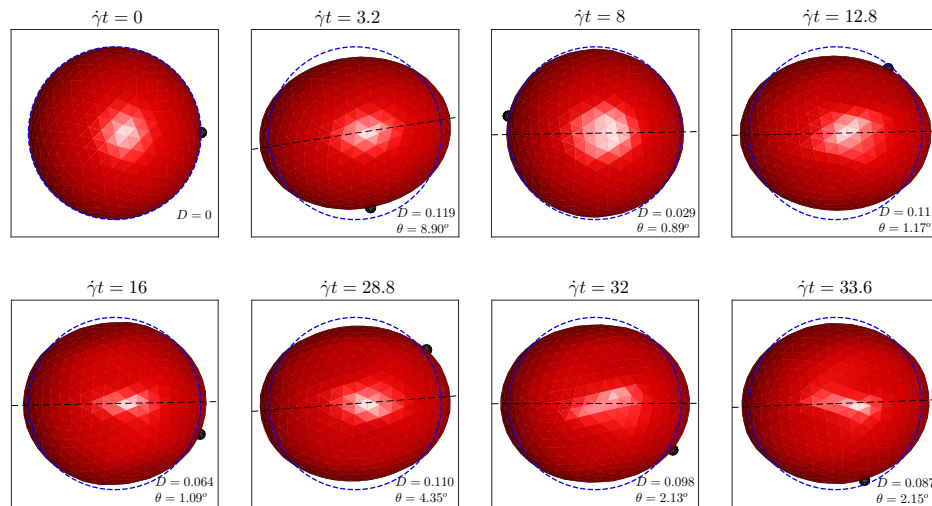


Figure 4.11: Capsule shapes during the deformation process of  $Bq_s = Bq_d = 40$  in shear flows. The dashed blue circles denote the original undeformed capsule shape for comparison, and the black dots represent the positions of one membrane node to show the membrane rotation. The dashed straight lines are plotted based on the calculated inclination angle  $\theta$  values, which are also shown with the deformation  $D$  in each subplot.

Figure 4.10 shows the evolution processes of the capsule deformation  $D$  and inclination angle  $\theta$  when the shear flow is imposed. When the shear viscosity is absent ( $Bq_s = 0$ ), the dilatational viscosity  $Bq_d$  alone has negligible influence on the capsule deformation and inclination after the steady tank-treading state is established; however, the transition process is prolonged as  $Bq_d$  increases (Figures 4.10(a, b)). The relatively weak influence of  $Bq_d$  on  $D$  and  $\theta$  is similar to those observed in previous studies for droplets [2, 99]; and it is reasonable to see that a larger  $Bq_d$  slows down the deformation process since the membrane viscosity, by definition, attempts to reduce the deformation rate (Eq. 4.6). Comparing Figures 4.2(b, d) and 4.10(b, d), it is interesting to note that the addition of  $Bq_d$  only starts to play an apparent role when  $Bq_s = Bq_d > 10$ , before which the steady tank-

treading deformation  $D$  and inclination angle  $\theta$  appear approximately the same for  $Bq_s$  only and  $Bq_s = Bq_d$  cases. For  $Bq_s = Bq_d > 10$  cases,  $Bq_d$  further enhances the suppression effect from  $Bq_s$  on the capsule deformation and also reduces the inclination angle  $\theta$  to lower values. This could be associated with the unsteady oscillations in  $D$  and  $\theta$  in these cases, since larger viscous stresses will be generated in the membrane with stronger oscillations and such viscous stresses will restrain the capsule deformation. The oscillation amplitude, especially for  $\theta$ , becomes more profound in cases  $Bq_s = Bq_d = 20$  and  $Bq_s = Bq_d = 40$ . This might be due to the nearly undeformed capsule shape, for which the calculated value for the inclination angle from the method in Ref. [43] become very sensitive. To illustrate this aspect, in Figure 4.11 we plot the capsule shapes at several representative instants during the deformation process of  $Bq_s = Bq_d = 40$ . It can be seen that, after  $\dot{\gamma}t > 16$ , the capsule shape and orientation are very similar, although apparent oscillations exist in the calculated  $D$  and  $\theta$  values in Figures 4.10(b, d).

Now we briefly discuss the applicability of the energy dissipation ratio  $d$  for systems with the dilatational viscosity  $Bq_d$  involved. Apparently, according to Figures 4.10(a, c), at the steady state, we should have  $d \approx 0$  for  $Bq_d$  alone since the changes in  $D$  and  $\theta$  with  $Bq_d$  are negligible there. On the other hand, the  $Bq_d$  influence during the deformation process is obvious. This poses a dilemma on the choice of energy dissipation ratio  $d$ :  $d = 0$  or  $d > 0$ , if one plans to simulate such systems by increasing the interior viscosity to replace the  $Bq_d$  effect. For the  $Bq_d = Bq_s$  cases in Figure 4.10(b, d), we see  $Bq_d$  has a weak influence on the capsule dynamics for  $Bq_d = Bq_s < 15$ , but the  $Bq_d$  effect becomes much more significant for  $Bq_d = Bq_s = 20$  and 40. Again this disagreement makes the selection of an appropriate  $d$  value very difficult: The  $d$  value for  $Bq_d = Bq_s = 10$  should be approximately the same as

that for  $Bq_d = 0$  and  $Bq_s = 10$ , but on the other side,  $d$  for  $Bq_d = Bq_s = 20$  should be quite different from that for  $Bq_d = 0$  and  $Bq_s = 20$ . Without the general proportionality between  $d$  and the membrane viscosity ( $Bq_s$ ,  $Bq_d$ , or their combination), the practical usefulness of  $d$  for theoretical analysis and numerical simulations is debatable.

#### 4.4 Conclusion

We have simulated the capsule deformation processes in shear flow with various membrane and interior fluid viscosity values to explore their individual and combined effects on the capsule dynamics. Our results show that, while both higher membrane and interior fluid viscosities can reduce the capsule deformation, their effects on the inclination angle are distinctive. The inclination angle decrease monotonically with the interior fluid viscosity increase; however, a decrease-then-increase variation is noticed for inclination angle response to the membrane viscosity increase. In addition, compared to a higher interior fluid viscosity, a higher membrane viscosity can introduce more severe oscillations in the capsule deformation and inclination angle. A simple, intuitive mechanics has also been proposed to qualitatively explain the spoon-like variations in membrane velocity and capsule rotation frequency from the observed capsule deformation and inclination. At last, we have examined the validity and accuracy of the simplification treatment suggested in previous studies of replacing the membrane viscous effect with an elevated interior fluid viscosity. For the systems studied in this research ( $Ca = 0.3$ ,  $\lambda = 0.2 \sim 10$ , and  $Bq = 0 \sim 40$ ), our results and analysis suggest that the membrane viscous effect cannot be accurately represented by increasing the interior fluid viscosity, and explicit modeling of the membrane

viscosity is necessary in future theoretical and numerical studies for capsule dynamics.

We acknowledge that our simulations are limited to originally spherical capsules and we have held the capillary number at 0.3. According to previous studies for capsules with pure elastic membranes [44, 81], the definition of the capillary number  $Ca$ , the capsule deformation increases and the inclination angle decreases as the capsule appears more flexible at a larger  $Ca$ . We anticipate that these general trends will be still true when membrane viscosity is involved; however, the detailed dynamic features are difficult to predict considering the complex non-linear and non-monotonic relationships among system parameters. In addition, other system parameters and situations, such as the constitutive relations for membrane elasticity, the pre-stress state of the capsule, and more general flow situations, can affect the capsule dynamic behaviors as well as the roles played by the membrane and interior fluid viscosities. All these are interesting topics for future research for a better understanding of the complex capsule dynamics and the individual and combined roles of these system parameters. Nevertheless, our results, analysis and discussions in this paper have revealed the complexity of capsule dynamics, and therefore attention needs to be executed on modelling the membrane viscosity accurately.

## **Acknowledgment**

We thank the anonymous reviewers for carefully reviewing the manuscript and providing critical comments and constructive suggestions. This work was supported by the Natural Science and Engineering Research Council of Canada (NSERC). The calculations have been enabled by the use of computing resources provided by WestGrid (westgrid.ca),

SHARCNet ([sharcnet.ca](http://sharcnet.ca)), and Compute/Calcul Canada ([compute canada.org](http://compute canada.org)). P.L. acknowledges the financial support from the Ontario Trillium Scholarship at Laurentian University.

# Chapter 5

## Concluding Statements

### 5.1 Summary of Thesis

This dissertation has developed three different numerical schemes for implementing membrane viscosity in IBM, and comprehensive tests have been conducted to study their numerical performances, such as accuracy, stability and computational efficiency. Furthermore, the effects of membrane viscosity on the capsule dynamics in shear flow have been examined in detail.

The thesis started with an introduction of the complex structure of RBC membrane and its mechanical properties due to its natural structure. Subsequently, the particular behaviours of RBCs in various flows were reviewed. A single RBC may exhibit tank-treading, swinging or tumbling motion in simple shear flow. Multiple RBCs flowing in a vessel show a two-phase-separation, the core RBCs and CFL. The Fahreaus and Fahraeus-Linqvist effects in tube flows and the hematocrit separation at bifurcations were introduced as well. The literature review explained that an appropriate numerical scheme for membrane vis-

cosity in IBM simulations is lacking and the viscosity effect on RBC dynamics has not been well addressed yet. Moreover, three typical numerical methods, namely DPD, BIM and IBM, for analyzing biological capsule and vesicle dynamics in flow were discussed from their advantages and limitations.

To achieve the motivation and objectives, my Ph.D. research is conducted in three major steps: model development and validation, algorithm analysis from accuracy, stability and efficiency, and investigation of the effects of membrane viscosity on capsule dynamics in shear flow.

In Chapter 2, a finite-difference scheme for the RBC membrane viscous stress simulation was developed. This approach can efficiently avoid severe numerical instability while implementing the membrane viscosity in IBM. The method had been validated by comparing with theoretical and previous numerical studies. Good agreements were observed in these comparisons. Thereafter, this scheme is utilized to analyze the membrane viscosity effect on the dynamics of an individual capsule in shear flow. It was observed that the membrane viscosity can reduce the capsule deformation and even transfer the capsule motion from tank-treading to oscillation modes. The inclination angle decreases with the membrane viscosity to an apparent minimum value, before strong oscillations in capsule deformation and orientation were observed at high membrane viscosity. Accompanied by the appearance of capsule oscillation, the equilibrium inclination angle starts to increase from the minimum value. Besides, tests for the membrane mesh resolution and simulation time step were also conducted. The results further prove there is no apparent influence of this method on the simulation accuracy. This finite-difference scheme has several advantages over other existing attempts for membrane viscosity simulation, such as the consistency to the classi-

cal membrane viscosity definition, the ability to include independent shear and dilatational membrane viscosities, the simple algorithm formulation, and the easy implementation in IBM programs.

In Chapter 3, apart from the finite-difference scheme in Chapter 2, two new numerical schemes had been developed based on the convolution integral expression of the Maxwell viscoelastic element for membrane viscous stress calculation in IBM simulations. The three schemes were rigorously examined in the aspects of accuracy, stability and efficiency. Our analysis confirmed that these schemes can have a good accuracy as long as the relaxation time is in a proper range: it should be sufficiently smaller than the characteristic time  $T_0$  of the strain variation and, in the meantime, it should be sufficiently larger than the viscous stress calculation interval  $\Delta t$ . Next, it was shown that the simulation errors caused by viscous stress schemes could be negligible, comparing with the membrane discretization and the IBM velocity interpolation processing. At last, we applied these schemes to simulate the dynamic deformation of a spherical capsule in shear flow with various combinations of the artificial spring stiffness  $\kappa$  and the viscous stress calculation frequency  $N$ . Results showed that these schemes demonstrated virtually identical performances in simulation accuracy and stability, while the computation time is insignificant compared to other calculations in IBM simulations. In addition, we defined a nondimensional parameter, the artificial spring stiffness  $\kappa$ , on which the simulation accuracy and stability essentially depend. As concluded in this chapter, the accuracy improves with  $\kappa$  and is independent of the viscous stress calculation frequency  $N$ . Meanwhile, simulations can become unstable when large  $\kappa$  and  $N$  values are used, and the critical  $\kappa$  value for the stable-unstable transition decreases with the frequency  $N$  and the membrane viscosity. Based on these results,

we suggest to set  $N = 1$ , which means to calculate the viscous stress at each simulation time step.

With the membrane viscosity method established, simulations were conducted to study the effects of the membrane and interior fluid viscosities on capsule dynamics in shear flows in Chapter 4. Although higher values of both membrane and interior fluid viscosities can reduce the capsule deformation, their effects on the inclination angle are distinctive: the inclination angle decreases monotonically with the interior fluid viscosity increases. On the other hand, a decrease-then-increase variation was noticed for inclination angle response to the membrane viscosity increase. Furthermore, comparing to a higher interior fluid viscosity, a higher membrane viscosity can introduce more severe oscillations in the capsule deformation and inclination angle. In addition, an intuitive qualitatively mechanics explanation was also provided for the spoon-like variations in membrane velocity and capsule rotation frequency from the observed capsule deformation and inclination. At last, I examined the validity and accuracy of the previous simplification treatment which suggested replacing the membrane viscous effect with an elevated interior fluid viscosity. The analysis indicates that the membrane viscous effect cannot be represented by simply increasing the interior fluid viscosity, and the results from such treatment could be inaccurate or even misleading. Explicit modelling of the membrane viscosity is therefore necessary for future theoretical and numerical studies for capsule dynamics.

In summary, I have developed three different schemes for the numerical simulation of the membrane viscosity in the biological capsule and vesicle dynamics in flow with IBM. Extensive validations and examinations were performed to study the accuracy, stability and computational efficiency of my algorithms. Meanwhile, the effects of membrane viscos-

ity on the capsule dynamics were investigated. The results confirmed that the membrane viscosity is an essential property for the complicated capsule dynamics and it should be considered explicitly in future related researches. In addition, the analysis and discussions in this dissertation are also useful for selecting proper parameters in membrane viscosity simulation implemented in IBM.

## 5.2 Future Work

Membrane viscosity is an important property that effects the dynamics of biological capsules and vesicles in flow. The algorithms implementing membrane viscosity in IBM have been developed with validation and extensive comparison. Also, general guidelines for selecting simulation parameters are provided. Based on the achievements of this thesis, several topics can be explored in the future. Although RBC has some common properties as capsule, the varieties still exist, such as geometry, membrane bending, area and volume conservation forces internal mechanics. In future work, researchers can apply the current model to examine the effects of membrane viscosity on a single RBC in shear flow.

First, with our new methods, the membrane viscosity effect on RBC dynamics can be examined. The simulations in Chapter 4 have considered a spherical capsule in shear flow of capillary number  $Ca=0.3$  and the membrane has a relatively area dilatation modulus. This system is different from human RBCs in several aspects, including the bi-concave shape, the high area dilatation modulus, and the membrane bending modulus [50]. In addition, the capillary number, which characterizes the relative strength of shear stress to membrane elasticity, is also a crucial factor in determining the RBC behaviors in shear flows

[126–128]. Previous RBC simulations [31, 41, 47, 126] have often neglected the membrane viscosity effect due to the absence of a convenient and reliable numerical method. For a better understanding of the role of membrane viscosity in RBC dynamics, this topic needs to be explored carefully using realistic RBC parameters. Considering the complex capsule behaviors and relations among the system parameters when membrane viscosity is involved, this research would be complicated and caution should be executed for the simulation design, result collection, and data analysis.

In this thesis, only one capsule in the shear flow has been considered. In the future, numerical simulations can be performed to study multiple RBCs in other flow situations, such as the RBC migration process in straight vessels and the separation process at bifurcations with the membrane viscosity considered [68, 129–131]. For these simulations, the vessel structure could be complex and also a larger simulation domain might be necessary. To improve computational efficiency, the data structures and programs need to be updated. In particular, the MPI (message passing interface) technology [132] or even GPU (graphic processing unit) computation [133–135] could be considered for their good performances with advanced computational facilities.

For all simulations in this thesis, the flow field has been solved by LBM. As a matter of fact, the membrane viscosity methods developed in Chapters 2 and 3 are independent of the flow solvers, and they are applicable to other numerical techniques for the fluid flow, such as the finite volume method and even the dissipative particle dynamics method. These methods have been used in capsule and RBC simulations before [37, 40, 134, 136, 137] and I would be glad to see future applications of the membrane viscosity methods developed in this thesis with other numerical schemes.

## Reference

- [1] R. W. Flumerfelt. Effects of dynamic interfacial properties on drop deformation and orientation in shear and extensional flow fields. *Journal of Colloid and Interface Science*, 76(2):330–349, 1980.
- [2] J. Gounley, G. Boedec, M. Jaeger, and M. Leonetti. Influence of surface viscosity on droplets in shear flow. *Journal of Fluid Mechanics*, 791:464–494, 2016.
- [3] W. L. Murfee and G. W. Schmid-Schönbein. Structure of microvascular networks in genetic hypertension. *Methods in Enzymology*, 444:271–284, 2008.
- [4] G. Rodríguez-Lázaro. *Red Blood Cell Mechanics: From Membrane Elasticity to Blood Rheology*. PhD thesis, Universitat de Barcelona, 2014.
- [5] A. Nans, N. Mohandas, and D. L. Stokes. Native ultrastructure of the red cell cytoskeleton by cryo-electron tomography. *Biophysical Journal*, 101(10):2341–2350, 2011.
- [6] J. Zhang, P. C. Johnson, and A. S. Popel. Simulating microscopic hemodynamics and hemorheology with the immersed-boundary lattice-boltzmann method. *Computational Hydrodynamics of Capsules and Biological Cells*. CRC Press, pages 113–148, 2010.

- [7] J. J. Bishop, P. R. Nance, A. S. Popel, M. Intaglietta, and P. C. Johnson. Relationship between erythrocyte aggregate size and flow rate in skeletal muscle venules. *American Journal of Physiology-Heart and Circulatory Physiology*, 286(1):113–120, 2004.
- [8] A. R. Pries and T. W. Secomb. Microvascular blood viscosity in vivo and the endothelial surface layer. *American Journal of Physiology-Heart and Circulatory Physiology*, 289(6):H2657–H2664, 2005.
- [9] A. Yazdani and P. Bagchi. Influence of membrane viscosity on capsule dynamics in shear flow. *Journal of Fluid Mechanics*, 718:569–595, 2013.
- [10] P. R. Zarda, S. Chien, and R. Skalak. Elastic deformations of red blood cells. *Journal of Biomechanics*, 10(4):211–221, 1977.
- [11] C. Pozrikidis. *Modeling and Simulation of Capsules and Biological Cells*. CRC Press, 2003.
- [12] R. Skalak, A. Tozeren, R. P. Zarda, and S. Chien. Strain energy function of red blood cell membranes. *Biophysical Journal*, 13(3):245–264, 1973.
- [13] A. S. Popel and P. C. Johnson. Microcirculation and hemorheology. *Annual Review of Fluid Mechanics*, 37:43–69, 2005.
- [14] T. Fischer and H. Schmid-Schönbein. Tank tread motion of red cell membranes in viscometric flow: behavior of intracellular and extracellular markers (with film). In *Red Cell Rheology*, pages 347–361. Springer, 1978.
- [15] J. Zhang, P. C. Johnson, and A. S. Popel. An immersed boundary lattice boltzmann

- approach to simulate deformable liquid capsules and its application to microscopic blood flows. *Physical biology*, 4(4):285, 2007.
- [16] M. Abkarian, M. Faivre, and A. Viallat. Swinging of red blood cells under shear flow. *Physical Review Letters*, 98(18):188302, 2007.
- [17] S. K. Mitra and S. Chakraborty. *Microfluidics and Nanofluidics Handbook: Chemistry, Physics, and Life Science Principles*. CRC Press, 2011.
- [18] O. Baskurt, B. Neu, and H. J. Meiselman. *Red blood Cell Aggregation*. CRC Press, 2011.
- [19] E. W. Merrill, E. R. Gilliland, T. S. Lee, and E. W. Salzman. Blood rheology: effect of fibrinogen deduced by addition. *Circulation Research*, 18(4):437–446, 1966.
- [20] H. Baumler and E. Donath. Does dextran indeed significantly increase the surface-potential of human red-blood-cells. *Studia Biophysica*, 120(2):113–122, 1987.
- [21] R. Fahraeus and T. Lindqvist. The viscosity of the blood in narrow capillary tubes. *American Journal of Physiology-Legacy Content*, 96(3):562–568, 1931.
- [22] G. R. Cokelet and H. L. Goldsmith. Decreased hydrodynamic resistance in the two-phase flow of blood through small vertical tubes at low flow rates. *Circulation Research*, 68(1):1–17, 1991.
- [23] H. L. Goldsmith. Red cell motions and wall interactions in tube flow. In *Federation Proceedings*, volume 30, pages 1578–1590. 1971.
- [24] J. O. Barber, J. P. Alberding, J. M. Restrepo, and T. W. Secomb. Simulated two-

- dimensional red blood cell motion, deformation, and partitioning in microvessel bifurcations. *Annals of Biomedical Engineering*, 36(10):1690–1698, 2008.
- [25] P. Cabrales, A. G. Tsai, and M. Intaglietta. Increased plasma viscosity prolongs microhemodynamic conditions during small volume resuscitation from hemorrhagic shock. *Resuscitation*, 77(3):379–386, 2008.
- [26] R. M. Hochmuth. Micropipette aspiration of living cells. *Journal of Biomechanics*, 33(1):15–22, 2000.
- [27] S. Henon, G. Lenormand, A. Richert, and F. Gallet. A new determination of the shear modulus of the human erythrocyte membrane using optical tweezers. *Biophysical Journal*, 76(2):1145–1151, 1999.
- [28] M. Puig-de, K. T. Turner, J. P. Butler, J. J. Fredberg, and S. Suresh. Viscoelasticity of the human red blood cell. *American Journal of Physiology-Cell Physiology*, 293(2):C597–C605, 2007.
- [29] T. M. Fischer. Tank-tread frequency of the red cell membrane: dependence on the viscosity of the suspending medium. *Biophysical Journal*, 93(7):2553–2561, 2007.
- [30] T. M. Fischer, M. Stohr-Lissen, and H. Schmid-Schonbein. The red cell as a fluid droplet: tank tread-like motion of the human erythrocyte membrane in shear flow. *Science*, 202(4370):894–896, 1978.
- [31] C. D. Eggleton and A. S. Popel. Large deformation of red blood cell ghosts in a simple shear flow. *Physics of Fluids*, 10(8):1834–1845, 1998.

- [32] Y. Sui, H. T. Low, Y. T. Chew, and P. Roy. Tank-treading, swinging, and tumbling of liquid-filled elastic capsules in shear flow. *Physical Review E*, 77(1):016310, 2008.
- [33] J. M. Skotheim and T. W. Secomb. Red blood cells and other nonspherical capsules in shear flow: oscillatory dynamics and the tank-treading-to-tumbling transition. *Physical Review Letters*, 98(7):078301, 2007.
- [34] T. Ye, N. Phan-Thien, and C. T. Lim. Particle-based simulations of red blood cells—a review. *Journal of Biomechanics*, 49(11):2255–2266, 2016.
- [35] D. A. Fedosov. *Multiscale modeling of blood flow and soft matter*. Citeseer, 2010.
- [36] T. Ye, N. Phan-Thien, B. Cheong-Khoo, and C. Teck-Lim. Numerical modelling of a healthy/malaria-infected erythrocyte in shear flow using dissipative particle dynamics method. *Journal of Applied Physics*, 115(22):224701, 2014.
- [37] T. Ye, N. Phan-Thien, B. C. Khoo, and C. T. Lim. Dissipative particle dynamics simulations of deformation and aggregation of healthy and diseased red blood cells in a tube flow. *Physics of Fluids*, 26(11):111902, 2014.
- [38] D. A. Fedosov, H. Noguchi, and G. Gompper. Multiscale modeling of blood flow: from single cells to blood rheology. *Biomechanics and Modeling in Mechanobiology*, 13(2):239–258, 2014.
- [39] D. A. Fedosov, M. Dao, G. E. Karniadakis, and S. Suresh. Computational biorheology of human blood flow in health and disease. *Annals of Biomedical Engineering*, 42(2):368–387, 2014.
- [40] X. Li, A. S. Popel, and G. E. Karniadakis. Blood–plasma separation in y-shaped

- bifurcating microfluidic channels: a dissipative particle dynamics simulation study. *Physical Biology*, 9(2):026010, 2012.
- [41] M. Ju, S. S. Ye, B. Namgung, S. Cho, H. T. Low, H. L. Leo, and S. Kim. A review of numerical methods for red blood cell flow simulation. *Computer Methods in Biomechanics and Biomedical Engineering*, 18(2):130–140, 2015.
- [42] C. Pozrikidis. Finite deformation of liquid capsules enclosed by elastic membranes in simple shear flow. *Journal of Fluid Mechanics*, 297:123–152, 1995.
- [43] S. Ramanujan and C. Pozrikidis. Deformation of liquid capsules enclosed by elastic membranes in simple shear flow: large deformations and the effect of fluid viscosities. *Journal of Fluid Mechanics*, 361:117–143, 1998.
- [44] E. Lac, D. Barthes-Biesel, N. A. Pelekasis, and J. Tsamopoulos. Spherical capsules in three-dimensional unbounded stokes flows: effect of the membrane constitutive law and onset of buckling. *Journal of Fluid Mechanics*, 516:303–334, 2004.
- [45] J. B. Freund. Leukocyte margination in a model microvessel. *Physics of Fluids*, 19(2):023301, 2007.
- [46] C. S. Peskin. Numerical analysis of blood flow in the heart. *Journal of Computational Physics*, 25(3):220–252, 1977.
- [47] J. Zhang, P. C. Johnson, and A. S. Popel. Red blood cell aggregation and dissociation in shear flows simulated by lattice boltzmann method. *Journal of Biomechanics*, 41(1):47–55, 2008.

- [48] P. Bagchi. Mesoscale simulation of blood flow in small vessels. *Biophysical Journal*, 92(6):1858–1877, 2007.
- [49] G. Tomaiuolo. Biomechanical properties of red blood cells in health and disease towards microfluidics. *Biomicrofluidics*, 8(5):051501, 2014.
- [50] J. D. Bronzino. *Biomedical Engineering Handbook*, volume 2. CRC press, 1999.
- [51] R. P. Rand and A. C. Burton. Mechanical properties of the red cell membrane: I. membrane stiffness and intracellular pressure. *Biophysical Journal*, 4(2):115–135, 1964.
- [52] R. P. Rand. Mechanical properties of the red cell membrane: II. viscoelastic breakdown of the membrane. *Biophysical Journal*, 4(4):303, 1964.
- [53] H. Noguchi and G. Gompper. Fluid vesicles with viscous membranes in shear flow. *Physical Review Letters*, 93(25):258102, 2004.
- [54] H. Noguchi and G. Gompper. Dynamics of fluid vesicles in shear flow: Effect of membrane viscosity and thermal fluctuations. *Physical Review E*, 72(1):011901, 2005.
- [55] C. Pozrikidis. *Computational Hydrodynamics of Capsules and Biological Cells*. CRC press, 2010.
- [56] D. A. Fedosov, B. Caswell, and G. E. Karniadakis. A multiscale red blood cell model with accurate mechanics, rheology, and dynamics. *Biophysical Journal*, 98(10):2215–2225, 2010.

- [57] R. Tran-Son-Tay, S. P. Suter, and P. R. Rao. Determination of red blood cell membrane viscosity from rheoscopic observations of tank-treading motion. *Biophysical Journal*, 46(1):65–72, 1984.
- [58] J. Gounley and Y. Peng. Computational modeling of membrane viscosity of red blood cells. *Communications in Computational Physics*, 17(4):1073–1087, 2015.
- [59] R. M. Christensen. A nonlinear theory of viscoelasticity for application to elastomers. *Journal of Applied Mechanics*, 47(4):762–768, 1980.
- [60] C. S. Peskin. The immersed boundary method. *Acta Numerica*, 11:479–517, 2002.
- [61] Z. Hashemi, O. Abouali, and G. Ahmadi. Direct numerical simulation of particle–fluid interactions: A review. *Iranian Journal of Science and Technology, Transactions of Mechanical Engineering*, 41(1):71–89, 2017.
- [62] M. Maxey. Simulation methods for particulate flows and concentrated suspensions. *Annual Review of Fluid Mechanics*, 49:171–193, 2017.
- [63] G. Hou, J. Wang, and A. Layton. Numerical methods for fluid-structure interaction a review. *Communications in Computational Physics*, 12(2):337–377, 2012.
- [64] R. Mittal and G. Iaccarino. Immersed boundary methods. *Annual Review of Fluid Mechanics*, 37:239–261, 2005.
- [65] K. Lykov, Y. Nematbakhsh, M. Shang, C. T. Lim, and I. V. Pivkin. Probing eukaryotic cell mechanics via mesoscopic simulations. *PLoS Computational Biology*, 13(9):e1005726, 2017.

- [66] T. Krüger, F. Varnik, and D. Raabe. Efficient and accurate simulations of deformable particles immersed in a fluid using a combined immersed boundary lattice boltzmann finite element method. *Computers & Mathematics with Applications*, 61(12):3485–3505, 2011.
- [67] M. Mokbel, D. Mokbel, A. Mietke, N. Traber, S. Girardo, O. Otto, J. Guck, and S. Aland. Numerical simulation of real-time deformability cytometry to extract cell mechanical properties. *ACS Biomaterials Science & Engineering*, 3(11):2962–2973, 2017.
- [68] X. Yin, T. Thomas, and J. Zhang. Multiple red blood cell flows through microvascular bifurcations: cell free layer, cell trajectory, and hematocrit separation. *Microvascular Research*, 89:47–56, 2013.
- [69] T. G. Fai, B. E. Griffith, Y. Mori, and C. S. Peskin. Immersed boundary method for variable viscosity and variable density problems using fast constant-coefficient linear solvers i: Numerical method and results. *SIAM Journal on Scientific Computing*, 35(5):B1132–B1161, 2013.
- [70] E. Evans and Y. Fung. Improved measurements of the erythrocyte geometry. *Microvascular Research*, 4(4):335–347, 1972.
- [71] K. Xie, C. De L., F. Dubreuil, D. Z. Gunes, M. Jaeger, and M. Léonetti. Interfacial rheological properties of self-assembling biopolymer microcapsules. *Soft Matter*, 13(36):6208–6217, 2017.
- [72] I. Koleva and H. Rehage. A comparison of different experimental methods for in-

- vestigating the mechanical properties of plane polysiloxane membranes and capsule walls. *Soft Matter*, 8(29):7672–7682, 2012.
- [73] I. Koleva and H. Rehage. Deformation and orientation dynamics of polysiloxane microcapsules in linear shear flow. *Soft Matter*, 8(13):3681–3693, 2012.
- [74] J. G. Oldroyd. The effect of interfacial stabilizing films on the elastic and viscous properties of emulsions. *Proceedings of the Royal Society of London A*, 232(1191):567–577, 1955.
- [75] M. A. Bos and T. van Vliet. Interfacial rheological properties of adsorbed protein layers and surfactants: a review. *Advances in Colloid and Interface Science*, 91(3):437–471, 2001.
- [76] N. Alexandrov, K. G. Marinova, K. D. Danov, and I. B. Ivanov. Surface dilatational rheology measurements for oil/water systems with viscous oils. *Journal of Colloid and Interface Science*, 339(2):545–550, 2009.
- [77] Z. Wang and G. Narsimhan. Interfacial dilatational elasticity and viscosity of  $\beta$ -lactoglobulin at air- water interface using pulsating bubble tensiometry. *Langmuir*, 21(10):4482–4489, 2005.
- [78] D. Möbius and R. Miller. *Proteins at liquid interfaces*, volume 7. Elsevier, 1998.
- [79] J. M. Lopez, M. J. Vogel, and A. H. Hirska. Influence of coexisting phases on the surface dilatational viscosity of langmuir monolayers. *Physical Review E*, 70(5):056308, 2004.

- [80] R. Dimova, K. A. Riske, S. Aranda, N. Bezlyepkina, R. L. Knorr, and R. Lipowsky. Giant vesicles in electric fields. *Soft Matter*, 3(7):817–827, 2007.
- [81] O. Oulaid, A. W. Saad, P. S. Aires, and J. Zhang. Effects of shear rate and suspending viscosity on deformation and frequency of red blood cells tank-treading in shear flows. *Computer Methods in Biomechanics and Biomedical Engineering*, 19(6):648–662, 2016.
- [82] C. Pozrikidis. Effects of surface viscosity on the finite deformation of a liquid drop and the rheology of dilute emulsions in simple shearing flow. *Journal of Non-Newtonian Fluid Mechanics*, 51(2):161–178, 1994.
- [83] S. P. Marques and G. J. Creus. *Computational Viscoelasticity*. Springer Science & Business Media, 2012.
- [84] A. Z. K. Yazdani. *Dynamics of Erythrocytes, Vesicles and Capsules in Shear Flow: The Role of Membrane Bending Stiffness and Membrane Viscosity*. PhD thesis, Rutgers University, 2012.
- [85] P. Bagchi, P. C. Johnson, and A. S. Popel. Computational fluid dynamic simulation of aggregation of deformable cells in a shear flow. *Journal of Biomechanical Engineering*, 127(7):1070–1080, 2005.
- [86] J. M. Charrier, S. Shrivastava, and R. Wu. Free and constrained inflation of elastic membranes in relation to thermoforming—non-axisymmetric problems. *The Journal of Strain Analysis for Engineering Design*, 24(2):55–74, 1989.
- [87] D. Barthes-Biesel and H. Sgaier. Role of membrane viscosity in the orientation

- and deformation of a spherical capsule suspended in shear flow. *Journal of Fluid Mechanics*, 160:119–135, 1985.
- [88] T. W. Secomb and R. Skalak. Surface flow of viscoelastic membranes in viscous fluids. *The Quarterly Journal of Mechanics and Applied Mathematics*, 35(2):233–247, 1982.
- [89] H. Krüger. *Computer Simulation Study of Collective Phenomena in Dense Suspensions of Red Blood Cells under Shear*. Springer Science & Business Media, 2012.
- [90] A. E. Komrakova, O. Shardt, D. Eskin, and J. J. Derksen. Lattice boltzmann simulations of drop deformation and breakup in shear flow. *International Journal of Multiphase Flow*, 59:24–43, 2014.
- [91] J. F. Hammond, E. J. Stewart, J. G. Younger, M. J. Solomon, and D. M. Bortz. Variable viscosity and density biofilm simulations using an immersed boundary method, part i: numerical scheme and convergence results. *Computer Modeling in Engineering and Sciences*, 98:295–340, 2014.
- [92] Y. Mori and C. S.s Peskin. Implicit second-order immersed boundary methods with boundary mass. *Computer Methods in Applied Mechanics and Engineering*, 197(25-28):2049–2067, 2008.
- [93] S. Succi and S. Succi. *The lattice Boltzmann equation: for fluid dynamics and beyond*. Oxford university press, 2001.
- [94] Z. Guo, C. Zheng, and B. Shi. Discrete lattice effects on the forcing term in the lattice boltzmann method. *Physical Review E*, 65(4):046308, 2002.

- [95] R. M. Hochmuth and R. E. Waugh. Erythrocyte membrane elasticity and viscosity. *Annual Review of Physiology*, 49(1):209–219, 1987.
- [96] Y. Kim, K. Kim, and Y. Park. Measurement techniques for red blood cell deformability: recent advances. *Blood Cell—An Overview of Studies in Hematology*, 10:167–194, 2012.
- [97] J. Wan, A. M. Forsyth, and H. A. Stone. Red blood cell dynamics: from cell deformation to atp release. *Integrative Biology*, 3(10):972–981, 2011.
- [98] C. S. Peskin. Flow patterns around heart valves: a numerical method. *Journal of Computational Physics*, 10(2):252–271, 1972.
- [99] P. Li and J. Zhang. A finite difference method with sub-sampling for immersed boundary simulations of the capsule dynamics with viscoelastic membranes. *International Journal for Numerical Methods in Biomedical Engineering*, page e3200, 2019.
- [100] S. Shrivastava and J. Tang. Large deformation finite element analysis of non-linear viscoelastic membranes with reference to thermoforming. *The Journal of Strain Analysis for Engineering Design*, 28(1):31–51, 1993.
- [101] M. A. Neto, A. Amaro, L. Roseiro, J. Cirne, and R. Leal. *Engineering Computation of Structures: the Finite Element Method*. Springer, 2015.
- [102] J. Zhang. Lattice boltzmann method for microfluidics: models and applications. *Microfluidics and Nanofluidics*, 10(1):1–28, 2011.

- [103] D. Barthes-Biesel. Motion and deformation of elastic capsules and vesicles in flow. *Annual Review of Fluid Mechanics*, 48:25–52, 2016.
- [104] P. M. Vlahovska. Dynamics of membrane-bound particles: Capsules and vesicles. In *Fluid-Structure Interactions in Low-Reynolds-Number Flows*, pages 313–346. Royal Society of Chemistry, 2015.
- [105] A. Diaz and D. Barthes-Biesel. Entrance of a bioartificial capsule in a pore. *Computer Modeling in Engineering and Sciences*, 3(3):321–338, 2001.
- [106] F. Lim. *Biomedical Applications of Microencapsulation*. CRC press, 2019.
- [107] Willem M Kühtreiber, Robert Paul Lanza, and William Louis Chick. *Cell encapsulation technology and therapeutics*. Springer Science & Business Media, 1999.
- [108] H.L. Goldsmith, J. Marlow, and F. C. MacIntosh. Flow behaviour of erythrocytes-i. rotation and deformation in dilute suspensions. *Proceedings of the Royal Society B: Biological Sciences*, 182(1068):351–384, 1972.
- [109] T. M. Fischer. Creep and stress relaxation of human red cell membrane. *Biomechanics and Modeling in Mechanobiology*, 16(1):239–247, 2017.
- [110] K. S. Chang and W. L. Olbricht. Experimental studies of the deformation and breakup of a synthetic capsule in steady and unsteady simple shear flow. *Journal of Fluid Mechanics*, 250:609–633, 1993.
- [111] A. Walter, H. Rehage, and H. Leonhard. Shear-induced deformations of polyamide microcapsules. *Colloid and Polymer Science*, 278(2):169–175, 2000.

- [112] S. R. Keller and R. Skalak. Motion of a tank-treading ellipsoidal particle in a shear flow. *Journal of Fluid Mechanics*, 120:27–47, 1982.
- [113] D. Barthes-Biesel. Motion of a spherical microcapsule freely suspended in a linear shear flow. *Journal of Fluid Mechanics*, 100(4):831–853, 1980.
- [114] G. Závodszy, B. van Rooij, V. Azizi, and A. Hoekstra. Cellular level in-silico modeling of blood rheology with an improved material model for red blood cells. *Frontiers in Physiology*, 8:563, 2017.
- [115] R. M. Hochmuth, P. R. Worthy, and E. A. Evans. Red cell extensional recovery and the determination of membrane viscosity. *Biophysical Journal*, 26(1):101–114, 1979.
- [116] F. Guglietta, M. Behr, L. Biferale, G. Falcucci, and M. Sbragaglia. On the effects of membrane viscosity on transient red blood cell dynamics. *Soft Matter*, 2020.
- [117] S. K. Doddi and P. Bagchi. Lateral migration of a capsule in a plane poiseuille flow in a channel. *International Journal of Multiphase Flow*, 34(10):966–986, 2008.
- [118] E. A. Evans and R. M. Hochmuth. Membrane viscoelasticity. *Biophysical Journal*, 16(1):1–11, 1976.
- [119] S. Chien. Red cell deformability and its relevance to blood flow. *Annual Review of Physiology*, 49(1):177–192, 1987.
- [120] T. M. Fischer. On the energy dissipation in a tank-treading human red blood cell. *Biophysical Journal*, 32(2):863, 1980.

- [121] J. N. Reddy. *An Introduction to the Finite Element Method*, volume 1221. McGraw-Hill New York, 2010.
- [122] P. Li and J. Zhang. Finite-difference and integral schemes for maxwell viscous stress calculation in immersed boundary simulations of viscoelastic membranes. *Biomechanics and Modeling in Mechanobiology*, 19(6):2667–2681, 2020.
- [123] G. Le and J. Zhang. Boundary slip from the immersed boundary lattice boltzmann models. *Physical Review E*, 79(2):026701, 2009.
- [124] T. Seta, R. Rojas, K. Hayashi, and A. Tomiyama. Implicit-correction-based immersed boundary–lattice boltzmann method with two relaxation times. *Physical Review E*, 89(2):023307, 2014.
- [125] P. Bagchi and R. M. Kalluri. Dynamics of nonspherical capsules in shear flow. *Physical Review E*, 80(1):016307, 2009.
- [126] A. Z. Yazdani, R. M. Kalluri, and P. Bagchi. Tank-treading and tumbling frequencies of capsules and red blood cells. *Physical Review E*, 83(4):046305, 2011.
- [127] T. Omori, T. Ishikawa, D. Barthès-Biesel, A. V. Salsac, Y. Imai, and T. Yamaguchi. Tension of red blood cell membrane in simple shear flow. *Physical Review E*, 86(5):056321, 2012.
- [128] D. Cordasco and P. Bagchi. Orbital drift of capsules and red blood cells in shear flow. *Physics of Fluids*, 25(9):091902, 2013.
- [129] T. Krüger. Effect of tube diameter and capillary number on platelet margination and near-wall dynamics. *Rheologica Acta*, 55(6):511–526, 2016.

- [130] P. Balogh and P. Bagchi. Analysis of red blood cell partitioning at bifurcations in simulated microvascular networks. *Physics of Fluids*, 30(5):051902, 2018.
- [131] A. W. El-Kareh and T. W. Secomb. A model for red blood cell motion in bifurcating microvessels. *International Journal of Multiphase Flow*, 26(9):1545–1564, 2000.
- [132] W. Gropp, W. D. Gropp, E. Lusk, A. Skjellum, and A. Lusk. *Using MPI: Portable Parallel Programming with the Message-Passing Interface*, volume 1. MIT press, 1999.
- [133] A. Cano. A survey on graphic processing unit computing for large-scale data mining. *Wiley Interdisciplinary Reviews: Data Mining and Knowledge Discovery*, 8(1):e1232, 2018.
- [134] A. L. Blumers, Y. H. Tang, Z. Li, X. Li, and G. E. Karniadakis. Gpu-accelerated red blood cells simulations with transport dissipative particle dynamics. *Computer Physics Communications*, 217:171–179, 2017.
- [135] J. Ames, D. F. Puleri, P. Balogh, J. Gounley, E. W. Draeger, and A. Randles. Multi-gpu immersed boundary method hemodynamics simulations. *Journal of Computational Science*, page 101153, 2020.
- [136] A. S. Jahangir, G. Q. Hu, and L. K. Yu. Simulation of red particles in blood cell. In *Applied Mechanics and Materials*, volume 477, pages 330–334. Trans Tech Publ, 2014.
- [137] M. Soleimani, S. Sahraee, and P. Wriggers. Red blood cell simulation using a coupled shell–fluid analysis purely based on the sph method. *Biomechanics and Modeling in Mechanobiology*, 18(2):347–359, 2019.